Stellar kinematics in surveys and simulations

Mikkola, Daniel

2022

Citation for published version (APA):
Mikkola, D. (2022). *Stellar kinematics in surveys and simulations*. [Doctoral Thesis (compilation), Department of Astronomy and Theoretical Physics - Has been reorganised]. Lund Observatory, Lund University.

LUND UNIVERSITY

PO Box 117
221 00 Lund
+46 46-222 00 00

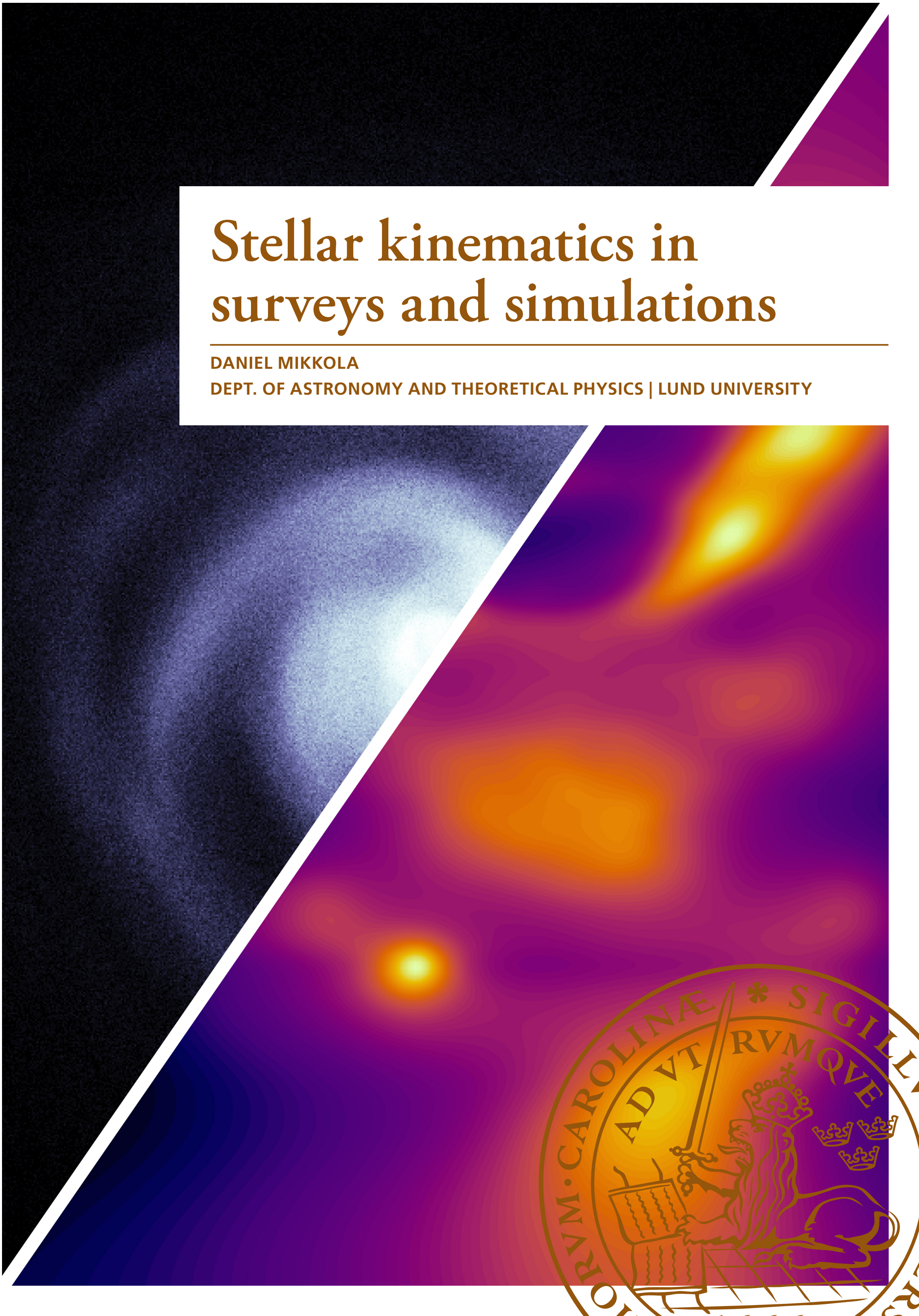

Stellar kinematics in surveys and simulations

DANIEL MIKKOLA

DEPT. OF ASTRONOMY AND THEORETICAL PHYSICS | LUND UNIVERSITY

Stellar kinematics in surveys and simulations

Daniel Mikkola

LUND
UNIVERSITY

Thesis for the degree of Doctor of Philosophy

Thesis advisor: Dr. David Hobbs
Co-advisor: Dr. Paul McMillan
Faculty opponent: Dr. Marie Martig

To be presented, with the permission of the Faculty of Science of Lund University, for public criticism in the Lundmark lecture hall (Lundmarksalen) at the Department of Astronomy and Theoretical Physics on the 18th November 2022 at 13:00.

Organization
LUND UNIVERSITY
Department of Astronomy and Theoretical Physics
Box 43, SE-22100 Lund, Sweden
Author(s)
Daniel Mikkola

Document name
DOCTORIAL DISSERTATION

Date of issue
2022-11-18

Sponsoring organization

Title and subtitle
Stellar kinematics in surveys and simulations

Abstract

As the Galaxy evolves it is subjected to a plethora of various dynamical processes that leave their mark upon it. We can view a snapshot of the ongoing processes and connect it to past events. To do this, we require an accurate picture of the stellar motions and positions which are predicted by numerical models. This is the two-pronged approach of Galactic dynamics which connects both theory and observations.

This thesis summarizes three papers where I use this approach to gain new insights into both the current structure of the local Galaxy and one of the processes responsible for it.

In Paper I, I seek to determine the relationship between the vertical extent of stellar orbits and their participation in radial migration across the disc. By numerically simulating different types of discs I am able to determine that radial migration primarily affects stars with small vertical excursions in halo-dominated galaxies and affects all stars more equally in disc-dominated ones.

In Paper II, I utilize the proper-motion limited catalogue of *Gaia* EDR3 to determine the most accurate velocity distribution of white dwarfs to date using a penalized likelihood estimate. This provides kinematics for the stars on the two sides of the bifurcation visible in the white dwarf cooling sequence. The paper is able to find known and some novel structure in the velocity distribution and finds that the bifurcation is related to two separate kinematic populations of white dwarfs.

In Paper III, I further apply the methods of Paper II to two new samples of stars: the local stellar halo and the Solar neighbourhood. With the updated Gaia DR3 I am able to show accurate velocity distributions for both samples and reveal new velocity substructures in the local halo which are part of the *accreted* stellar halo

Key words
Galactic dynamics, stellar kinematics, numerical simulations, statistical methods, solar neighbourhood

Classification system and/or index terms (if any)

Supplementary bibliographical information

Language
English

ISSN and key title

ISBN
ISBN: 978-91-8039-411-6 (print)
ISBN: 978-91-8039-412-3 (pdf)

Recipient’s notes

Number of pages
120

Price

Security classification

I, the undersigned, being the copyright owner of the abstract of the above-mentioned dissertation, hereby grant to all reference sources permission to publish and disseminate the abstract of the above-mentioned dissertation.

Signature

Date 2022-10-05

Stellar kinematics in surveys and simulations

Daniel Mikkola

LUND
UNIVERSITY

Faculty Opponent

Dr. Marie Martig
Astrophysics Research Institute, Liverpool John Moores University,
Liverpool, United Kingdom

Evaluation Committee

Dr. Lise Christensen
Niels Bohr Institute, University of Copenhagen,
Copenhagen, Denmark

Dr. Christa Gall
Niels Bohr Institute, University of Copenhagen,
Copenhagen, Denmark

Dr. Sijing Shen
Institute of Theoretical Astrophysics, University of Oslo,
Oslo, Norway

Front cover: The left side shows one of my simulated N-body galaxies. The right side shows is my estimated velocity distribution for the accreted stellar halo.
Funding information: Computations for this study were performed on equipment funded by a grant from the Royal Physiographic Society in Lund (Stiftelsen Walter Gyllenbergs Fond)

Faculty of Science, Department of Astronomy and Theoretical Physics

ISBN: 978-91-8039-411-6 (print)
ISBN: 978-91-8039-412-3 (pdf)

Printed in Sweden by Media-Tryck, Lund University, Lund 2022

Till morfar

Contents

List of publications

This thesis is based on the following peer-reviewed publications:

I **Radial migration and vertical action in N-body simulations**
Mikkola, D.; McMillan, P. J.; Hobbs, D. (2020)
Monthly Notices of the Royal Astronomical Society, Volume 495, Issue 3, pp. 3295-3306

II **The velocity distribution of white dwarfs in Gaia EDR3**
Mikkola, D.; McMillan, P. J.; Hobbs, D.; Wimarsson, J (2022)
Monthly Notices of the Royal Astronomical Society, Volume 512, Issue 4, pp. 6201-6216

III **New stellar halo substructures from Gaia DR3 proper motions**
Mikkola, D.; McMillan, P. J.; Hobbs, D. (2022)
Submitted to Monthly Notices of the Royal Astronomical Society

Papers I and II are reproduced with permission from Monthly Notices of the Royal Astronomical Society.

Popular summary

Of all things on the celestial vault, the greatest and most striking is the diffuse band of stars that make up the Milky Way, our home Galaxy. To understand how it formed and evolved we need, among other things, a detailed description of how the stars move and where they are located, the field of research called *astrometry*. The first stellar catalogue was created in 200 BCE by Hipparchus in ancient Greece. A little over two millennia later we began measuring stars with space telescopes, the first of which was named *Hipparcos*. This was succeeded by the space telescope *Gaia* which was launched in 2013 and revolutionized the field of astrometry, providing a truly great catalogue of stellar motions and positions. This catalogue has significantly contributed to the research behind this thesis. *Gaia* gives us a very precise picture of how the Milky Way kinematics look today. To complete the picture one also uses numerical simulations to recreate and interpret the features found in observations. The union of theory and observations then reinforce one another and is critical for our understanding of the Milky Way.

The first article in this thesis uses numerical simulations to study how interactions with the Galaxy's spiral arms and bar transport stars radially in the plane of the disc. We find that this migration depends on the Galactic disc's strength and how vertical extended the stellar orbit is. With over 100 simulated discs we could determine that in less massive discs it is mostly the stars close to the disc that migrate and in the opposite case of massive discs they migrate regardless of how far above the disc the orbit goes.

In the second and third articles, we use data from *Gaia*. By using positions and velocities along the celestial sphere, without needing velocities in the line-of-sight direction, we have access to extremely large amounts of data. This way, we obtain an estimate for the local stellar velocity distribution, despite lacking one velocity component. We do this for three samples of data. In the second article, we used white dwarfs, which are the remains of low mass dead stars, and could discover that there were two separate kinematic populations. In the third article, we used the Solar neighbourhood of stars in the disc and a local part of the Galaxy's halo. We were able to identify many known structures in the velocity distribution, as well as some new ones which then belong to the accreted halo, and could be the remains of accreted dwarf galaxies.

Populärvetenskaplig sammanfattning

Utav alla ting på himlavalvet så är det största och mest slående det diffusa band av stjärnor som uppgör Vintergatan, vår hemgalax. För att förstå hur den skapades och utvecklas behöver vi, bland annat, förstå i detalj hur stjärnorna rör sig och var det befinner sig, ett forskningsfält som kallas astrometri. Den första stjärnkatalogen kom 200 f.v.t. från Hipparkos i antika Grekland. Två millennier senare så började vi mäta stjärnor med rymdteleskop, det första då döpt till just Hipparcos. Detta efterföljdes av rymdteleskopet *Gaia* som sattes i omloppsbana 2013 och har revolutionerat astrometrin genom att bidra med en fantastisk stjärnkatalog av positioner och hastigheter. Denna katalog har bidragit stort till forskningen bakom denna avhandling. *Gaia* ger oss en väldigt noggran bild av hur Vintergatans kinematik ser ut idag. För att fullända bilden, använder man sig dessutom utav numeriska simuleringar som kan återskapa och förklara de resultat som vi ser i mätdatan. Föreningen av teori och observationer förstärker då varandra och är kritisk för vår förståelse av Vintergatan.

Den första artikeln i denna avhandling använder just numeriska simuleringar för att studera hur interaktioner med Galaxens spiral armar och centrala stav förflyttar stjärnor radiellt i skivans plan. Vi visar att denna migrering beror på Galaxskivans styrka och hur vertikalt utsträckt stjärnans omloppsbana är. Med över 100 simulerade skivor kunde vi bestämma att i mindre massiva skivor migrerar stjärnor mest nära skivan och i motsatt fall med en massiv skiva migrerar de oavsett hur långt utanför skivan som omloppsbanan går.

I den andra och tredje artikeln använder vi mätdatan från *Gaia*. Genom att vi använder positioner och hastigheter längst med himlavalvet, utan att kräva hastigheter i siktriktningen, får vi tillgång till extremt stora mängder data. Vi kan då uppskatta stjärnornas lokala hastighetsfördelning, trots att vi saknar en hastighet. Detta gjorde vi för tre olika urval av data. I den andra artikeln använder vi vita dvärgar, som är kvarlevorna av mindre massiva döda stjärnor, och kunde upptäcka att där fanns två separata kinematiska populationer. I tredje artikeln använder vi Solens kvarter av stjärnor i skivan och en lokal del av Galaxens halo. Där lyckas vi identifiera många kända strukturer i hastighetsfördelningen, samt några nya som tillhör den ansamlade halon, och skulle kunna vara kvarlevorna av uppslukade dvärggalaxer.

Acknowledgements

I am forever grateful to who is probably my greatest supporter, my beloved partner Tina Sörensen who has been by my side ever since I started my doctoral journey. Your unwavering support has been with me through difficult times with debugging, writing, contemplating, and a global pandemic. I would not be where I am today without you.

My supervisor, David Hobbs. You have mastered the art of knowing when to give a push and when to encourage letting go and taking a step back. You have inspired my work ethic and taken the best care of me as a student of yours. Your door has always been open to me and so has your ear. I will miss walking around the corner to have a chat about just anything.

My co-supervisor, Paul McMillan. Your guidance has been invaluable to me ever since we started working together during my master's project. I am ever impressed by your intuition when looking at new results and to me, you have always been a bottomless fount of knowledge. I regret that this is our last project together, however I think I now know what a good enough scientist would do.

I want to thank the friends I made at Lund Observatory during my stay here. There are too many master students, fellow PhDs, and staff members I want to thank for me to name them all here. Especially I want to thank Eric Andersson whose thesis has been in tandem with mine, which led to good friendship over the years. My first and second office-mates Iryna Kushniruk and Bibiana Prinoth, my closest colleagues in almost all matters besides research. You were the ones I could always 'turn' to and have a chat about either work or life in general. Wherever I end up in the future I am certain I will not have such a great office situation as the one you have given me.

I must not forget to thank the Physics & Lasershow. For almost ten years the show has let me mix work with incredible amounts of fun and given me some of my closest friends. Thank you Per-Olof, Johan Z, Stina, Odd, Johan K, Jonas, Alexandra, Frida, Rebecca, Vassily, Matteus, Lina, David, Elin, and Anna-Maria.

My friends outside of work: Anton, Sara, Fredrik, Marielle, Rasmus, Anna, Jesper, Lovisa, Johan. You have always made sure to keep me humble and to ask me any and all *astrology*-related questions, much to my bemusement. Adrian, I am thankful we reconnected during our PhDs and could share many hours working out or betraying each other in board games.

To conclude, I want to extend my deepest gratitude to the people who made sure I got here today: my family. First, my parents Marita and Seppo, who always made sure to let me explore while providing all the support I needed. My bonus-

mother Suzie, I aspire to have your fortitude. My five brothers: Nicholas, Robert, Christopher, Mattias, and Alexander. Of course also my extra family in Halmstad who have always welcomed me.

Preface

In this thesis, the primary question we seek to understand better is ”how do stars move in the Galaxy?”. To shed light on this I have examined radial migration in simulated Milky Way-like galaxies to constrain its dependencies. Furthermore, I have estimated the full 3D velocity distributions of different samples of local stars using the largest available astrometric catalogues from the *Gaia* mission. The velocity distributions have allowed us to demonstrate unknown properties of the white dwarf population as well as identify new velocity substructures which can tentatively be linked to accretion events.

This thesis summarises the work which has been published in two papers and is to be submitted in a third. Here follows a brief description of each paper to give the reader an overview of the thesis.

1. *Paper I: Radial migration and vertical action in N-body simulations* - My first paper seeks to determine how effectively stars are radially migrated as a function of how vertically extended their orbit is and how gravitationally dominant their stellar disc is. This was an interesting question since the current understanding of radial migration, following works by Solway et al. (2012); Vera-Ciro et al. (2014, 2016), especially the latter two, had firmly argued for what they call *provenance bias*; radial migration primarily affects stars with small vertical excursions. We investigated whether this *provenance bias* exists regardless of the strength of the spiral arms that cause the radial migration. This had also been investigated in the third of the cited papers, which found that it indeed was. To do this we set up our own simulations with a pure N-body bulge, halo, and disc. We used 11 different set-ups where the halo mass is varied. This allowed the force ratio of halo to disc, $F_\mathrm{h}/F_\mathrm{d}$ to vary between 0.5 to 3.2 at a Solar orbit. In other words, we went from strongly disc-dominated systems to halo-dominated systems. We could then quantify the radial migration by comparing the final and initial angular momentum $\Delta L_z = L_{z,f} - L_{z_i}$, and compare it to the vertical action. For a region of the disc, the migration is better described by the spread of ΔL_z, described by its standard deviation $\sigma_{\Delta L_z}$. We looked at the slope of the function that relates the migration efficiency parameter to the vertical action, J_z, at various radii of the disc in all of our simulations. This lets us show that the as the disc becomes more dominant, the slope flattens, and the provenance bias disappears across the whole disc. This was

not the case when migration efficiency was compared to radial action, which implied that there is a difference in the response of migration to increased actions in the various directions. We also recreated the simulations used by Vera-Ciro et al. (2016) and were able to reproduce our results there as well.

2. *Paper II: The velocity distribution of white dwarfs in Gaia EDR3* - In the second paper, the goal is to determine accurate velocity distributions for white dwarfs (WDs) without having to rely on measured line-of-sight velocities. The data releases of *Gaia* have revolutionised the field of astrometry and have produced a truly great catalogue of stellar motions and positions. Already in EDR3, the catalogue contained the full astrometric solution for up to $\sim$1.5 billion sources which completely dwarfs the sample when limited to measured line-of-sight velocities which is about $\sim$7.2 million or about 0.5%. It is typically difficult to get radial velocities for WDs since their spectra have few and broad lines, which means that working with pure proper motions is preferred in order to access a large sample of them. Doing this allows us to use a large sample of 129 675 WDs within 500 pc. Inferring the velocity distribution from proper motions and positions was done for *Hipparcos* data by Dehnen (1998) using a penalised maximum likelihood estimate. The method requires a sample that can be assumed to have proper motions uncorrelated to the on-sky positions. In this case the proper motions in one part of the sky compensate for the missing line-of-sight velocities of another. We applied this method and the related method of Dehnen & Binney (1998) to determine the velocity distributions and velocity dispersions for the WD population. Gaia DR2 had already shown that the WDs have a bifurcation in the colour-magnitude diagram, so the difference between the two sequences was something we chose to investigate. We were able to show that the bluer sequence has lower velocity dispersion, across all magnitudes where the bifurcation exists, than the redder sequence. This means that they comprise two separate kinematic populations. Furthermore, we determined the statistical independence of the two populations with a KS-test. The current best explanation for the bifurcation is atmospheric composition, which would not have a bearing on the kinematics. Our results, therefore, provide support for alternative explanations.

3. *Paper III: New stellar halo substructures from Gaia DR3 proper motions* - The third paper expands the use of the penalised likelihood estimate from Paper II. The benefits of using proper motion catalogues warranted further

> exploitation and so we decided to apply the method towards two new samples: the Solar neighbourhood and the local stellar halo. For the Solar neighbourhood, this results in 1 171 846 stars within 200 pc with 10% parallax uncertainty. This sample gives a very accurate view of what the velocity distribution looks like at 'face-value', with all of the most well-known moving groups featuring in the distribution. This also demonstrates that to find additional velocity substructure in the Solar neighbourhood special methods must be applied and in our case, we made use of conditional probabilities of one velocity component of the distribution upon the other. This effectively normalises the distribution along either the rows or the columns of the 2D map and reveals further structure in high-velocity regions. Selecting the local (within 3 kpc distance) stellar halo with a velocity cut of $v_{\mathrm{T}} > 200$ km s^{-1} provides us with 456 273 stars. This also reveals the double main sequences which have been previously identified in the colour-magnitude diagram in *Gaia* DR2 Gaia Collaboration et al. (2018b). The sequences are typically associated with a redder 'in-situ' halo and a blue 'accreted' halo which matches well a lower metallicity isochrone. This second sequence has been shown to have significant amounts of accreted substructure (see e.g., Koppelman et al. 2019 and links therein). We create a sample for each sequence with 239 115 and 194 507 stars in left and right sequences respectively. We focus on the accreted population and identify the majority of substructures available in literature. Using the conditional probabilities, we can identify two new features the the accreted halo which have no match in literature: *MMH-1* at $(v_r, v_\phi, v_\theta) \approx (\pm 220, 20, 300)$ km s^{-1} and *MMH-2* at $(v_r, v_\phi, v_\theta) \approx (-20, 180, -100)$ km s^{-1}.

Since the first of the articles is on dynamics in N-body simulations while the second and third are on statistical analysis of astrometric data, the thesis is divided into chapters reflecting this. Chapter 1 gives a structural overview of the Milky Way and explains radial migration. This follows naturally into Chapter 2 which summarises the first article. Chapter 3 gives historical context for the field of astrometry and background for the second and third article's method. Finally, Chapters 4 and 5 summarise the second and third articles respectively.

Chapter 1

The Milky Way as a Galaxy

> *"I know, it doesn't make any sense, I wish there were sense. Where did all the sense go?"*
> - Tribore, Final Space

1.1 Components

Throughout history, mankind has sought to understand the night sky and its many features such as stars, clumps, planets or 'wanderers'. But no feature is as large and noticeable as the great spray of stars that make up the Milky Way Galaxy, named so for the milk from Hera's breast in Greek mythology (Leeming, 1998). The suggestion that this milky band of stars was a rotating body that we, the observers, are inside of did not come until Wright (1750). Since then our understanding of our home Galaxy has increased tremendously and we can present stunningly detailed views of it like the map shown in Fig. 1.1. This map is made possible thanks to measurements from *Gaia*'s second data release (Gaia Collaboration et al. 2018a, hereafter DR2). As the figure shows, the Milky Way is composed of several different components with stars differing in spatial distribution, kinematics, chemistry, and age. In the three papers in this thesis, I touch upon almost every component mentioned in Fig. 1.1 and so I will provide a brief description of each one.

1.1.1 Thin disc

The thin disc is what visually makes up the Milky Way and, since it is where the Sun is located, it is the most well-studied of the stellar components. The thin disc is also the site of ongoing star formation which recent estimates place as high as $\sim$3.3 $\mathrm{M_{\odot}yr^{-1}}$ (Zari et al., 2022). As the name suggests it is relatively thin

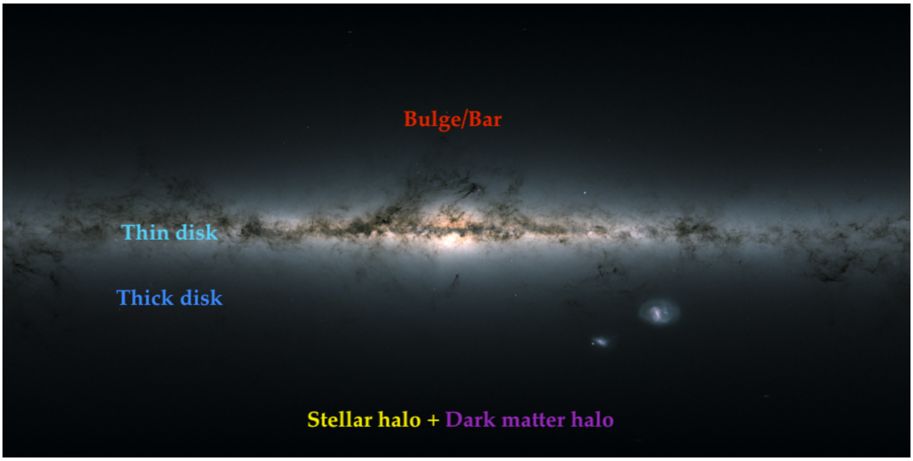

Figure 1.1: All-sky view of the Milky Way Galaxy from Gaia based on measurements of nearly 1.7 billion stars. We mark the location of different components of the Galaxy with different colours. Image adapted from *Gaia* Data processing and Analysis Consortium (DPAC) (CC BY-SA 3.0 IGO).

with a scale length of $R_\mathrm{t} \approx 2.6$ kpc, scale height of $z_\mathrm{t} \approx 300$ pc, and with a mass $M_\mathrm{t} \approx 3.5 \times 10^{10}$ $\mathrm{M}_\odot$ (Bland-Hawthorn & Gerhard, 2016). The thin disc stars are generally young and have abundances of elements produced by the α-process (Burbidge et al., 1957) relative to iron similar to the Sun. These elements have nuclei which are multiples of four, the atomic mass number of the Helium nucleus or α-particle. We measure the relative abundances relative to iron as:

$$[\alpha/\mathrm{Fe}] = \log_{10}\left(\frac{N_\alpha}{N_\mathrm{Fe}}\right)_\mathrm{star} - \log_{10}\left(\frac{N_\alpha}{N_\mathrm{Fe}}\right)_\odot , \tag{1.1}$$

where N is the number of atoms per unit of volume of the respective species.

1.1.2 Thick disc

The second disc of the Galaxy fulfills its name with a scale height of $z_\mathrm{T} \approx 900$ pc, scale length $R_\mathrm{T} \approx 2$ kpc, and mass $M_\mathrm{T} \approx 6$ $\mathrm{M}_\odot$ (Bland-Hawthorn & Gerhard, 2016). Its stars are older (Bensby et al., 2014; Martig et al., 2016) and kinematically hotter than those of the thin disc, since age and velocity dispersion are correlated (Martig et al. 2014; Aumer et al. 2016). In metallicity space, thick disc stars occupy regions of higher $[\alpha/\mathrm{Fe}]$ and are usually linked to the high-α sequence (Katz et al., 2021). How the thick and thin discs formed is still a debated topic, particularly so the former as explained in Helmi (2020) who also shows that the formation may be related to the evolution of the stellar halo through mergers with nearby galaxies.

1.1.3 Stellar halo

The most extended stellar component is the stellar halo which contains $1.3^{+0.3}_{-0.2} \times 10^{9}$ $\mathrm{M}_{\odot}$ within $2 < r < 70$ kpc (Mackereth & Bovy, 2020) and is host to the oldest and most metal-poor stars in the Galaxy (e.g., Da Costa et al. 2019; Horta et al. 2022). The orbits of halo stars are less flattened towards the disc and so can be told apart locally by their kinematics. Relative to the discs, the halo stars appear to move with a typical velocity of $\sim$200 km s^{-1}. A commonly used cosmological model is Λ cold dark matter (ΛCDM) which successfully explains, for example, the cosmic microwave background (Planck Collaboration et al., 2020) and the large-scale structure of galaxies (Springel et al., 2005). This theory also explains how stellar halos can form through hierarchical growth with minor and major mergers (White & Rees, 1978; Fall & Efstathiou, 1980). This view matches well with the current understanding of the stellar halo as having an *in situ* component of stars as well as an accreted component that becomes extremely dominant at larger distances from the disc (Naidu et al., 2020). It has also been shown that this accreted component has a plethora of substructures in it attributed to various accreted stellar populations (e.g., Koppelman et al. 2019; Feuillet et al. 2021; Dodd et al. 2022). We will touch more upon this in sections 5.2 and 5.3.

1.1.4 Dark matter halo

There is another halo that is not visible to our telescopes. If we only look at the stellar matter of a galaxy like the Milky Way, the rotational velocity of stars in its outer parts is expected to decrease with distance similarly to Keplerian rotation, in which $v_{\mathrm{rot}}^2 \propto M/R$. This is not what we observe however, and instead, the rotation curve flattens out which is attributed to the existence of a dark matter halo. Current results place the mass of the dark matter halo at $M_{\mathrm{dh}} \approx 1.3 \times 10^{12}$ $\mathrm{M}_{\odot}$ (Posti & Helmi, 2019) and its shape is still a topic of much debate as explained in McMillan (2017). While the debate is ongoing, it is very common in simulations to assume a spherically symmetric halo (e.g., Andersson et al. 2020).

1.1.5 The bulge

In the central regions of the Galaxy lies the bulge, heavily obscured by dust as is clearly visible in Fig. 1.1. The original explanation of the bulge was that of a spherical structure built up through early mergers, which is called a *classical bulge*. This also made sense given the old ages of bulge stars known at the time (Clarkson et al., 2008). More recent results have shown that the bulge has several different metallicity populations (Ness et al., 2013a) including young metal-rich stars (Ness et al., 2014). These younger stars instead suggest that the bulge could have formed through internal disk instabilities. Other works have also shown that parts of the bulge can be formed from the disc through interactions that slowly rearrange energy, angular momentum, and mass, otherwise known as *secular evolution* (Kormendy, 2013). Following star counts in the bulge, it has been established that the majority of bulge stars participate in a *box/peanut*-shaped structure, related to the three-dimensional Galactic bar, with cylindrical rotation (Wegg & Gerhard 2013; Ness et al. 2013b) and Shen et al. (2010) uses the kinematics to constrain its contribution to be less than 8% of the disc mass. In light of these discoveries, it is unclear if the Milky Way even has a classical bulge.

1.2 The bar & spiral arms

Beyond the components mentioned in the previous sections, there are the non-axisymmetric features. In other galaxies they are clearly visible but since we reside inside our Galaxy we struggle to see them as clearly. As an example, we show a simulated galaxy in Fig. 1.2 which has a bar and two spiral arms that can be seen very clearly and represents a typical disc galaxy. Since non-axisymmetric features play an important role in secular evolution we will take a closer look at these features in the Milky Way.

The boxy/peanut-shaped bulge mention in section 1.1.5 is an inner, vertical extension of the Galactic bar (Bland-Hawthorn & Gerhard, 2016). The bulge region reaches to about $\sim$2 kpc (Wegg & Gerhard, 2013) while the bar may reach as far as 5 kpc (Wegg et al., 2015). For this reason, it is sometimes referred to as the 'long' bar. Current estimates for the bar puts its mass at $\sim 1.6 \pm 0.3 \times 10^{10}$ $M_\odot$ (Kipper et al., 2020) and using Gaia's third data release (Gaia Collaboration et al. 2022b, hereafter DR3) the bar angle with respect to the Sun-Galactic Centre (GC) is estimated to be $-19.2^\circ \pm 1.5^\circ$ (Gaia Collaboration et al., 2022a). The bar is not static however and is rotating with a specific angular velocity, called its pattern speed. The pattern speed of the bar is subject to much debate with many

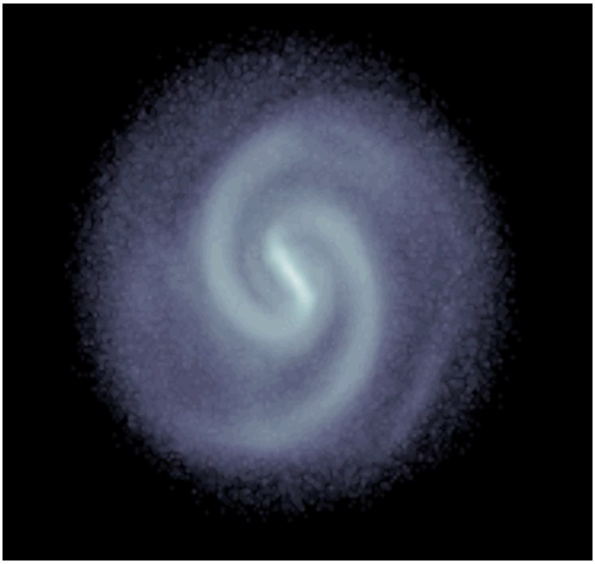

Figure 1.2: An example of a simulated Milky-Way like disc Galaxy with pronounced spiral arms and a central bar.

attempts at determining it. Bland-Hawthorn & Gerhard (2016) review many of the estimates and conclude with an estimated pattern speed of $\Omega_b \simeq 43 \pm 9$ km s^{-1} kpc^{-1}. More recent estimates place the pattern speed of the bar at $\Omega_b = 33.29 \pm 1.81$ km s^{-1} kpc^{-1} (Clarke & Gerhard, 2022) and $\Omega_b = 41 \pm 3$ km s^{-1} kpc^{-1} (Bovy et al., 2019; Sanders et al., 2019), in agreement with the previous value. Pattern speeds of this scale have been called a 'slow' bar scenario.

The other major non-axisymmetric feature of the Milky Way is the spiral arms. They likely wind around the whole disc and as such, we do not have a full picture of them to date and instead must look to whatever parts of them are visible to us from our position as observers in the Galactic plane. Current evidence within the community is that the Milky Way has four approximately symmetric spiral arms (Reid et al., 2019) rather than just two. The names for these four arms as in literature are *Perseus*, *Sagittarius-Carina*, *Scutum-Centaurus*, and *Norma-Outer*. The Sun is believed to lie between *Perseus* and *Sagittarius-Carina* in an inter-arm region. In addition to these arms, very close to the Sun lies the *local arm*, initially believed to be a spur of the *Perseus arm*. It has since been understood to be more similar to the nearby arms with comparable qualities and is perhaps a branch of one of them (Xu et al., 2013). In spiral galaxies, the highest densities of gas and

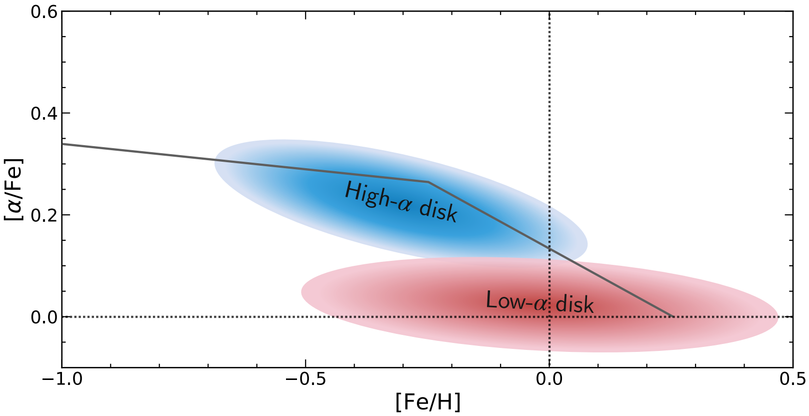

Figure 1.3: An illustration of the distribution of abundance of α-elements vs the abundance of iron. The dotted line shows the location of the Sun and the gray solid line the expected evolution of an isolated region of the ISM.

stars lie along the arms which is the site for most star formation in the disc.

1.3 Radial migration

Since the spiral arms and the Galactic bar are such very prominent features of our Galaxy and in other similar spiral galaxies, it is no surprise that they have a profound impact upon the disc in which they are found and the stars that live therein. One such effect which occurs because of the dynamical interplay between disc and the non-axisymmetric features is *radial migration*, which is the displacement of a star in the radial direction from the Galactic plane. We will soon explain the major processes which cause radial migration but first the importance of radial migration as an ingredient of galaxy evolution, and the evidence to support it, should be discussed.

Let us consider the chemical evolution of the Galactic disc. The abundances of α-elements and Fe over time in an isolated region of the interstellar matter (ISM) are affected by the life and death of its stars through what is called stellar nucleosynthesis (for a review see Edvardsson et al. 1993). In short, stars create elements and enhance the abundances of the next generation. Initially, core-collapse supernovae produce similar amount of α and Fe, but [Fe/H] increases. Eventually, type Ia supernovae begin, which produce Fe but no α-elements and thus in the region [α/Fe] starts to drop. This behaviour produces a trend like the grey line seen in

Fig. 1.3. If we are in a very isolated region, we would expect to see that the stars follow this narrow trend. Neighbouring regions radially inside and outside of the region would however have higher and lower [Fe/H] ranges as it has been shown that [Fe/H] increases radially inwards in the Galaxy (e.g., Hayden et al., 2015). In observations of the Solar neighbourhood (e.g., Edvardsson et al. 1993; Hayden et al. 2015; Bensby et al. 2014) we see a range of different Fe abundances at each [α/Fe], similar to the illustration shown in Fig. 1.3. Similarly, the age-metallicity relationship (AMR) can be expected to follow a narrow line for an isolated region but shows a wide scatter. This can be quite easily explained if the different regions of the disc are not isolated from each other, but rather there is radial mixing between them.

Beyond this rather straightforward example of radial migration, it has been suggested that several other observed features of the Milky Way disc are caused by it. These include the observed bimodality of $[\alpha/Fe]$ in plots like Fig. 1.3 (Schönrich & Binney, 2009; Toyouchi & Chiba, 2016) and the flaring of the outer disc in mono-age populations (Minchev et al., 2012). It is clear that some form of radial migration occurs in the Milky Way and we are today able to estimate the radial displacement of individual stars, such as in Frankel et al. (2018) who find that the Sun has likely migrated from a birth radius of $\sim$5.2 kpc. Therefore it is important to understand the processes by which migration occurs.

1.3.1 Radial heating

One rather simple cause of radial migration is what is called *radial heating*, sometimes called *blurring*. Stars are born in Giant Molecular Clouds (GMCs) which move on nearly circular orbits around the disc. This means that the stars themselves are born on nearly circular orbits. But through the evolution of stellar orbits, they can scatter by interaction with things like other GMCs, clusters, or spiral arms which will lead them onto slightly eccentric orbits, called *epicycle orbits* as they can be described by the *epicycle approximation*. The epicycle refers to the radial and azimuthal oscillations of the perturbed orbit, occurring with an *epicycle frequency*, κ. The reason a perturbed star does not simply move to a different radius when scattered is because of the fine balance between centrifugal and gravitational force keeping it in place. If the star is pushed radially outwards, the centrifugal force decreases faster than gravity and the star moves back in. The star now overshoots to an interior radius where the centrifugal force increases faster than gravity which pushes it back out. In other words, we say that the star is stable to small velocity changes. Because of the oscillations the star will visit different radii than its

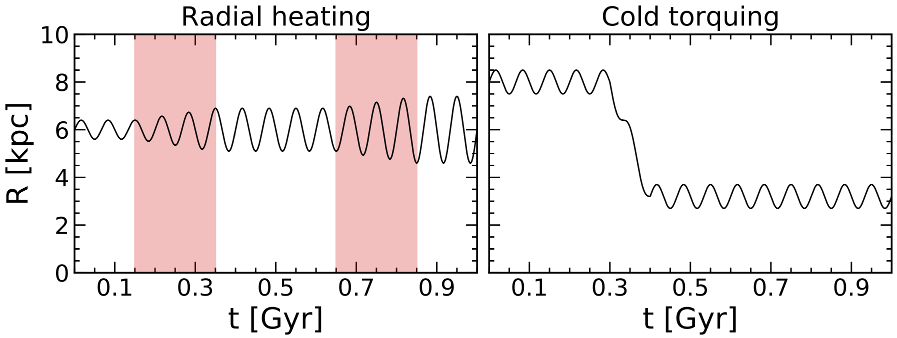

Figure 1.4: A simple sketch of the radial evolution of an orbit that undergoes migration. *Left*: The effect of radial heating or blurring, i.e. the increase of random motion due to dynamical scattering. This process increases or decreases the amplitude of the radial oscillations of the orbit. The shaded regions mark the time during which the radial heating occurs. The average radius, or guiding centre radius, R_g, is never changed during the process. *Right*: The effect of cold torquing or churning by scattering at a corotation resonance, which displaces the guiding centre radius, R_g, but does not increases the amplitude of oscillations and therefore does not increase the radial action, J_R.

original radius, called the *guiding radius*, $R_g = L_z/v_c$, where L_z is the angular momentum perpendicular to the disc and v_c is the circular velocity. It is the process of increasing the amplitude of the oscillations that we call radial heating and we show how this might look in the left panel of 1.4. The scattering process will not change the guiding radius on average but in the cases in which it does, this increases the random motions of the star, including the amplitude of the radial oscillations. In short, while the process of radial heating does not directly relate to a change in guiding radius, such a change can in certain instances also occur.

Given that the stars visit other regions of the Galaxy, they can obviously enrich those regions as well which leads to the conclusion that radial heating can contribute to the width observed in the chemical evolutionary tracks discussed in the previous section. It can, however, be shown, as in Binney (2007), that radial heating will only account for around 50% of the observed scatter in the metallicity and instead there must be some additional source of mixing to explain the measured scatter.

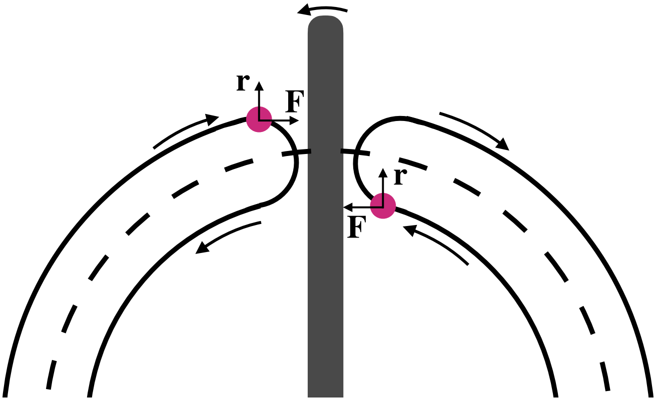

Figure 1.5: The concept of horseshoe orbits and angular momentum transfer near corotation of a non-axisymmetric feature with constant angular speed. The grey bar is a non-axisymmetric feature, with the Galactic centre towards its bottom. The dashed line marks the corotation radius and the pink points are positions along the horseshoe orbit right before angular momentum transfer. The vectors for $\boldsymbol{r}$ and $\boldsymbol{F}$ which gives the torque is indicated

1.3.2 Cold torquing

Another source of radial mixing was described first in a seminal paper by Sellwood & Binney (2002) where it was shown that disc heating is not the dominant effect of the spiral arms. Instead, non-axisymmetric features like the bar and spiral arms can shift the guiding radii of stars without significantly altering their dynamics. This process occurs through resonant interactions with the non-axisymmetric features. The spiral arms or bar will exert a torque that changes the angular momentum of the star's orbit since:

$$\frac{d}{dt}\boldsymbol{L} = \frac{d}{dt}(\boldsymbol{r} \times \boldsymbol{p}) = \boldsymbol{r} \times \boldsymbol{F} = \boldsymbol{\Gamma}. \tag{1.2}$$

Axisymmetric features like bars and spirals move with constant angular velocity, which means that the non-angular velocity increases further out. This means that for stars with approximately constant circular velocity there is a radius at which the velocity of a star and spiral/bar is the same, called *corotation*. Beyond this point, stars move more slowly than the spiral and within it they move faster. Faster stars catch up to the feature and will have a force, $\boldsymbol{F}$, directed towards it. Slower stars instead fall into it with a force in the opposite direction. We illustrate this in Fig. 1.5 which shows that for the fast stars, the torque will be directed inwards, i.e.,

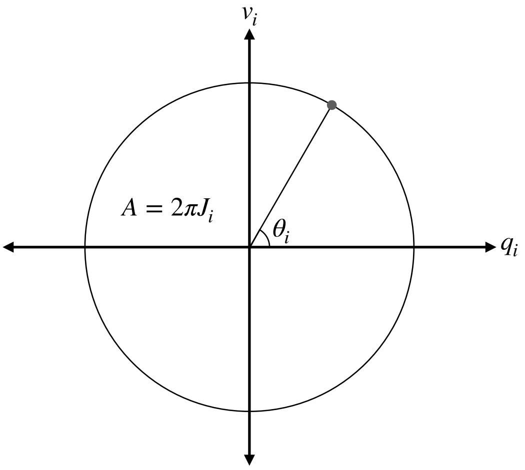

Figure 1.6: A polar coordinate analogy of action-angle variables to phase-space coordinate. An orbit oscillating in some coordinate q_i will have a velocity, v_i which also oscillates. A point on the same orbit can be described with a constant area, $2\pi J_i$, since the action J_i is a conserved quantity, and an angle θ_i.

negative which decreases the angular momentum and transfers it to a smaller R_g orbit where it moves faster. It eventually catches up to the spiral/bar and is given a positive torque, migrating outwards. In this simple view, the orbit would go back and forth but due to the transient nature of spiral arms and the plurality of axisymmetric features, this is not a likely outcome.

This provides the 'torquing' part. The cold part of the term comes from the fact that the migration does not increase the random motion of the affected stars, leaving them kinematically unscathed from the interaction. To properly explain this concept, we introduce *action-angle* variables to describe a stellar orbit. A simple polar-coordinate analogy is given in Fig. 1.6 which shows that an orbit in a certain dimension, i, can be described with two oscillating phase-space coordinates (q_i, v_i) or one constant and one oscillating, (J_i, θ_i). For disc orbits the three actions usually used are: J_r which describes the extent of the radial motion, J_z, the extent of the vertical motion, and J_ϕ which is equivalent to L_z.

If we place ourselves in the rotating frame of a Galaxy, moving with a pattern speed Ω_p relative to the inertial frame, we can describe its total energy or Hamiltonian, E_J, using the Hamiltonian of the inertial frame, E:

$$E_J = E - \Omega_p L, \tag{1.3}$$

Where L is the angular momentum. We call E_J the *Jacobi integral* (see Binney & Tremaine 2008 chapter 3.3.2 for a full derivation) and it is constant in time. So the difference in energy between two points in time is:

$$\Delta E = \Omega_p \Delta L. \tag{1.4}$$

Now we consider the energy separated into a radial and an azimuthal part

$$\Delta E = \frac{\partial H}{\partial L}\Delta L + \frac{\partial H}{\partial J_R}\Delta J_R, \tag{1.5}$$

where J_R is the radial action. If we use Hamilton's equations with $\boldsymbol{J}$ as the momentum and $\boldsymbol{\theta}$ as the coordinate we find:

$$\dot{J_i} = -\frac{\partial H(\boldsymbol{J})}{\partial \theta_i} = 0 \qquad \dot{\theta_i} = \frac{\partial H(\boldsymbol{J})}{\partial J_i} = \Omega_i(\boldsymbol{J}). \tag{1.6}$$

where Ω_i is an angular velocity. This can be understood considering the total energy or Hamiltonian of an orbit is a function of the action, but not of the angle; the energy does not change during an orbit. If the actions, which describe velocities and positions, change then of course so must the energy. We have that $\partial H/\partial J_r = \omega_R$ and $\partial H/\partial L = \Omega$, the radial and azimuthal frequencies. Combining this with eq. (1.5) gives

$$\Delta E = \Omega \Delta L + \omega_R \Delta J_r, \tag{1.7}$$

which when put into eq. (1.4) yields

$$\Delta J_r = \frac{\Omega_p - \Omega}{\omega_R}\Delta L. \tag{1.8}$$

It is the implications of eq. (1.8) that provides the 'cold' part.

Stars have almost constant circular velocity across the disc which means that angular momentum corresponds to guiding radius, (approximately, $L_z \propto R_g$). We know that torquing provides a change in the angular momentum from our discussion above, so this will correspond to a change in the radial action of the orbit unless the angular velocity of the star matches that of the axisymmetric feature, $\Omega = \Omega_p$, which is the case near corotation. This behaviour was demonstrated and detailed in Sellwood & Binney (2002) which showed also that the migration caused by the cold torquing can displace the star on kiloparsec scales, without imparting any increased random motions. The nature of cold torquing is therefore not only impressive but also frustrating since if stars can change their guiding radius by large scales without having any kinematic evidence of such a process, the history of different regions of the Galaxy becomes much more complex.

As an aside, it is worth mentioning the influence of other resonances that exist besides corotation. A particularly strong such resonance is when the radial frequency, ω_R (identical to κ in the epicyclic approximation), is a multiple of the frequency with which the star encounters the non-axisymmetric feature $(\Omega_p - \Omega)$. In other words when

$$\omega_R = \pm m(\Omega_p - \Omega). \tag{1.9}$$

These resonances are called *Lindblad resonances* after Swedish astronomer Bertil Lindblad (1895 - 1965). The value of m is set by the symmetry of the perturber. For example, $m = 2$ is a two-armed spiral or bar and $m = 4$ is a four-armed spiral. The positive sign corresponds to an orbit in which the rotating feature sweeps by the slower star as it completes m radial oscillations and is known as an *Outer Lindblad Resonances* (OLR). The negative sign is when the fast star rotates past the rotating feature by the time it completes its m radial oscillations and is then called an *Inner Lindblad Resonance* (ILR). At these resonances, we have from eq. (1.8)

$$\Delta J_r = \pm \frac{1}{m} \Delta L, \tag{1.10}$$

which shows how migration at these resonances increases the radial action, therefore making them a potential source of migration by radial heating as discussed previously.

Clearly, we must understand how stars are radially migrated. In particular, the process of cold torquing must be well understood since it is unique in the fact that it leaves no dynamical trace. Without these insights we cannot have a full picture of the history and evolution of our Galaxy.

Chapter 2

Paper I

2.1 Introduction

In my first paper, the aim is to establish the relationship between the efficiency of radial migration by cold torquing and the vertical action of stars. We seek to answer the question: do stars with large vertically extended obits migrate equally, or less efficiently, than those with smaller vertical extensions? Radial migration is a complicated process which can not be accurately described with an analytical expression. It is also a process which occurs over hundreds of millions of years, so we cannot observe it directly. For these reasons, we make use of numerical or 'N-body' simulations. In addition, using isolated disc galaxy simulations lets us have a great deal of control over the parameter space.

The paper particularly focuses on determining the efficiency of radial migration as a function of the kinematics of their orbits. This is not a topic that has gone entirely without study, of course. The efficiency of radial migration as a function of radial velocity dispersion is investigated in Solway et al. (2012), Vera-Ciro et al. (2014), and Daniel & Wyse (2018) who all agree that migration is reduced with increased radial motion. A similar trend can be seen when investigating vertical motion or vertical scale height. This is studied by several articles including Solway et al. (2012); Vera-Ciro et al. (2014); Halle et al. (2015); Vera-Ciro et al. (2016) and the conclusion is the same: radial migration is reduced with increased vertical excursion measured either through scale height or velocity dispersion. This is dubbed the *provenance bias* by Vera-Ciro et al. (2014). However, Solway et al. (2012) found that this effect was rather minor and was even used by Schönrich & McMillan (2017) as justification for migration to be independent of actions in their model. They also speculate on the difference between the works of Solway et al. (2012) and Vera-Ciro et al. (2014) being due to the strength and morphology of the spiral arms.

The idea of a provenance bias can be understood by considering the interaction between a star and a spiral arm. Cold, circular orbits will spend more time near the corotation resonance of the spiral and be more prone to migration. However, a sufficiently strong spiral arm from a massive stellar disc could perhaps be strong enough to migrate stars that reach larger vertical excursions as well. In Vera-Ciro et al. (2016) they create three different simulations of live discs in static dark matter halo potentials. These go from a lighter disc to a heavier disc, with the heavier disc resulting in fewer, stronger, spirals (D'Onghia, 2015). They claim that the provenance bias is present regardless of morphology which does not provide an explanation for the result of Solway et al. (2012).

In the paper, we seek to answer how this provenance bias is affected by spiral morphology and disc dominance. To do this, we generate a large number of N-body simulations where the ratio of the halo to disc strength is varied to produce discs with different strengths and morphology. We investigate the radial migration that occurs in these simulations and quantify it as a function of disc dominance. Specifically, we quantify the provenance bias of the migration. We determine that the slope of radial migration efficiency as a function of vertical action is itself a function of the dominance of the disc. The slope is steep for weaker discs (i.e., a provenance bias exists) and flattens for stronger discs, supporting the idea that strong spirals can migrate stars on vertically extended orbits. For radial action, we find that there is a provenance bias regardless of disc dominance.

2.2 Setting up simulations

All of our simulations are set up and run using packages available as part of the NEMO[1] (Teuben, 1995) toolbox. We start with a pure N-body isolated galaxy system designed to be similar to the Milky Way. The scale lengths and masses of components we use are chosen with inspiration from McMillan (2017). The full specifics of each component and the chosen parameters are found in paper I.

We follow the procedure of McMillan & Dehnen (2007) which describes the production of an equilibrium system of bulge, halo, and disc. The paper describes the procedure used in the NEMO package MKGALAXY, which in turn uses MKWD99DISC and MKHALO to create the different components. This disc has a

---

[1] `https://teuben.github.io/nemo/`

standard shape with a density profile that decreases exponentially in radius and has a sech^2 vertical profile:

$$\rho_{\rm disc}(R,z) = \frac{1}{2z_{\rm d}}\Sigma_0 \exp\left(-\frac{R}{R_{\rm d}}\right) {\rm sech}^2\left(\frac{z}{z_{\rm d}}\right). \tag{2.1}$$

The dark matter halo and bulge are both designed to have a spherical density distribution:

$$\rho(r) = \frac{\rho_0}{x_i^\gamma (x^\eta + 1)^{(\gamma_o - \gamma_i)/\eta}} {\rm sech}\left(\frac{r}{r_t}\right), \tag{2.2}$$

with the parameters chosen for the halo to provide a Dehnen-McLaughlin profile (Dehnen & McLaughlin, 2005) which has the advantage of being fully analytic with a smooth transition between inner and outer parts of the distribution. It also matches very well to simulated dark matter halos. The bulge uses a standard Hernquist profile (Hernquist, 1990).

Starting from these initial conditions we change only the mass of the dark matter halo. We create eleven different setups with halo masses ranging from 1.7×10^{11} M$_\odot$ to 1.02×10^{12} M$_\odot$ which corresponds to the ratio of the radial force from the halo to the disc, $F_{\rm h}/F_{\rm d}$, ranging from around 0.5 to 3.2 at $R = 8$ kpc and $z = 0$. In other words, we go from disc-dominated systems to halo-dominated systems. Each dark matter halo setup is also generated with ten different random seeds to estimate stochasticity, resulting in a total of 110 simulations.

2.3 Evolution of non-axisymmetric features

To capture the evolution of the simulated galaxies and their spiral arms and bars we use two approaches. The first is a direct visual inspection of the disc morphology in the plane of rotation at three different times, which correspond to 'early', 'evolved', and 'late' times or 0.3 Gyr, 1 Gyr, and 4 Gyr respectively. This is shown in Fig. 2.1. Since we are in a pure N-body simulation, we do not get much secular evolution beyond this time as the disk kinematics become too heated to participate in the dynamical interactions with the spiral arms. For this analysis we also only look at the lightest halo, 1.7×10^{11} M$_\odot$; the heaviest halo, 1.02×10^{12} M$_\odot$; and the one in between, 5.1×10^{11} M$_\odot$ as representative cases. This gives a disc-dominated case, a halo-dominated case, and something in between.

These simulations highlight that a very halo-dominated system leads to many, weaker arms rather than grand-design spirals and is unable to form a bar as well. In contrast to this, the disc-dominated system shows impressive arms, a bar, as

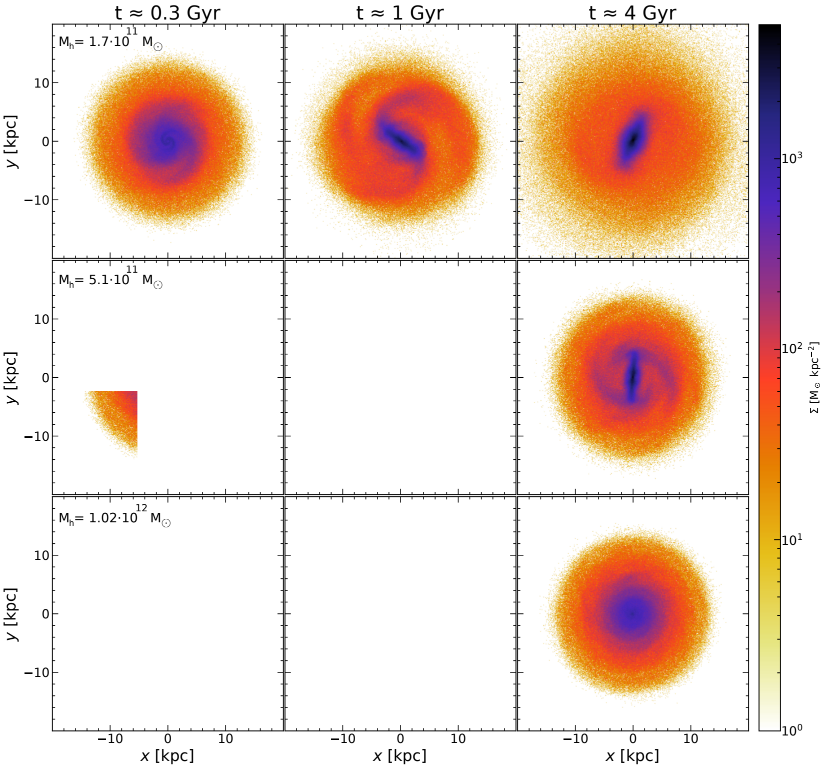

Figure 2.1: Three simulated galaxies seen face-on with masses: 1.02×10^{12} $\mathrm{M}_{\odot}$, 5.1×10^{11} $\mathrm{M}_{\odot}$, 1.02×10^{12} $\mathrm{M}_{\odot}$ in each row. The time of the snapshots for each column is indicated on the top. The different evolution of non-axisymmetric features is seen.

well as the heating mentioned before as the disc becomes extended by comparison to its quiescent counterparts.

The second approach is using a Fourier analysis to extract the power spectrum of different modes, m, or number of spiral arms ($m = 2$ is a two-armed spiral or bar). This method is described thoroughly in Roškar et al. (2012) and our paper. This analysis further strengthens what is already discussed above. The disc-dominated system sees a strong $m = 2$ resonance arise already at around 0.3 Gyr, probably a mixture between the spirals and bar. It has a pattern speed of $\sim$30 km s^{-1} kpc^{-1}, comparable to that of the Milky Way bar. The intermediate disc takes until after 2 Gyr to form a $m = 2$ feature with weaker multi-arm features prior to this time. Finally, the halo-dominated system barely sees any significant modes

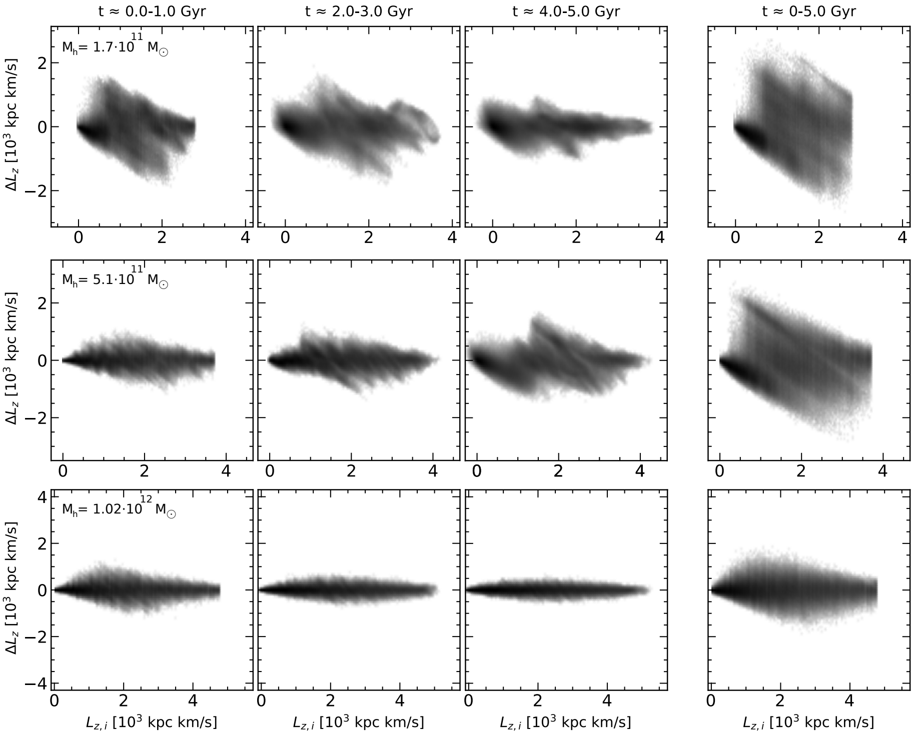

Figure 2.2: Change in angular momentum, ΔL_z, between two points in time as a function of initial angular momentum, $L_{z,\mathrm{i}}$. The rows correspond to the same simulations as in Fig. 2.1 and the time of angular momentum change is shown at the top. The amount of angular momentum change in each case is closely related to the evolution of strong non-axisymmetric features in the simulation.

appear apart from a very weak $m = 6$ feature briefly around 0.2 Gyr. Our results agree with D'Onghia (2015) that the disc-dominated systems form fewer, stronger spirals. This, of course, has implications for radial migration.

2.4 Quantifying radial migration

To gauge the amount of radial migration that occurs across the disc, we use a common approach of looking at the change in angular momentum, $\Delta L_z = L_z(t_2) - L_z(t_1)$, between two points in time t_1 and t_2. This can be compared against the initial angular momentum of the particles, $L_{z,\mathrm{i}}$, which is a proxy for the guiding radius. This is seen in 2.2 for the three simulations mentioned in sec-

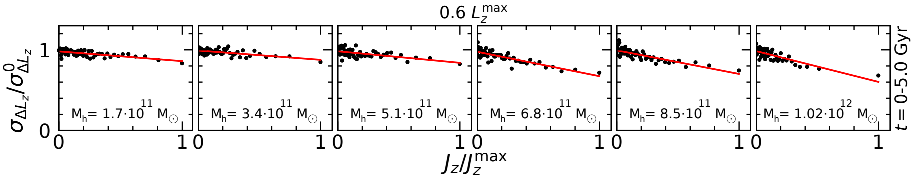

Figure 2.3: Change in angular momentum, ΔL_z, between two points in time as a function of initial angular momentum, $L_{z,\mathrm{i}}$. The rows correspond to the same simulations as in Fig. 2.1 and the time of angular momentum change is shown at the top. The amount of angular momentum change in each case is closely related to the evolution of strong non-axisymmetric features in the simulation.

tion 2.3 and shows how the strength of the secular features affects the migration. Note that diagonal features in this space corresponds to migration across a corotation resonance since particles interior to the resonance are migrated outwards, gaining a positive ΔL_z and vice-versa for the particles exterior. For example, consider the intermediate case. As was shown in the previous section, the bar forms not until after 2 Gyrs to form its largest $m = 2$ mode. We can see here that the most significant migration does not transpire until after this. We also see that the disc-dominated system has strong early migration which calms down as the disc has become heated. Since we have quantified the amount of migration as a function of angular momentum and shown how it relates to the disc morphology, we are equipped to tackle the primary question, the provenance bias.

We want to see how the migration changes as a function of the vertical action J_z across the disc. The particles are therefore binned 100x100 in the space of initial vertical action, $J_{z,\mathrm{i}}$, and initial angular momentum, $L_{z,\mathrm{i}}$. In each of these bins, the amount of migration occurring is quantified by the dispersion of angular momentum changes, $\sigma_{\Delta L_z}$, which we call the radial migration *efficiency*. We can then separate different bins in $L_{z,\mathrm{i}}$ into separate cases and investigate the behaviour of migration efficiency $\sigma_{\Delta L_z}$ as a function of initial vertical action $J_{z,\mathrm{i}}$. In the paper we use three values of $L_{z,\mathrm{i}}$ as representative of separate radial disc regions: 0.4, 0.6, and 0.8 of the maximum $L_{z,\mathrm{i}}$, corresponding to about 15 kpc. In this overview, we will show the $0.6L_z^{\max}$ case only. There are also inconsistencies between the simulations and in radius that require special attention. At smaller guiding radius particles reach much larger extents in vertical action due to the gravitational potential. To correct for this J_z is normalized such that it ranges from 0 to 1 with 1 corresponding to the largest extent in J_z. We also know that total migration is less in the halo-dominated simulations (as seen in Fig. 2.2). We wish to know how migration is biased to higher vertical actions, rather than how much migration occurs in total, and so we also normalize $\sigma_{\Delta L_z}$ by dividing it by its value at $J_z = 0$ km s^{-1} kpc^{-1}. The result as seen in Fig. 2.3 allows us to determine the slope in this space, which is a measure of the provenance bias. A flat slope means that migration is equally efficient at all values of J_z and a strong negative slope means that migration preferentially affects low J_z particles.

This result shows that the provenance bias is a function of the disc dominance of the simulated system. We see the same trend in the slopes at the two other angular momentum slices considered, $0.4L_z^{\mathrm{max}}$ and $0.8L_z^{\mathrm{max}}$. We compare our results with Vera-Ciro et al. (2016) by reproducing their Milky Way-like simulation and altering the disc dominance through the disc mass. We then apply our analysis approach to these simulations and quantify the migration in the same way as for our own simulations. This leads us to the same conclusion as above: the slope of migration efficiency flattens with disc dominance. The fact that we see this and they do not is likely because of the lengths we go to in order to quantify the migration. We also investigate the radial bias of migration efficiency to find that there is a provenance bias that is independent of disc dominance, suggesting different responses to cold torquing efficiency with increased action in the disc plane instead of orthogonal to it.

These results have significant implications for galaxy evolution. If stars on vertically extended orbits, which are typically older, can be migrated then any interpretation of stellar distributions as a function of age is contaminated. The results also provide necessary constraints for analytical modelling of radial migration, which is a necessary part of any analytical galaxy evolution model.

Chapter 3

Motions of stars

"The stars are far brighter, Than gems without measure."
- J. R. R. Tolkien, The Hobbit

3.1 The oldest science

The fascination of mankind with the celestial sphere has undoubtedly been around for far longer than historical records can demonstrate. Beyond a scientific curiosity, the night sky has had practical purposes that have been used throughout history. Polaris points the way north for travellers of all sorts. The blurring of stars can tell sailors that it is windy at sea. Agriculture heavily relies on the use of calendars based around the Sun and Moon. The relationship between astronomy and humans was arguably more tangible and transparent in the past than it is today when non-astronomers do not need to think about these matters very often.

In the last few decades, the study of prehistoric astronomy has boomed into its own field called archaeoastronomy and revolves around the study of prehistoric sites and their possible astronomical association (see Magli 2020 for a review). These sites have origins dating back several millennia BCE. The earliest historically verified accounts of astronomy come from Mesopotamia and the ancient kingdoms of Sumer, Assyria, and Babylonia. From this region have been found clay tablets noting down positions and locations for constellations and planets. One significant example of such is the *Mul-Apin* clay tablet, shown in Fig. 3.1, which dates back to a little over 1000 BCE (de Jong, 2007).

Around 200 BCE the first star catalogue was made by *Hipparchus* in ancient

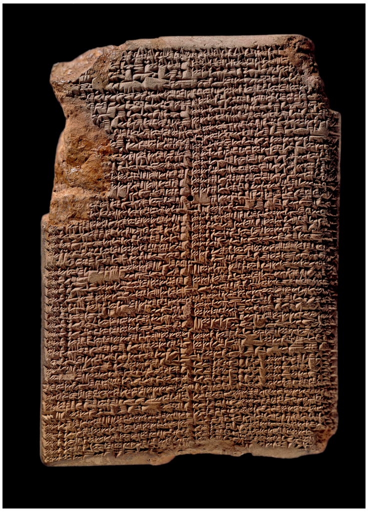

Figure 3.1: The Mul-Apin clay tablet, tablet 1. The tablet has sections locating constellations in relation to each other and lists stars and constellations according to celestial latitude among other entries. © The Trustees of the British Museum. Shared under a Creative Commons Attribution-NonCommercial-ShareAlike 4.0 International (CC BY-NC-SA 4.0) licence.

Greece[1]. This catalogue contained positions of stars and is often linked to the birth of *astrometry* as a subject, the study of positions and movements of celestial bodies with precise measurements. As the Roman empire fell and the Dark Ages began, astrometric advances were made to wait. In 1428 a 36-meter sextant was constructed in Uzbekistan by the grandson of the Mongol conqueror Tamarkand, *Ulugh Beg*. This provided a new star catalogue of 994 stellar positions accurate to a degree. The next advancement came from Scandinavia as *Tycho Brahe* (1546-1601) on the Danish island of Hven, using a quadrant of around seven meters at his Uraniborg observatory, measured a thousand stellar positions. His accuracy reached about $20''$. In order to perfect the art of navigation, it was necessary to determine the longitude of various places. For this purpose, the Royal Greenwich Observatory was founded in 1675 and its first Astronomer Royal was *John Flamsteed* (1646-1719), tasked with determining the motions of the heavens. After his passing was published a catalogue of 2935 stellar positions accurate to $10''$-$20''$, the *Historia Coelestis Brittanica* (Flamsteed, 1725), the first catalogue using

---

[1] The history of astrometry is described in much greater detail in Perryman (2012) than it is here and we encouraged the interested reader to have a look.

a telescope. This expanded rapidly thereafter and had reached 50 000 stars with $3''$accuracy in *Histoire Céleste Française* by *Jérôme Lalande* (1732 - 1807) (de Lalande, 1801).

The next step is not an increasingly large catalogue. Instead, through separate works by *Wilhelm Struve* (1793-1864), *Friedrich Bessel* (1784-1846), and *Thomas Henderson* (1798-1844) the first stellar parallaxes (ϖ) were published between 1837 to 1839. The parallax is the apparent angular displacement of an object due to the displacement of the observer. When driving down a highway, you will notice that as you move, the mountains in the background move more slowly across your field of vision than the trees by the side of the road. This angular displacement is the parallax, larger for nearby objects, and smaller for more distant ones. The same can be done for the stars, as the closer a star is the more it is displaced across the celestial sphere as the Earth orbits the Sun. The distance to stars based on their apparent motions could now be measured, albeit for individual stars at first. It is worth noting the scale of these distances. Bessel's measurement of 61 Cygni's parallax was $0.314''$, corresponding to $\sim$3 pc or roughly 90 trillion kilometres. The enormity of the Universe could no longer be questioned. During the next century and a half, the number of available ground-based parallax measurements grows rapidly and culminates in 1995, when the *Yale Trigonometric parallax Catalogue* is published by *William van Altena* (van Altena et al., 1995). The parallax measurements are then limited to an accuracy of $0.5''$ due to the flickering of the Earth's atmosphere which is reduced to $0.01''$ when averaging over many measurements. One workaround is adaptive optics, distorting the mirror to compensate for the atmosphere, which is used in the GRAVITY instrument (Eisenhauer et al., 2011) to achieve up to $0.003''$. Even then however, the entire sky cannot be covered. Furthermore, it is not the most precise astrometry we can get. Further precision requires that the next advancements be made using space telescopes.

3.2 Hipparcos & Gaia

In 1989, following a little over two millennia of astrometric catalogues, the first astrometric satellite was launched by ESA with the name *Hipparcos*, named after the author of the first catalogue. Eight years later the catalogue was published in Perryman et al. (1997), containing positions, proper motions (the on-sky angular motions), and distances for 117 955 stars, accurate to a milliarcsecond (mas). This mission was also used to produce the lower-precision Tycho catalogue (named for Tycho Brahe), which expanded the number of stars with proper motions and positions to 2.5 million (Høg et al., 2000). The scientific gifts of Hipparcos were many, and the achievements made possible are reviewed in Perryman (2009).

The opportunities awarded to astronomers by Hipparcos perhaps left the community hungry for more because not long after, in 2013, its successor was launched and was designed to provide the single largest improvement on past available astrometry, by a wide margin. This mission is called *Gaia* (Gaia Collaboration et al., 2016a) and currently provides the largest available set of astrometric data.

The Gaia mission has so far had three full data releases (DRs). DR1 (Gaia Collaboration et al., 2016b) released with the five-parameter astrometric solution (positions, parallax, proper motions) for 2 million sources. The total number of sources was closer to 1.1 billion, but getting the astrometric solution using one year's worth of data required the adoption of the *Tycho-Gaia Astrometric Solution*, described in Michalik et al. (2015). Two years later DR2 (Gaia Collaboration et al., 2018a) released with $\sim$1.3 billion five-parameter sources. Not only that, but the onboard spectrometer provided $\sim$7.2 million radial velocities, completing the full 6D phase-space information for these stars in addition to 3D position with on-sky velocities. Two years later again, the Early Data Release 3 (Gaia Collaboration et al., 2021) arrived with five-parameter solutions for $\sim$1.4 billion sources. The radial velocities came with DR3 (Gaia Collaboration et al., 2022b) and we now have $\sim$33 million sources with RVs. The precision of Gaia is of course also a massive improvement on that of previous catalogues. From brightest to faintest sources, Gaia now has an uncertainty of 0.01-1 mas in position, and 0.02-1.3 mas in parallax, 0.02-1.4 mas yr^{-1} in proper motion. The astrometry of the faintest stars is about as accurate as Hipparcos could provide for any star, and the ratio of sources in Hipparcos to those in Gaia is about $8 \times 10^{-5} : 1$, representing an increase of about 12 000 times.

In addition to astrometry and spectroscopy, Gaia also provides photometry, variable sources, as well as some parameters for Solar system objects[2]. Gaia is not done quite yet and the future is sure to be exciting with a successor mission being planned which would conduct astrometry in the infrared (Hobbs et al., 2021). It does not seem like the exponential growth of astrometry is stopping anytime soon, much to the benefit of our understanding of the universe.

For everything Gaia does well, we need to discuss a shortcoming of the data with respect to studying Galactic dynamics that is central to the work in Papers II and III. Radial velocities were not available in the Gaia catalogue until DR2, and

---

[2] For a more exhaustive list of everything in the data releases, see the 'info' section of each release on `https://www.cosmos.esa.int/web/gaia/data`

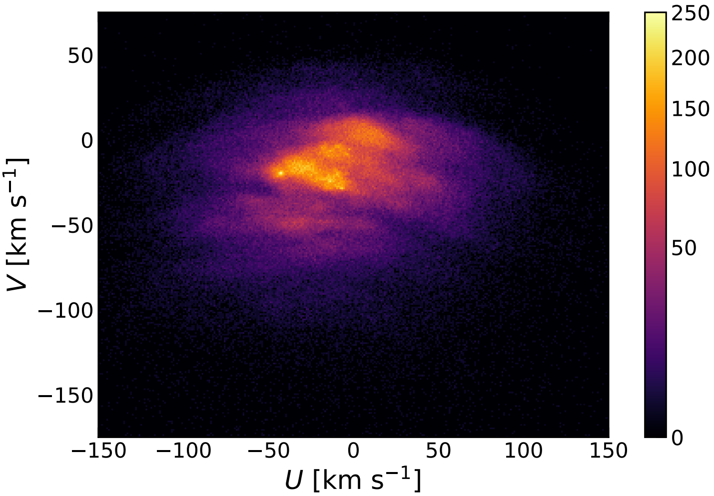

Figure 3.2: The number density distribution of sources from DR3 with radial velocities in the Solar neighbourhood. There is clearly a great deal of structure present already in close proximity to the Sun. The colour scale shows $\sqrt{N}$ and the axes show Galactic velocities U, towards the Galactic centres, and V, in the direction of Galactic rotation.

when released was only available for about 0.5% of the astrometric solutions. This was slightly improved with DR3, which reached closer to 2%. This still leaves the vast majority of the data without 6D phase-space information. Full phase-space information is important because, as Dehnen (1998) puts it, ”*The dynamical state of a stellar system is completely described by its phase-space distribution function* $F(\boldsymbol{x}, \boldsymbol{v})$”. Practically we cannot determine the full distribution in a realistic way and instead, we seek to determine more local variations of the velocity distribution $f(\boldsymbol{v})$.

Now comes the issue; we do not have 3D velocities for the majority of these sources. How can we hope to determine the velocity distribution? To begin with, we can simply work with the sources that have radial velocities. This has been done of course and for DR2 it was in one of the demonstration papers, (Gaia Collaboration et al., 2018c). We use DR3 to recreate the same plot here, using a similar Solar neighbourhood sample we have around 500 000 stars, whereas in DR2 the sample contained ∼350 000 stars. The velocity distribution can be seen in Fig. 3.2. This figure shows us that the velocity structure of the Galaxy, even locally, is anything but straightforward. Structure in velocity space can be caused by a variety of processes (see, e.g., Antoja et al., 2010). Originally it was thought to come from disrupted stellar clusters. Newer suggestions have been accreted dwarf galaxies and close passings by external galaxies. Last but not least, the resonances of the spiral arms and bar, as discussed in the context of Paper I, can cause substructure in velocity space as well. We can with ease understand how decoding the velocity structure of the Galaxy will provide valuable insight into its evolution and history. It is therefore vital that we have access to as many stars as possible.

So what about the remainder of the sources? It turns out that all hope is not lost. Already in Dehnen (1998) the velocity distribution from Hipparcos was determined, despite the lack of radial velocities, by employing a clever approximation of a velocity distribution which is isotropic across the sky and then inferring $f(\boldsymbol{v})$ with a penalized maximum likelihood estimate (MPLE) (we will return to this in section 4.3). Similarly the average velocities and the velocity dispersion were determined in Dehnen & Binney (1998). Other studies that work around the absence of measured radial velocities include Antoja et al. (2017) with estimates of disc velocity asymmetries, Koppelman & Helmi (2021) who determined the Milky Way's escape velocity, and McMillan et al. (2022) who looked to the outer parts of the disc near the anti-centre and showed that the velocities exhibit properties that match well with being perturbed by a dwarf galaxy. At least for now, it is necessary to use proper motion-limited samples if we wish to have access to catalogues that span a greater part of our Galaxy, and if we wish to have access to all kinds of stars.

The astrometric renaissance is now and it is an exciting time for all fields of astronomy that can make use of the impressive data that is not only currently released but is sure to arrive in the foreseeable future.

Chapter 4

Paper II

4.1 Introduction

In Paper II we deal with the velocity distribution of local stars which was discussed in the previous chapter. Specifically, we determine the velocity distribution and velocity moments of Solar neighbourhood white dwarfs (WDs) in Gaia EDR3. In order to do this, we make use of the methods derived in Dehnen (1998) and Dehnen & Binney (1998) the first of which has not been employed for the *Gaia* data prior. Since the method does not rely on any measurements of radial velocity the WDs are ideal candidates since they very rarely have such measurements available.

The velocity distribution is a powerful tool to decode the evolution of the Milky Way's components, as the community has been able to show in the past few decades. Recent research has been able to show a staggering amount of substructure in the velocity distributions (Antoja et al., 2012; Kushniruk et al., 2017; Gaia Collaboration et al., 2018c) where we can see individual velocity structures up to hundreds of km s^{-1} away from Solar motion as well as horizontal arches in (U, V) that span across the distribution. In addition to classical motions in U, V, W, the field has grown to include distributions in actions and angles, called orbit space (e.g., Trick et al. 2019, 2021; Trick 2022). In orbit space, we can see clear ridges that are linked closely to the various structures in velocity space. Going forwards, both of these spaces will be important to understand the dynamical structure of the Milky Way.

The velocity distribution of WDs has, as mentioned, not been as easy to probe as that of the rest of the stars in the Solar neighbourhood. This leads to smaller samples which a couple of decades ago were only in the few hundreds (Sion & Liebert, 1977; Sion et al., 1988) and more recently samples which range from a couple of thousand to a few tens of thousands (Rowell & Hambly, 2011; Anguiano et al., 2017). Recent works that investigate the kinematics of WDs are Torres et al. (2019) who used Gaia to identify the *Hercules* stream in the WDs and Raddi et al. (2022) who determined the age-velocity dispersion relation of WDs. These samples are about as large as any that have been used, with $\sim$14 000 and $\sim$3000 for the two papers respectively. In my second paper, our method provides us with a sample of 129 675 WDs, the largest to date. We use this sample to identify known substructures as well as some novel features in velocity space. In addition to this, we also manage to identify two kinematically separate WD populations, which are attributed to two parallel cooling sequences seen in the colour-magnitude diagram (CMD) of WDs and demonstrated in section 4.2. We tentatively linked this to recent star formation which, it has been suggested, matches the times of flybys of nearby dwarf galaxies (Ruiz-Lara et al., 2020).

4.2 White dwarfs

Stars can be called 'nuclear foundries', as they fuse hydrogen into helium, 'shaping' metals from other metals through nuclear processes. This process creates outward thermal pressure which holds the star up against gravitational pressure in hydrostatic equilibrium. The hydrogen is not infinite and eventually runs out and the star contracts, shedding its outer layers while the core begins fusing helium into heavier elements, creating a planetary nebula around it. For massive stars, the core is large enough that many heavier elements can start fusing but for stars between about $0.6 - 10\ \mathrm{M}_\odot$, at some point this is insufficient and 'electron degeneracy'[1] occurs and provides the necessary outward pressure. The star no longer fuses and all that is left is the core, a stellar 'corpse' called a white dwarf. This is the fate of 97% of all stars in the Milky Way (Fontaine et al., 2001). The WD will live for a long time, but cools slowly, growing fainter and redder over time which can be seen in the CMD of WDs, shown in Fig. 4.1. The WD will be difficult to observe photometrically, as it is rather faint, and spectroscopically, due to the metals sinking below the observable photosphere as well as thermal broadening.

Despite this, Gaia is able to observe quite a large number of WDs photometrically. In the Solar Neighbourhood (within 500 pc) we can, after some quality cuts, find about 130 000 WDs in EDR3. However, if we use an even closer sample

---

[1] Electron degeneracy pressure and more is explained in Kippenhahn et al. (2012)

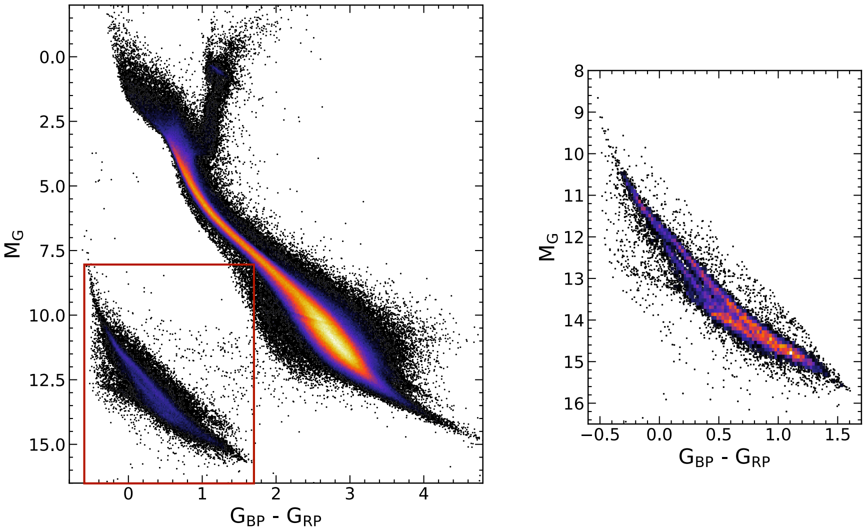

Figure 4.1: Colour-magnitude diagram of stars available as part of the Gaia data. The colour shows the square root of the number density. The left panel shows all stars in DR3 that are within 200 pc overlaid with a 500x500 histogram. The red box shows the WD region which is then shown on the right in a similar style but for stars within 100pc and with increased bin width. A separation into two sequences can clearly be seen.

limited to 100 pc, we can observe that the WD sequence is in fact not singular, but split into two. This result was first identified in Gaia Collaboration et al. (2018b) and has had two major suggestions put forth to explain it. Explanation **a)** suggests that the second sequence arises due to atmospheric differences in WDs. The upper, redder, sequence have hydrogen-dominated spectra (called DAs and constitutes ∼80% of observed WDs) whereas the lower, bluer, sequence contains WDs with Helium (called DBs) or heavier elements dominating their atmospheres. We can refer to this simply as DAs or non-DAs for the purposes of Paper II. For a full description of spectral classes of WDs and their meaning, see table 4.1[2] This explanation has shown to be able to explain the CMD bifurcation very well in works like that of Kilic et al. (2018, 2020) and Gentile Fusillo et al. (2019). Another recent discovery about the WDs is that their mass distribution is bimodal, with a main Gaussian centred on ∼0.6 $M_\odot$ and a secondary, smaller Gaussian around ∼0.8 $M_\odot$ (e.g., El-Badry et al. 2018; Kilic et al. 2018, 2020). This led to the expla-

---

[2] The 'D' in the spectral classifications stands for degenerate.

Table 4.1: Spectral classification of white dwarfs. The name of the spectral class and its definition.

Spectral class	Definition
DA	Hydrogen dominated spectrum
DB	Helium dominated spectrum
DC	Continuous spectrum, featureless
DO	He II and He I or H features
DZ	Metal lines dominate spectrum
DQ	Carbon lines dominate spectrum

nation **b**) that the second sequence could consist of heavier mass WDs, which have fainter and bluer cooling tracks. In single-star evolution, the more massive WDs would come from more massive progenitors, which then become WDs much on shorter timescales. For this reason, they would have colder kinematics due to the age-dispersion relation (Aumer et al., 2016). Mergers were suggested as a source of massive WDs but was ruled out by Kilic et al. (2020) who failed to discover significant massive WDs with hot kinematics. Instead El-Badry et al. (2018) shows that with the right choice of initial-final mass relation and continuous star formation, the second sequence can be populated by late-forming WDs. In summary, the second sequence can be explained as massive WDs formed recently. The two scenarios can be distinguished by their kinematics. The atmospheric composition should not have any bearing on the kinematics while, as explained above, the mass of WDs does. Therefore, we can investigate the kinematics of the two populations and try to provide insight into the cause of the CMD bifurcation.

4.3 Inferring f_v

As shown in Dehnen & Binney (1998), the mean motion $\langle \boldsymbol{v} \rangle$ and velocity dispersion $\boldsymbol{\sigma}$ can be determined for a sample of stars given a few caveats. The on-sky positions have to be uncorrelated with the velocities, which means that we see the same velocity distribution regardless of where on the sky we look. Consider the regions shown in Fig. 4.2. If there is a general mean motion for all parts of the sky, the line-of-sight motion of the red region will be given by the tangential motion of either pink or green regions in the direction of the red region, shown here using red arrows on the pink/green regions. Conversely, the tangential motion components of the red region that points to the left and right will give, approximately, the line-of-sight motion of the other two components, as indicated by the

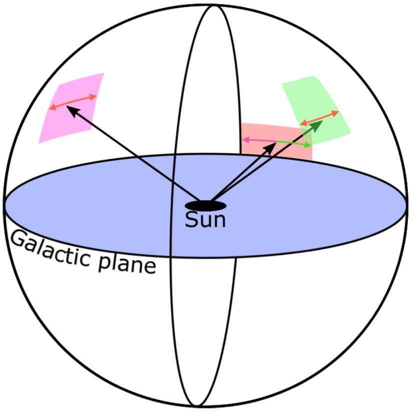

Figure 4.2: An illustration of positions on the celestial sphere from the point of view of a Solar system observer.

colouring of the arrows.

The same concept was used for the even more impressive feat of inferring the velocity distribution of Hipparcos stars in Dehnen (1998). We can write the probability distribution of tangential or transverse velocities in a given direction $\hat{\boldsymbol{r}}$ as $\rho(\boldsymbol{q}|\hat{\boldsymbol{r}})$ where $\boldsymbol{q}$ is the 2D vector of tangential velocities. To relate this distribution to the full velocity distribution we can write

$$\rho(\boldsymbol{q}|\hat{\boldsymbol{r}}) = \int \mathrm{d}v_r f(\boldsymbol{v}) = \int \mathrm{d}v_r f(\boldsymbol{p} + v_r\hat{\boldsymbol{r}}), \tag{4.1}$$

where $\boldsymbol{p}$ is the 3D projection of the tangential motion. The true distribution can of course not be determined precisely using transverse motion alone but it can be estimated with a log-likelihood maximization of some model of it. We do this numerically by defining the velocity distribution to be

$$f(\boldsymbol{v}) = e^{\phi(\boldsymbol{v})}, \tag{4.2}$$

where $\phi(\boldsymbol{v})$ is given on a 3D velocity grid with $L_U \times L_V \times L_W$ cells with widths $h_U \times h_V \times h_W$. The final expression for the function we seek to maximize, as a function of $\phi(\boldsymbol{v})$, is:

$$\tilde{\mathscr{Q}}_\alpha(\boldsymbol{\phi}) = \overbrace{N^{-1}\sum_k \ln\left[\sum_{\boldsymbol{l}} e^{\phi_{\boldsymbol{l}}} K(k|\boldsymbol{l})\right]}^{\text{Sum of PDF}} - \underbrace{\sum_{\boldsymbol{l}} e^{\phi_{\boldsymbol{l}}}}_{\text{Normalizing term}} - \overbrace{\frac{1}{2}\alpha h_x h_y h_z \sum_{\boldsymbol{l}} \left(\sum_{\boldsymbol{n}} \phi_{\boldsymbol{n}} \Xi_{\boldsymbol{nl}}\right)^2}^{\text{penalizing term}}. \tag{4.3}$$

Here, N is the sample size, α is the smoothing parameter, $(\sum_{\boldsymbol{n}} \phi_{\boldsymbol{n}} \Xi_{\boldsymbol{nl}})$ is a numerical approximation for the second derivative of $\phi(\boldsymbol{v})$ for a given cell. This term, therefore, penalizes unsmooth solutions and is scaled by the smoothing parameter, α. For each star k, $K(k|\boldsymbol{l})$ is the length of the line $(\boldsymbol{p} + v_r\hat{\boldsymbol{r}})$ in velocity space through each cell, $\boldsymbol{l}$, formed by its tangential velocity and all possible radial velocities.

To determine α, we make use of a calibration sample of main sequence stars in the Solar neighbourhood that had measured radial velocities from *Gaia* DR2. We select some reasonable range of test values for α and run the maximization on this sample. Since we know the velocity distribution of this calibration sample, we can then choose the α that best reproduces it. Since the best choice of α depends on sample size, the calibration sample is picked so as to have about the same number of sources as the WD sample and uses an identical grid.

We chose a grid of $\boldsymbol{n} = [100, 100, 72]$ cells with velocity ranges:

$$\begin{aligned} U \in& [-150, 150] \text{ km s}^{-1} \\ V \in& [-150, 50] \text{ km s}^{-1} \\ W \in& [-80, 60] \text{ km s}^{-1}, \end{aligned}$$

which provides a resolution of about $\Delta v = [3, 2, 2]$ km s^{-1}. The algorithm is also set up to use a so-called multigrid approach, where the solution is first found on a coarser grid which is interpolated and used as an initial guess for the maximization on a finer grid. This refinement occurs $3 - 5$ times depending on the grid size.

We split the WD sample along the bifurcation in the colour-magnitude diagram (between 12th and 14th magnitude where it is strongest) as well as into three equally sized magnitude bins, which we simply call *A*, *B*, and *C* from brightest to faintest. The resulting velocity distributions in (U, V) are seen in Fig. 4.3. While the other velocity projections are also calculated (and shown in the paper) the (U, V) space shows the most structure. The overall shape can be quickly identified to match well with the known distribution of the main-sequence stars as seen in Fig. 3.2. The magnitude bins can be seen increasing in velocity dispersion as they go from *A* to *C*, reflecting the age-dispersion relation. As the dispersion becomes larger, *C* appears to have arch-like features as well, marked in the plot with red lines. The relative distributions on the third row have an unexpected result. We naturally would expect the more centrally fixated samples *A* and *B* to dominate close to the origin and *C* would dominate further out. This is mostly the case apart from a small region around $(U, V) \approx (7, -19)$ km s^{-1}. The region does not match conclusively with any known moving group and only Kushniruk et al.

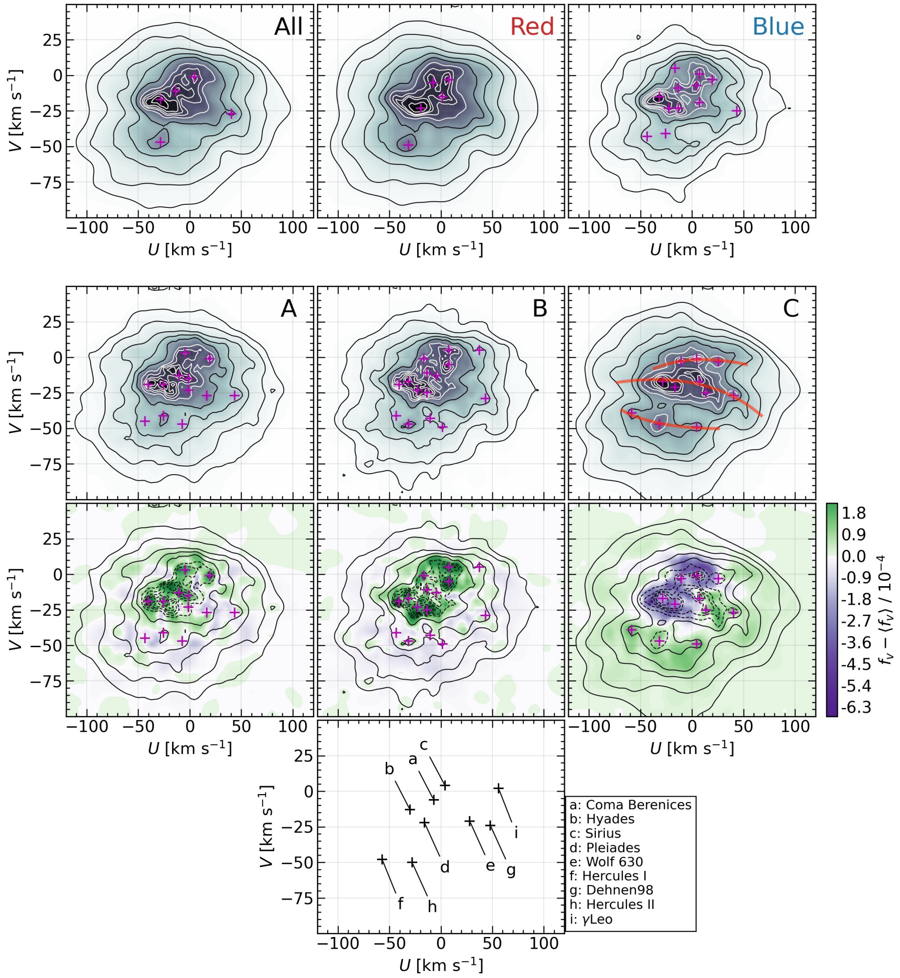

Figure 4.3: Velocity distributions of the WDs in the $U - V$ plane. Purple crosses show identified features. Shown also are the different sub-samples with the top row showing the different bifurcated sequences, the middle row shows the magnitude bins mentioned in section 4.3. The bottom row shows the distribution of the same magnitude bins subtracted by the mean of the three distributions, to highlight where each bin is strongest or weakest. At the bottom are shown the first nine groups identified in Antoja et al. (2012) for comparison.

(2017) provides a nearby link to *Coma Berenices* which has a suggested dynamical origin from a pericenter passing of the *Sagittarius* dwarf galaxy in Monari et al. (2018).

The regions on either side of the CMD bifurcation are seen in the top row and show similar dynamical features. However, the velocity dispersion of the red

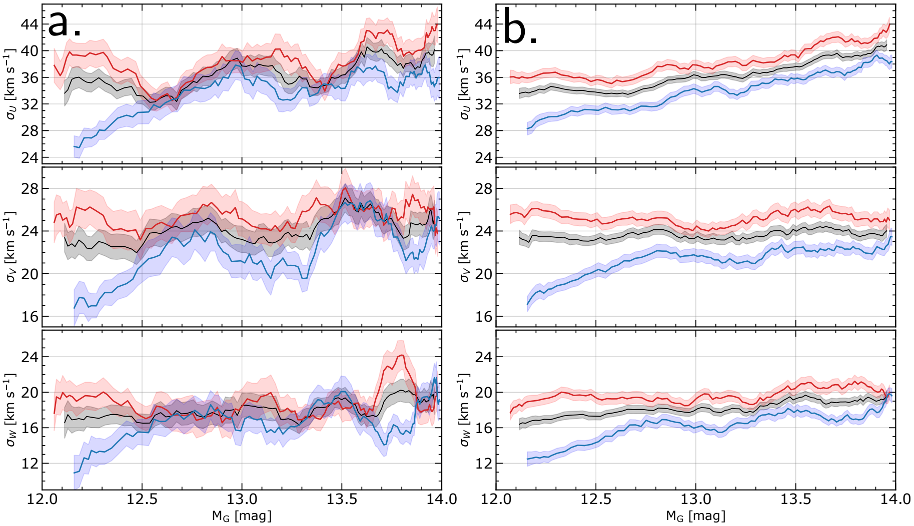

Figure 4.4: Moving velocity dispersion calculated in the three directions of U, V, and W, for the bifurcated sequences between 12th and 14th magnitude where they are visible. *a.* shows the moving dispersion for the red and blue sequences as well as the joint sample using WDs which are closer than 100 pc. The shaded regions show the 1σ uncertainty regions. *b.* same as the a. but for WDs up to 200 pc. Both plots show clearly a separation between the red and blue samples and when the 200 pc sample is used, they barely even overlap within 1σ.

sample is clearly larger than the blue. This hints at hotter kinematics and as such, we look to the dispersion of the samples rather than the full distribution for further analysis.

4.4 Two kinematic populations

We use the same method as in Dehnen & Binney (1998) to determine the velocity dispersion for a sample of stars. But we also employ a moving window across the CMD bifurcation to better compare the sequences as they cool. The velocity distributions shown in Fig. 4.3 were found for WDs within 500 pc, whereas here we use WDs limited to either 100 pc or 200 pc, the result of which can be seen in Fig. 4.4. Here it can be clearly seen for the 200 pc sample that the red sequence has a higher velocity dispersion across all magnitudes. For the 100 pc sample, this is also visible but less so. We can however show that the two samples are drawn from the same underlying distribution. We determine the following Q-statistic for the two dispersion of the samples at various points:

$$Q = \frac{\sigma_{d_1} - \sigma_{d_2}}{\sqrt{\Delta\sigma_{d_1}^2 + \Delta\sigma_{d_2}^2}}, \tag{4.4}$$

where d_1 is the 100 pc sample and d_2 are stars between 100-200 pc. Both the red and blue Cumulative Distribution Functions (CDF) match well with a Gaussian distribution, and using a Kolmogorov-Smirnov test gives P-values between them and a true Gaussian which all lie above 0.8. Therefore, the difference between the two figures is consistent with simple statistical noise.

This shows that the two sequences between magnitudes 12 and 14 are *kinematically separate and distinct populations*. In regards to the discussion in section 4.2, this would agree neatly with the two sequences being comprised of WDs different masses where the heavier WDs are formed recently, giving them less time to be heated dynamically and thus forming the blue sample we have seen here. It cannot be ruled out the atmospheric composition is partly responsible for the bifurcation in the CMD but it cannot be the sole explanation. In our 100 pc samples, we cross-matched with the Montreal White Dwarf Database (Dufour et al., 2017) to find that 85% of the cross-matched red sample and 39% of the blue are DAs, so there are undoubtedly non-DAs in the second sequence. If they truly correspond to 60%, they still do not significantly alter the kinematics of the sample as a whole. It can be argued that the crystallization of massive WDs would provide massive WDs which are still visible in our range due to cooling delays (e.g., Tremblay et al. 2019; Bergeron et al. 2019; Bauer et al. 2020). If this were the case, these massive WDs would have been around for long enough to have significant dynamical heating. If this process is contaminating the sample, the fact that we still see the kinematic split is arguably even more significant.

Further insight into the CMD bifurcation of the WD sequence will likely require a combination of both spectroscopic and kinematic studies. Here, we have demonstrated the possibilities of working with only proper motions when analysing the vast Gaia datasets.

Chapter 5

Paper III

5.1 Introduction

Following on from the previous paper, we wished to apply our implemented MPLE to other interesting subsamples of the *Gaia* data. We were also able to make use of the improved Gaia DR3.

The study of kinematic space can be divided into the study of the Galactic disc and the stellar halo. This division guides our choice of samples and is understandable since the two regions are affected by different dynamical processes. The disc we have already described in section 4.1. The stellar halo, on the other hand, is where the evidence of past mergers between the Galaxy and its neighbours will be found (Helmi, 2020). These mergers can, for example, contribute to the velocity distribution and cause enhanced star formation (Ruiz-Lara et al., 2020). This is what inspires our chosen samples of data: the Solar neighbourhood disc sample and the local stellar halo.

Since our method requires only measured astrometry for the stars and not radial velocities, we can then utilise larger sets of data for these populations. Limiting the Solar neighbourhood to $\varpi > 5$ mas (or 200 pc) we can use as many as 1 171 846 stars, after having applied all of our quality cuts. This is comparable to current results using the Gaia RVS like Lucchini et al. (2022) which has 982 879 stars in the Solar neighbourhood. However, they do not apply any quality filters on photometry or astrometry, apart from a criteria of 20% parallax uncertainty ($\varpi/\sigma_\varpi > 5$). We restrict our results to only 10% uncertainty and if we were to use 20%, we would have 3 592 434 sources before applying our quality filters, which highlights the benefits of our method.

For the stellar halo, a recent similar sample is Dodd et al. (2022) which limits their halo to 2.5 kpc with <20% relative parallax uncertainty as well as imposing a velocity cut whereby the motions of the star with respect to the Local Standard of Rest (LSR) must be greater than 210 km/s. Since the circular speed at the position of the sun is $\sim$233 km s^{-1} (McMillan, 2017), this cut removes the vast majority of the disc stars. Our cuts on distance and velocity are slightly more generous with a distance limit of 3 kpc and velocity limit of at least 200 km s^{-1}, albeit on transverse velocity rather than full space velocity. Their sample contains 72 274 stars, whereas ours contains 456 273.

We use these two samples to estimate their velocity distributions. For the Solar neighbourhood, this is done in the same manner as for the WDs in the previous paper. The stellar halo distribution is inferred in spherical coordinates rather than Cartesian since it is more spherically symmetric around the Galaxy. We also divide the stellar halo into *in situ* and *accreted* components (e.g., Naidu et al. 2020). The velocity distributions are studied closely to determine if known structure is detected and what new structure we are able to identify. Some novel structures do appear in our analysis, specifically in the accreted halo where we find two new features that we call *MMH-1* and *MMH-2*.

5.2 Gaia's view of the local Galaxy

There has been plenty of work done to try and characterise the velocity substructure that exists in the disc and stellar halo. We briefly discussed the Solar neighbourhood in chapter 4 and showed several moving groups from Antoja et al. (2012) in Fig. 4.3. Above Lucchini et al. (2022) was mentioned which is one of the more recent works that investigates the disc structure. The current picture of the local disc velocity distribution is one with multiple arch-like structures, of which many fractured individual substructures can be identified (see e.g., Table 1 from Lucchini et al. 2022).

For the stellar halo, things look slightly different. This is currently a very active field, but some smaller discoveries were made already 20 years ago using Hipparcos to identify the Helmi streams (Helmi et al., 1999). It is, perhaps, not surprising that *Gaia* has had a significant impact on this field as well. When DR2 was released, an important finding for the stellar halo came soon thereafter. By selecting stars with $v_{\mathrm{T}} > 200$ km s^{-1} Gaia Collaboration et al. (2018b) showed that in the CMD appears two separate main sequences, a finding that we recreate and show in Fig. 5.1. Rather than a main sequence with binaries adding a brighter,

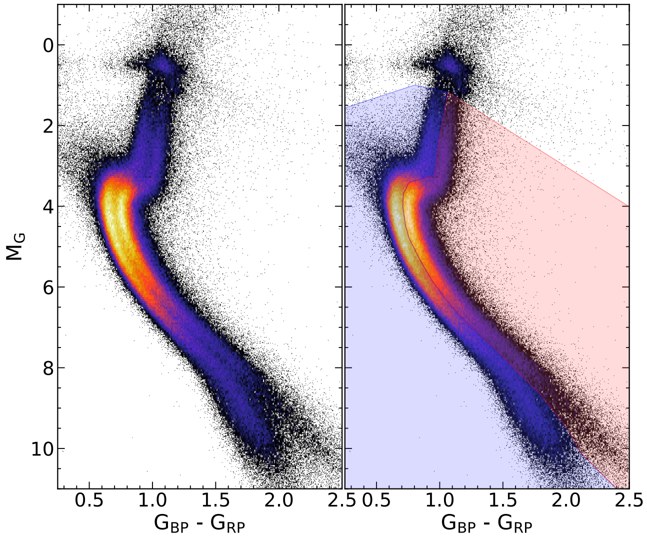

Figure 5.1: Colour-magnitude diagram of our filtered halo sample. The colour shows the number density. The right panel shows selected regions for the left and right sequences overlaid with shaded areas.

redder sequence the new sequence appears on the left, consistent with isochrones of a lower metallicity. Based on its kinematics, chemistry, and age the left sequence was found to be connected to an accretion event from a single object (Belokurov et al., 2018; Helmi et al., 2018) which is called *Gaia-Sausage-Enceladus* or *GSE*. This led to a successful hunt for other accreted populations in the stellar halo which matched very well to the notion of a Galaxy formed through hierarchical growth, suggested by the ΛCDM model mentioned in Section 1.1.3. At the time of writing, some of the larger discovered structures include *Sequoia* (Myeong et al., 2019), *Antaeus* (Oria et al., 2022), *Thamnos* 1 and 2 (Koppelman et al., 2019), and *Typhon* (Tenachi et al., 2022), to name a few. We show the expected positions of these features as well as some smaller ones in Fig. 5.2. This puts into perspective how structured the Galactic stellar halo has been revealed to be with the use of *Gaia* data.

Since we have access to the most expansive catalogue of sources from *Gaia*, we aim to expand the view of substructure in the local parts of the Galaxy's disc and stellar halo.

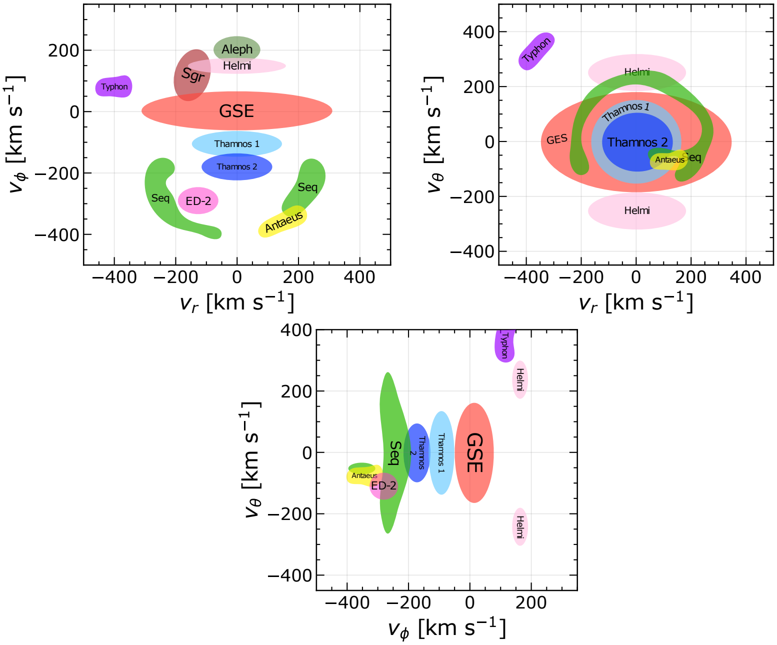

Figure 5.2: Estimated typical positions of known velocity structures in the stellar halo. Figures show the velocity spaces of (v_r, v_ϕ) (top left), (v_r, v_θ) (top right), and (v_ϕ, v_θ) (bottom). Here v_r points outwards from the Galactic centre, v_ϕ increases in the direction of Galactic rotation, and v_θ increases from south to north Galactic poles.

5.3 Structures: The old and the new

When we investigated the velocity distribution of the Solar neighbourhood we found that the distribution is heavily dominated by the typical major moving groups: *Sirius*, *Coma Berencies*, *Hyades*, *Pleiades*, and *Hercules*. The distributions also contains weaker traces of *Dehnen98* and *Wolf630*. A curious feature that stood out is a strong overdensity near *Pleiades*, close to $(U, V) = (-10, -15)$ km s^{-1} which is not found in literature. This may be a new moving group that we can discern due to our 1 km s^{-1} resolution. However, since the distribution is so heavily dominated by the major features, a better way of unravelling the low-level structure that these representations of the velocity distribution may have missed is to renormalize the plots. This implies that rather than showing the full 2D probability density of U and V, we show the *conditional* probabilities of V or U

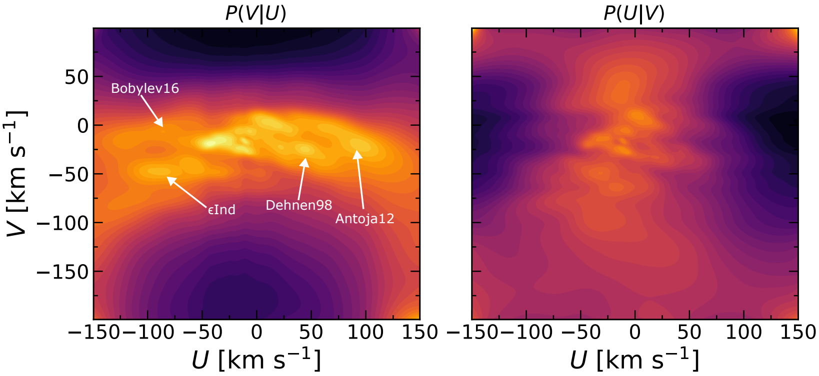

Figure 5.3: The conditional probability of one velocity component in (U, V) against the other. Left shows $P(V|U)$ and right shows $P(U|V)$ which reveals rich substructure beyond the central dominating groups. The color shows the density scaled as $P(v)^{0.25}$.

for each U or V, respectively. That is, the colour represents the probability of the star having a specific V given that it has a certain U velocity (or vice versa). The result is probability maps that can reveal structure that is otherwise blotted out by the major groups and we show this in Fig. 5.3. Here can be seen much richer structure like ϵ*Ind* (e.g., Antoja et al. 2012; Kushniruk et al. 2017; Bobylev & Bajkova 2016) at $(U, V) = (-100, -50)$ km s^{-1}, *Dehnen98* (Antoja et al., 2012) at $(U, V) = (50, -30)$ km s^{-1}, a group from Bobylev & Bajkova (2016) at $(U, V) = (-100, -10)$ km s^{-1}, and likely *Antoja12* from e.g. Kushniruk et al. (2017) at $(U, V) = (100, -30)$ km s^{-1}. The conditional probability maps are clearly a useful tool for the outer regions.

The velocity distributions of the two halo samples were determined and as expected, the right sequence shows very little accreted structure and as such we only focus on the left sequence. The velocity distributions are shown in Fig. 5.4 and are overlaid with the expected positions of stellar halo substructure from Fig. 5.2. These distributions show clearly a lot of the known velocity substructures such as *GSE*, *Sequoia*, and the *Helmi* streams. Particularly the *GSE* in (v_r, v_ϕ) shows a lot of structure with significant peaks marked as G1-G5. The groups at largest v_r, 1 and 5, are placed where the *GSE* is typically associated (e.g., Feuillet et al. 2021). G2 and G4 lie near the region which is removed by our cut of $v_\mathrm{T} < 200$ km s^{-1} and are therefore probably contaminants from the disc population. Finally G3 matches with Cluster 3 of Lövdal et al. (2022) which is also called *L-RL3* in Dodd

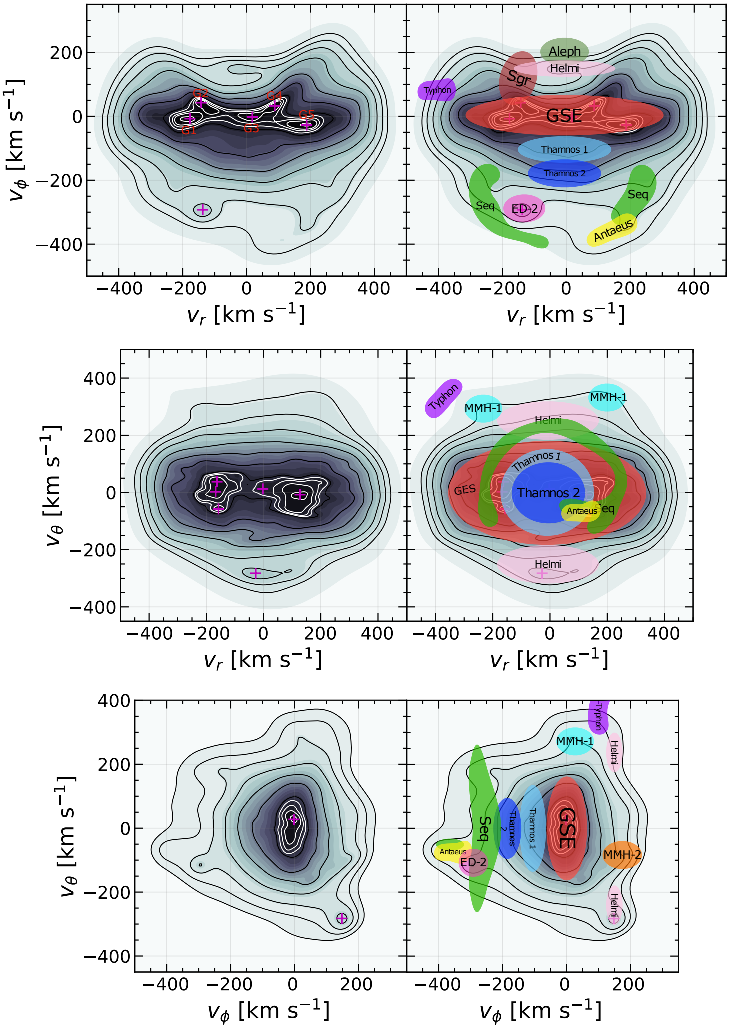

Figure 5.4: Velocity distributions of our left halo sample in (v_r, v_ϕ) (top row), (v_r, v_θ) (middle row), and $(v_\phi, v_\theta$ (bottom row). The right column shows the same distributions overlaid with the positions of expected substructures from literature, in a similar style to what is done in Naidu et al. (2020) and Mardini et al. (2022). Significant peaks are marked with purple crosses and in the top left figure five significant groups belonging to the *GSE* are marked as G1-G5.

et al. (2022). The distributions do show some of the smaller features as well and particularly the low v_θ-component of the *Helmi* stream is very pronounced here.

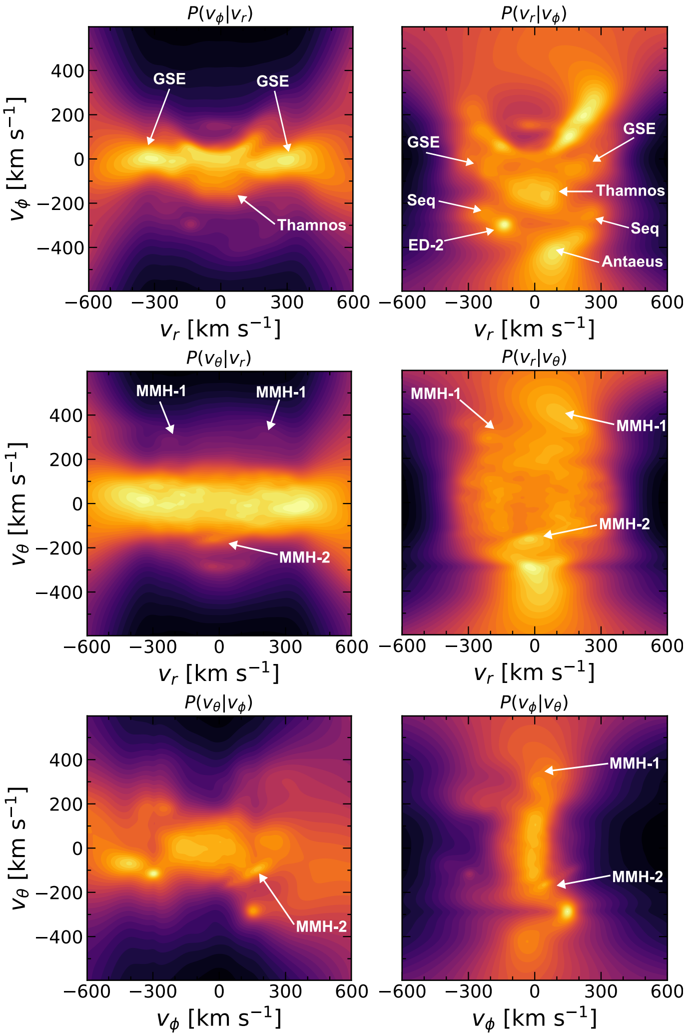

Figure 5.5: Conditional probability distributions of the velocities from Fig. 5.4 with the left column showing the conditional probability distribution of the y-axis velocity on the x-axis velocity. The right column shows the inverted conditional probabilities. Density is scaled as $P(v)^{0.25}$. The arrows show features discussed in Section 5.3. This map is used to unveil further information in the phase-space structure and as such the other features of Fig. 5.4 are not labelled here.

These figures give a good impression of what the accreted stellar halo looks like at ‘face value’.

Beyond these larger structures, there are three additional ones that we are able to identify. The first is *ED-2* from Dodd et al. (2022) at roughly $(v_r, v_\phi, v_\theta) = (-150, -300, -100)$ km s^{-1}. In Dodd et al. (2022) they note that it occupies about 0.05% of their sample with 33 proposed members. This region of velocity space makes up around 0.075% in our sample, suggesting that the group is slightly larger than previously believed. We are also able to make out two new velocity features which we call *MMH-1* and *MMH-2* which have no prior associations in literature. The first, *MMH-1*, lies at about $(v_r, v_\phi, v_\theta) = (\pm 225, 25, 325)$ km s^{-1} and is visible in the spaces of (v_r, v_θ) and (v_ϕ, v_θ). It is placed in the dense regions in (v_r, v_ϕ) and is therefore difficult to spot there. The second is *MMH-2* which is around $(v_\phi, v_\theta) \approx (150, -100)$ km s^{-1} and is a challenge to trace into v_r. However, its v_r component became clear when we again looked to the conditional probability of the velocities, seen in Fig. 5.5. Here, the sloped feature centred around $(v_r, v_\theta) = (0, -150)$ km s^{-1} stands out in both $P(v_r|v_\theta)$ and $P(v_\theta|v_r)$, and is the representation of *MMH-2* in this space. This shows also that the full extent of *MMH-2* is obscured in Fig. 5.4 and that its actual velocities are instead centred on $(v_r, v_\phi, v_\theta) = (0, 150, -125)$ km s^{-1}. These maps also reveal some parts of *Thamnos* up to $(v_r, v_\phi) = (0, -200)$ km s^{-1} which could previously not be seen. The extended nature of *MMH-1* at $v_\theta = 300$ km s^{-1} is uncovered as well, stretching to even larger values of v_θ in both $P(v_r|v_\theta)$ and $P(v_\phi|v_\theta)$ and has what appears to be a symmetrical component at large negative v_θ, which if real would likely imply that this feature has considerable vertical action. This view also shows the strength of *MMH-1* as it appears in both $P(v_\theta|v_\phi)$ and $P(v_\phi|v_\theta)$.

The distributions and the insight into the Galaxy that we gain from them clearly advocate for the benefits of working with pure proper-motion limited catalogues. Until such a time that comparable 6D catalogues are available, these types of methods provide the largest possible data sets for kinematic studies.

References

Andersson E. P., Agertz O., Renaud F., 2020, MNRAS, 494, 3328

Anguiano B., Rebassa-Mansergas A., García-Berro E., Torres S., Freeman K. C., Zwitter T., 2017, MNRAS, 469, 2102

Antoja T., Figueras F., Torra J., Valenzuela O., Pichardo B., 2010, in , Vol. 4, Lecture Notes and Essays in Astrophysics. pp 13–31

Antoja T., et al., 2012, MNRAS, 426, L1

Antoja T., de Bruijne J., Figueras F., Mor R., Prusti T., Roca-Fàbrega S., 2017, A&A, 602, L13

Aumer M., Binney J., Schönrich R., 2016, MNRAS, 462, 1697

Bauer E. B., Schwab J., Bildsten L., Cheng S., 2020, ApJ, 902, 93

Belokurov V., Erkal D., Evans N. W., Koposov S. E., Deason A. J., 2018, MNRAS, 478, 611

Bensby T., Feltzing S., Oey M. S., 2014, A&A, 562, A71

Bergeron P., Dufour P., Fontaine G., Coutu S., Blouin S., Genest-Beaulieu C., Bédard A., Rolland B., 2019, ApJ, 876, 67

Binney J., 2007, in DE JONG R. S., ed., ISLAND UNIVERSES. Springer Netherlands, Dordrecht, pp 67–76

Binney J., Tremaine S., 2008, Galactic Dynamics: Second Edition

Bland-Hawthorn J., Gerhard O., 2016, ARA&A, 54, 529

Bobylev V. V., Bajkova A. T., 2016, Astronomy Letters, 42, 90

Bovy J., Leung H. W., Hunt J. A. S., Mackereth J. T., García-Hernández D. A., Roman-Lopes A., 2019, MNRAS, 490, 4740

Burbidge E. M., Burbidge G. R., Fowler W. A., Hoyle F., 1957, Reviews of Modern Physics, 29, 547

Clarke J. P., Gerhard O., 2022, MNRAS, 512, 2171

Clarkson W., et al., 2008, ApJ, 684, 1110

D'Onghia E., 2015, ApJL, 808, L8

Da Costa G. S., et al., 2019, MNRAS, 489, 5900

Daniel K. J., Wyse R. F. G., 2018, MNRAS, 476, 1561

Dehnen W., 1998, AJ, 115, 2384

Dehnen W., Binney J. J., 1998, MNRAS, 298, 387

Dehnen W., McLaughlin D. E., 2005, MNRAS, 363, 1057

Dodd E., Callingham T. M., Helmi A., Matsuno T., Ruiz-Lara T., Balbinot E., Lovdal S., 2022, arXiv e-prints, p. arXiv:2206.11248

Dufour P., Blouin S., Coutu S., Fortin-Archambault M., Thibeault C., Bergeron P., Fontaine G., 2017, in Tremblay P. E., Gaensicke B., Marsh T., eds, Astronomical Society of the Pacific Conference Series Vol. 509, 20th European White Dwarf Workshop. p. 3 (`arXiv:1610.00986`)

Edvardsson B., Andersen J., Gustafsson B., Lambert D. L., Nissen P. E., Tomkin J., 1993, A&A, 275, 101

Eisenhauer F., et al., 2011, The Messenger, 143, 16

El-Badry K., Rix H.-W., Weisz D. R., 2018, ApJL, 860, L17

Fall S. M., Efstathiou G., 1980, MNRAS, 193, 189

Feuillet D. K., Sahlholdt C. L., Feltzing S., Casagrande L., 2021, MNRAS, 508, 1489

Flamsteed J., 1725, Historia Coelestis Britannicae

Fontaine G., Brassard P., Bergeron P., 2001, PASP, 113, 409

Frankel N., Rix H.-W., Ting Y.-S., Ness M., Hogg D. W., 2018, ApJ, 865, 96

Gaia Collaboration et al., 2016a, A&A, 595, A1

Gaia Collaboration et al., 2016b, A&A, 595, A2

Gaia Collaboration et al., 2018a, A&A, 616, A1

Gaia Collaboration et al., 2018b, A&A, 616, A10

Gaia Collaboration et al., 2018c, A&A, 616, A11

Gaia Collaboration et al., 2021, A&A, 649, A1

Gaia Collaboration et al., 2022a, A&A accepted, arXiv:2206.06207

Gaia Collaboration et al., 2022b, A&A accepted, arXiv:2208.00211

Gentile Fusillo N. P., et al., 2019, MNRAS, 482, 4570

Halle A., Di Matteo P., Haywood M., Combes F., 2015, A&A, 578, A58

Hayden M. R., et al., 2015, ApJ, 808, 132

Helmi A., 2020, ARA&A, 58, 205

Helmi A., White S. D. M., de Zeeuw P. T., Zhao H., 1999, Nature, 402, 53

Helmi A., Babusiaux C., Koppelman H. H., Massari D., Veljanoski J., Brown A. G. A., 2018, Nature, 563, 85

Hernquist L., 1990, ApJ, 356, 359

Hobbs D., et al., 2021, Experimental Astronomy, 51, 783

Høg E., et al., 2000, A&A, 355, L27

Horta D., et al., 2022, arXiv e-prints, p. arXiv:2204.04233

Katz D., Gómez A., Haywood M., Snaith O., Di Matteo P., 2021, A&A, 655, A111

Kilic M., Hambly N. C., Bergeron P., Genest-Beaulieu C., Rowell N., 2018, MNRAS, 479, L113

Kilic M., Bergeron P., Kosakowski A., Brown W. R., Agüeros M. A., Blouin S., 2020, ApJ, 898, 84

Kippenhahn R., Weigert A., Weiss A., 2012, Stellar Structure and Evolution. Springer Science & Business Media

Kipper R., Tenjes P., Tuvikene T., Ganeshaiah Veena P., Tempel E., 2020, MNRAS, 494, 3358

Koppelman H. H., Helmi A., 2021, A&A, 649, A136

Koppelman H. H., Helmi A., Massari D., Price-Whelan A. M., Starkenburg T. K., 2019, A&A, 631, L9

Kormendy J., 2013, in Falcón-Barroso J., Knapen J. H., eds, , Secular Evolution of Galaxies. p. 1

Kushniruk I., Schirmer T., Bensby T., 2017, A&A, 608, A73

Leeming D. A., 1998, Mythology: The Voyage of the Hero. Oxford University Press

Lövdal S., Ruiz-Lara T., Koppelman H. H., Matsuno T., Dodd E., Helmi A., 2022, arXiv e-prints, p. arXiv:2201.02404

Lucchini S., Pellett E., D'Onghia E., Aguerri J. A. L., 2022, arXiv e-prints, p. arXiv:2206.10633

Mackereth J. T., Bovy J., 2020, MNRAS, 492, 3631

Magli G., 2020, Archaeoastronomy: introduction to the science of stars and stones. Springer Nature

Mardini M. K., Frebel A., Chiti A., Meiron Y., Brauer K. V., Ou X., 2022, ApJ, 936, 78

Martig M., Minchev I., Flynn C., 2014, MNRAS, 443, 2452

Martig M., Minchev I., Ness M., Fouesneau M., Rix H.-W., 2016, ApJ, 831, 139

McMillan P. J., 2017, MNRAS, 465, 76

McMillan P. J., Dehnen W., 2007, MNRAS, 378, 541

McMillan P. J., et al., 2022, MNRAS,

Michalik D., Lindegren L., Hobbs D., 2015, A&A, 574, A115

Minchev I., Famaey B., Quillen A. C., Di Matteo P., Combes F., Vlajić M., Erwin P., Bland-Hawthorn J., 2012, A&A, 548, A126

Monari G., et al., 2018, Research Notes of the American Astronomical Society, 2, 32

Myeong G. C., Vasiliev E., Iorio G., Evans N. W., Belokurov V., 2019, MNRAS, 488, 1235

Naidu R. P., Conroy C., Bonaca A., Johnson B. D., Ting Y.-S., Caldwell N., Zaritsky D., Cargile P. A., 2020, ApJ, 901, 48

Ness M., et al., 2013a, MNRAS, 430, 836

Ness M., et al., 2013b, MNRAS, 432, 2092

Ness M., Debattista V. P., Bensby T., Feltzing S., Roškar R., Cole D. R., Johnson J. A., Freeman K., 2014, ApJL, 787, L19

Oria P.-A., Tenachi W., Ibata R., Famaey B., Yuan Z., Arentsen A., Martin N., Viswanathan A., 2022, ApJL, 936, L3

Perryman M., 2009, Astronomical Applications of Astrometry: Ten Years of Exploitation of the Hipparcos Satellite Data. Cambridge University Press

Perryman M., 2012, European Physical Journal H, 37, 745

Perryman M. A. C., et al., 1997, A&A, 323, L49

Planck Collaboration et al., 2020, A&A, 641, A6

Posti L., Helmi A., 2019, A&A, 621, A56

Raddi R., et al., 2022, A&A, 658, A22

Reid M. J., et al., 2019, ApJ, 885, 131

Roškar R., Debattista V. P., Quinn T. R., Wadsley J., 2012, MNRAS, 426, 2089

Rowell N., Hambly N. C., 2011, MNRAS, 417, 93

Ruiz-Lara T., Gallart C., Bernard E. J., Cassisi S., 2020, Nature Astronomy, 4, 965

Sanders J. L., Smith L., Evans N. W., 2019, MNRAS, 488, 4552

Schönrich R., Binney J., 2009, MNRAS, 396, 203

Schönrich R., McMillan P. J., 2017, MNRAS, 467, 1154

Sellwood J. A., Binney J. J., 2002, MNRAS, 336, 785

Shen J., Rich R. M., Kormendy J., Howard C. D., De Propris R., Kunder A., 2010, ApJL, 720, L72

Sion E. M., Liebert J., 1977, ApJ, 213, 468

Sion E. M., Fritz M. L., McMullin J. P., Lallo M. D., 1988, AJ, 96, 251

Solway M., Sellwood J. A., Schönrich R., 2012, MNRAS, 422, 1363

Springel V., et al., 2005, Nature, 435, 629

Tenachi W., Oria P.-A., Ibata R., Famaey B., Yuan Z., Arentsen A., Martin N., Viswanathan A., 2022, ApJL, 935, L22

Teuben P., 1995, in Shaw R. A., Payne H. E., Hayes J. J. E., eds, Astronomical Society of the Pacific Conference Series Vol. 77, Astronomical Data Analysis Software and Systems IV. p. 398

Torres S., Cantero C., Camisassa M. E., Antoja T., Rebassa-Mansergas A., Althaus L. G., Thelemaque T., Cánovas H., 2019, A&A, 629, L6

Toyouchi D., Chiba M., 2016, ApJ, 833, 239

Tremblay P.-E., et al., 2019, Nature, 565, 202

Trick W. H., 2022, MNRAS, 509, 844

Trick W. H., Coronado J., Rix H.-W., 2019, MNRAS, 484, 3291

Trick W. H., Fragkoudi F., Hunt J. A. S., Mackereth J. T., White S. D. M., 2021, MNRAS, 500, 2645

Vera-Ciro C., D'Onghia E., Navarro J., Abadi M., 2014, ApJ, 794, 173

Vera-Ciro C., D'Onghia E., Navarro J. F., 2016, ApJ, 833, 42

Wegg C., Gerhard O., 2013, MNRAS, 435, 1874

Wegg C., Gerhard O., Portail M., 2015, MNRAS, 450, 4050

White S. D. M., Rees M. J., 1978, MNRAS, 183, 341

Wright T., 1750, An original theory or new hypothesis of the universe: founded upon the laws of nature, and solving by mathematical principles the general phnomena of the visible creation; and particularly the via lactea

Xu Y., et al., 2013, ApJ, 769, 15

Zari E., Frankel N., Rix H. W., 2022, arXiv e-prints, p. arXiv:2206.02616

de Jong T., 2007, Wiener Zeitschrift für die Kunde des Morgenlandes, 97, 107

de Lalande J. J. L. F., 1801, Histoire céleste française. Vol. 1

van Altena W. F., Lee J. T., Hoffleit E. D., 1995, The general catalogue of trigonometric [stellar] parallaxes

Scientific publications

Paper I

Paper I: Radial migration and vertical action in N-body simulations

Mikkola, D.; McMillan, P. J.; Hobbs, D. (2020)
Monthly Notices of the Royal Astronomical Society, Volume 495, Issue 3, pp. 3295-3306

My contribution:

Paul McMillan (PM) had the original idea for the paper after reading about the role of migration for large vertical excursions in Solway et al. (2012) and Vera-Ciro et al. (2014, 2016). Daniel Mikkola (DM) set up and ran the numerical simulations and wrote all of the analysis tools that were used. David Hobbs (DH) and PM advised on choice of simulation code and on what analysis to perform. Outputs of simulations were analyzed by DM with guidance by his supervisors DH and PM and discussed by DM, PM, and DH. PM provided literature resources for the writing and DM wrote and submitted the manuscript. Several rounds of revisions, feedback, and discussions between the authors as well as with an anonymous referee led to the final product which was accepted for publication.

Monthly Notices
of the
ROYAL ASTRONOMICAL SOCIETY

MNRAS **495,** 3295–3306 (2020)
Advance Access publication 2020 May 16

doi:10.1093/mnras/staa1223

Radial migration and vertical action in *N*-body simulations

Daniel Mikkola,* Paul J. McMillan and David Hobbs
Department of Astronomy and Theoretical Physics, Lund Observatory, Lund University, Box 43, SE-22100 Lund, Sweden

Accepted 2020 April 27. Received 2020 March 20; in original form 2019 October 28

ABSTRACT

We study the radial migration of stars as a function of orbital action as well as the structural properties of a large suite of *N*-body simulations of isolated disc galaxies. Our goal is to establish a relationship between the radial migration efficiency of stars and their vertical action. We aim to describe how that relationship depends on the relative gravitational dominance between the disc and the dark matter halo. By changing the mass ratio of our disc and dark matter halo, we find a relationship between disc dominance, number, and strength of spiral arms, and the ensuing radial migration as a function of the vertical action. We conclude that the importance of migration at large vertical action depends on the strength of the spiral arms and therefore the dominance of the disc. Populations with more radial action undergo less radial migration, independently of disc dominance. Our results are important for the future of analytical modelling of radial migration in galaxies and further the understanding of radial migration that is a key component of the restructuring of galaxies, including the Milky Way.

Key words: methods: numerical – Galaxy: disc – Galaxy: formation – Galaxy: kinematics and dynamics – galaxies: evolution – galaxies: spiral.

1 INTRODUCTION

During the evolution of a galaxy there are a number of external and internal factors that play a part in shaping its chemodynamical structure. One of these factors is called radial migration and is capable of displacing stars over large radial distances. Because of this radial migration plays an important part in the restructuring of a galaxy over time. In this paper, we will study radial migration over large time-scales to determine which stars migrate and in what way this is affected by the strength and number of the spiral arms present.

A galaxy can suffer mergers with other galaxies and has significant evolution from within, through giant molecular clouds (GMCs) and secular features like bars and spiral arms. Both in the context of an isolated galaxy and when there is a dynamic galactic environment, the local regions of a galaxy do not evolve independently. This has been clearly seen in studies of the chemical properties of the Milky Way, particularly in the age–metallicity relationship (Edvardsson et al. 1993; Bensby, Feltzing & Oey 2014; Bergemann et al. 2014). Studies of this nature show that there is a significant scatter in abundances at almost all ages. Such a scatter would not exist in an isolated setting and instead supports the existence of a restructuring process.

An important process that restructures galaxies is radial migration. Sellwood & Binney (2002) showed that significant angular momentum changes could occur when the pattern speeds of stars and spirals match at corotation, in addition to the angular momentum changes at the Lindblad resonances previously known (Lynden-Bell & Kalnajs 1972). This process is able to move stars by kiloparsecs and does not leave dynamical traces.

The importance of radial migration has been shown not only by its role in broadening abundance distributions across the Galaxy, but has been suggested as an explanation for the bimodality of stars in the [α/Fe]–[Fe/H] plane (Schönrich & Binney 2009; Toyouchi & Chiba 2016) and as cause for mono-age population flaring in the outer disc (Minchev et al. 2012, 2015). The effects of radial migration has been studied extensively by simulations (Roškar et al. 2008; Halle et al. 2015; Aumer, Binney & Schönrich 2016a, b; Aumer & Binney 2017; Aumer, Binney & Schönrich 2017), analytical models (Sellwood & Binney 2002; Schönrich & Binney 2009; Schönrich & McMillan 2017), and real data (Frankel et al. 2018; Minchev et al. 2018) but still requires further understanding of which stars are more likely to undergo migration.

Radial migration is driven by secular features such as spiral arms and bars and is therefore going to affect stars differently depending on their positions and velocities within the disc of a galaxy. Studies that utilize analytical models like Schönrich & Binney (2009) and Schönrich & McMillan (2017) therefore rely upon a sound understanding of which stars are migrated and to which extent. The extent of radial migration as a function of position or velocity about the mid-plane has been studied previously by, e.g. Solway, Sellwood & Schönrich (2012), Vera-Ciro et al. (2014), Vera-Ciro, D'Onghia & Navarro (2016) and in Daniel & Wyse (2018), the link between radial migration and dynamical temperature was investigated.

In this paper, we perform a large suite of *N*-body galaxy simulations to probe radial migration in terms of kinematics and its effects on the structure of galactic discs. We look at the migration of stars as a function of their vertical and radial actions, J_z and J_r, which quantifies the oscillations about the mid-plane of the disc and the average radius along an orbit, respectively. The structure of this paper is as follows; in Section 2 we outline the two processes commonly referred to as radial migration, in Section 3 we go through the details

---

* E-mail: mikkola@astro.lu.se

of the simulations we have performed and a subsequent Fourier analysis of them, in Section 4 we present our simulation results in terms of structural properties, actions, and action conservation before comparing them to those of Solway et al. (2012) and Vera-Ciro et al. (2014, 2016) who studied closely related topics, and in Section 5 we give our conclusions.

2 RADIAL MIGRATION

We will consider the two processes most commonly referred to as radial migration in disc galaxies namely *blurring* (Schönrich & Binney 2009) and *churning* (Sellwood & Binney 2002). Both are processes related to the orbits of stars and are significantly different. In this section, we approximate for simplicity's sake that a disc galaxy is a flat disc and use angular momentum to refer to the vector perpendicular to this disc, $L_z = Rv_\phi$, where R and v_ϕ are the radius and azimuthal velocity of a particle, respectively.

Blurring is the change in amplitude of radial oscillations around an average radius for an orbit, called the guiding radius, R_g. A star will be born on a nearly circular orbit and very likely scattered at some point in its life from a GMC or similar, placing it on to a slightly more or less radially extended orbit. The guiding radius and therefore angular momentum, since L_z is directly related to R_g, does not change through this process, and it is the change in amplitude of the oscillations between closest and furthest galactic radius that define blurring.

The second source of radial migration is *churning*, first described by Sellwood & Binney (2002), which is caused by non-axisymmetric features such as bars and spiral arms exerting a torque on a star. In contrast to blurring, churning can change the angular momentum of an orbit without changing its eccentricity. Sellwood & Binney (2002) showed that conservation of the Jacobi integral, $E_J = E - \Omega_\mathrm{p} L_z$, in the presence of a steady non-axisymmetric perturbation with pattern speed Ω_p implies the relationship

$$\Delta J_R = \frac{\Omega_\mathrm{p} - \Omega}{\omega_R} \Delta L_z. \tag{1}$$

Here, ΔJ_R is a measure of the extent of radial oscillations. ΔL_z is the change in angular momentum, Ω_p is the pattern speed of the spiral/bar, Ω is the angular speed of a star, and ω_R is the frequency of radial oscillations. A change in ΔJ_R will follow from radial migration where the angular momentum is changed, $\Delta L_z \neq 0$, but is made less pronounced if such a migration occurs near corotation where the angular velocity of the star is the same as the spiral arm/bar, $\Omega = \Omega_\mathrm{p}$, in which case there is close to zero change in radial action. This feature of churning is perhaps also the most frustrating, as it means stars are able to radially migrate with no dynamical trace of the procedure, which removes the possibility of dynamically discerning a migrated star in the Solar neighbourhood from a local one. The direction of the migration is determined by whether the star is inside or outside the corotation resonance as the sign of the exerted torque will change. A star inside corotation moves outwards and vice versa. A more rigorous demonstration of churning was given in Sellwood & Binney (2002) with spiral arms churning stars and gas without changing the overall angular momentum distribution or increasing the random motions significantly.

We mentioned in the previous section the importance of understanding which stars migrate and this is not fully understood. It is important to further increase our understanding of which gradients in radial migration exist if we are to use analytical models of it. In Daniel & Wyse (2018), they use a series of analytical disc galaxy models and study the fraction of stars trapped at corotation depending on the velocity dispersion. They find that this fraction declines with increasing radial velocity dispersion. Their analysis is 2D and therefore does not make any statements about the vertical distribution of migrators.

Two articles that study the vertical gradient of radial migration are Solway et al. (2012) and Vera-Ciro et al. (2014). Solway et al. (2012) uses an N-body disc in a static potential halo. They include both a thick and thin disc and conclude that the root mean square angular momentum changes are gradually reduced. That radial migration is reduced by vertical motion is also supported by Vera-Ciro et al. (2014) and subsequently by Vera-Ciro et al. (2016) who use three different simulations of live discs embedded in static halo potentials. These systems vary in the dominance of the disc and this creates different spiral morphologies (e.g. D'Onghia 2015). The result in all three simulations is what is called a 'provenance bias', i.e. that migration primarily concerns stars with small vertical excursions regardless of spiral pattern. This is at first glance not surprising since stars with small vertical excursions should spend more time closer to the mid-plane where the spirals are strongest. However, sufficiently strong spirals, which could arise in very disc dominated systems, could migrate stars of larger vertical excursions as well. How much radial migration is a function of its vertical excursions depending on the spiral morphology and disc dominance has not previously been established. To investigate this, we use a large suite of simulations that span a broad range in disc dominance. We use N-body discs as well as haloes and bulges and investigate the effects on spiral strength and structure. To probe the effect of vertical excursions on radial migration, we calculate actions for our stars and compare the vertical action, J_z, to the amount of migration that occurs in different parts of our galaxies.

2.1 Action variables

Instead of characterizing the vertical and radial gradients of radial migration by position or velocities we use actions. Take for example the vertical action:

$$J_z = \frac{1}{2\pi} \oint_{\gamma_z} v_z \,\mathrm{d}z, \tag{2}$$

where the line integral is over a path, γ_z, of phase-space coordinates that the orbit can go through and which goes through a full vertical oscillation. This can be, for example, the heights and vertical velocities (z, v_z) that an orbit can have as it goes through a given radius R (the surface of section, e.g. Binney & Tremaine 2008, section 3.2.2). However, it is enormously difficult to calculate the actions using a surface of section directly. We use a more accurate and robust approach available in the software library AGAMA. This allows us to approximate the gravitation potential of our simulation as an axisymmetric expansion in spherical harmonics, and to calculate actions by applying the 'Stäckel fudge' from Binney (2012), which uses the approximation that any orbit in a realistic galactic potential can be closely approximated by one in a Stäckel potential.

This allows us to use vertical action instead of vertical position and velocity which has the advantage of not oscillating along an orbit and is a good measure of how vertically heated an orbit is. The same is true for J_r in the radial direction.

3 SIMULATIONS

In order to study radial migration, we generate a number of N-body galaxies that were numerically integrated using the tree code

Table 1. Parameters of the *N*-body disc. The mass of the disc, M_d, the number of particles, N_d, the scale length, R_d, the scale height, z_d, the normalization constant of σ_R, Toomre's Q, the number of bodies per orbit, and the softening length, ϵ.

M_d ($\mathrm{M}_\odot$)	N_d	R_d (kpc)	z_d (kpc)	R_σ (kpc)	Q	N_bpo	ϵ (kpc)
5×10^{10}	10^6	3	0.3	9	1.7	50	0.03

GYRFALCON (Dehnen 2000, 2002) which is available as part of the NEMO[1] (Teuben 1995) toolbox.

3.1 Initial conditions

To generate the initial conditions, three packages within NEMO were used: MKWD99DISC, MKHALO, and MKGALAXY (McMillan & Dehnen 2007), the first two for the disc and halo/bulge, respectively, and the latter combines the two for systems containing a disc, halo, and bulge.

3.2 The disc

The disc is generated using the procedure laid out in McMillan & Dehnen (2007). This method uses the distribution function described in Dehnen (1999) which has the advantage that it avoids using a Maxwellian approximation, and therefore starts close to equilibrium. The disc is generated iteratively in the potential of the halo and bulge, tending towards the specified profile. It is designed to be stable to axisymmetric perturbations, but not stable to the non-axisymmetric perturbations that are expected to arise.

The density profile is of the form

$$\rho_\mathrm{disc}(R, z) = \frac{1}{2z_\mathrm{d}} \Sigma_0 \exp\left(-\frac{R}{R_\mathrm{d}}\right) \mathrm{sech}^2\left(\frac{z}{z_\mathrm{d}}\right), \tag{3}$$

where the disc mass corresponds to $M_\mathrm{d} = 2\pi R_\mathrm{d}^2 \Sigma_0$ with Σ_0 being the scale density, R_d is the scale radius, and z_d is the scale height. The radial velocity dispersion profile is $\sigma_R \propto \exp(-\ R/R_\sigma)$ where the parameters R_σ and Q, the selected value for Toomre's Q (Toomre 1964), determine the constant of proportionality. The vertical velocity dispersion is $\sigma_z^2 = \pi G \Sigma(R) z_\mathrm{d}$. The number of bodies in a single orbit is set with N_bpo and the gravitational softening length is ϵ. The parameters used when generating the disc are listed in Table 1.

3.3 The halo and bulge

Both halo and bulge are generated within MKGALAXY and the spheroids are created with spherical density distribution:

$$\rho(r) = \frac{\rho_0}{x^{\gamma_i}(x^\eta + 1)^{\gamma_o - \gamma_i/\eta}} \mathrm{sech}\left(\frac{r}{r_t}\right), \tag{4}$$

with $x = r/r_\mathrm{s}$, r_s being scale radius, ρ_0 is the scale density, r_t is the truncation radius, γ_i and γ_o are the inner and outer exponents, and η is the transition strength between them. For the halo these parameters are selected to produce a Dehnen–McLaughlin dark matter halo (Dehnen & McLaughlin 2005) which can be seen in Table 2. Further explanation of the parameters can be found in McMillan & Dehnen (2007). The sech factor of the profile is a truncation. For the bulge, a Hernquist profile (Hernquist 1990) is used with parameters in Table 2. To constrain the parameters for the different components and achieve Milky Way-like initial conditions, values from McMillan (2017) are used. The mass of the halo is altered from this fiducial galaxy set-up, as discussed below.

Table 2. Parameters of the fiducial dark matter halo and bulge components. The mass of the component, M_tot, the scale radius, r_s, the truncation radius, r_t, the total number of particles in the component, N_tot, the inner exponent, γ_i, the outer exponent, γ_o, the transition exponent, η, and the softening length, ϵ.

M_tot ($\mathrm{M}_\odot$)	r_s (kpc)	r_t (kpc)	N_tot	γ_i	γ_o	η	ϵ (kpc)
			Halo				
3.4×10^{11}	17	30	2×10^6	7/9	31/9	4/9	0.02
			Bulge				
1.5×10^{10}	1	3	5×10^5	1	4	1	0.03

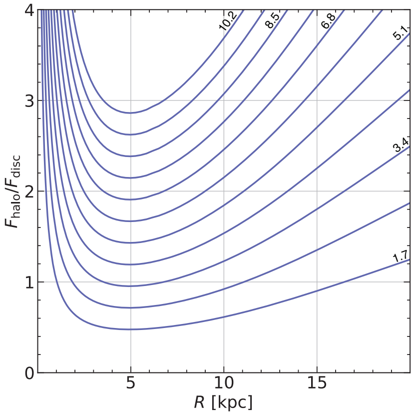

Figure 1. Ratio of the radial force from the dark matter halo and the disc at $z = 0$ against radius in simulations varying in dark matter halo total mass. The mass of the dark matter halo is written above its respective line for every other simulation in units of 10^{11} $\mathrm{M}_\odot$.

3.4 Simulation types

In order to create systems of varying number and strength of spiral modes, we generate galaxies where the dominance of the disc in relation to the halo is varied. This is achieved by simply increasing or decreasing the mass of the dark matter halo without changing any other parameters. The ratio of the radial force contributed by disc and dark matter halo at $z = 0$, as a function of radius can be seen in Fig. 1. Halo masses are picked in order to have a large spread in this ratio, including both disc dominant systems and halo dominant ones. Fig. 1 shows these ratios for the different halo mass simulations performed. The lightest halo starts at 1.7×10^{11} $\mathrm{M}_\odot$ and increases by 0.85×10^{11} $\mathrm{M}_\odot$ up until 1.02×10^{12} $\mathrm{M}_\odot$. In accordance with literature (e.g. D'Onghia 2015), the systems can be expected to form a larger number of spiral arms as the mass is increased. The strength of the spirals are expected to decrease as their number increases. For each system we generate 10 additional initial conditions varying only in random seed to give a sense of how the stochasticity of the initial

---

[1] https://github.com/teuben/nemo

conditions affects our results. In total this results in 121 simulations with 11 different seeds per halo mass used.

3.5 Spiral strength analysis

A key question is the link between how dominant the disc of a system is, the strength of corresponding bars/spirals, and the migration that ensues. To answer this the strength of the resonances that arise in the simulations must be measured. This is done using an extended Fourier analysis borrowing elements from Press et al. (1992) and described thoroughly in Roškar et al. (2012).

The disc is divided into annuli of equal widths such that the distribution of particles can be expanded into a Fourier series

$$\Sigma(R, \phi) = \sum_{m=0}^{\infty} c_m(R) \exp(-im\phi_m(R)), \tag{5}$$

with pattern multiplicity, m and ϕ_m the phase of the m-th mode at the given radius. The coefficient $c_m(R)$ is given by

$$c_m(R) = \frac{1}{M(R)} \sum_{j=1}^{N} m_j \exp(im\phi_j), \tag{6}$$

with the mass in the annuli $M(R)$, the mass of particle j as m_j, and the azimuth angle relative to the x-axis of the particle as ϕ_j. N is the total number of particles in the annuli. This method can be expected to identify bars at close radii and spirals at larger ones. Other azimuthal structures that can be identified through this method are ignored as any strong patterns appearing should be due to spirals or a bar.

At this point only patterns at a given time can be detected but performing the above analysis at different points in time creates a time series out of the coefficients, $c_m(R)$, from which one can obtain a discrete Fourier transform

$$C_{k,m}(R) = \sum_{j=0}^{S-1} c_j(R, m) w_j \exp(2\pi i jk/s), \tag{7}$$

where $c_j(R, M) = c_m(R)$ at a given time $t = t_0 + j\Delta t$. The number of snapshots identified is the sample size, S, $C_{k,\,m}$ are the Fourier coefficients for the discrete frequencies Ω_k, and w is a Gaussian window function,

$$w_j(x) = \exp(-(x - S/2)^2/(S/4)^2), \tag{8}$$

where x is the current snapshot.

The frequency sampling is determined by the sample size, S, and the time between samples, Δt such that

$$\Omega_k = 2\pi \frac{k}{S\Delta t} m, \qquad k = 0, 1, \ldots, \frac{S}{2}, \tag{9}$$

avoiding high-frequency spectral leakage. Care is taken not to overstep the Nyquist frequency since $\Omega_{\rm Ny} = \Omega_{S/2}$. The complete power spectrum is then

$$P(\Omega_k, R) = \frac{1}{W} \left[|C_k(R)|^2 + |C_{S-k}(R)|^2 \right], \quad k = 1, 2, \ldots, \frac{S}{2} - 1. \tag{10}$$

The power is normalized by $W = \sum_{j=0}^{S} w_j$. Using P, Ω_k, and R it is possible to construct a contour plot of the power spectrum, allowing identification of the pattern speed and extent of a certain mode.

In addition to this, the strength of a certain mode over time can be retrieved through the absolute value of the coefficients, $c_m(R)$, at a given time. This gives the amplitude of the wave,

$$A_m(R) = |c_m(R)|. \tag{11}$$

Dividing the maximum value of the amplitude by the amplitude of the zeroth mode for each snapshot gives the growth and evolution of a certain mode. However, this will only identify the strongest pattern for a given mode at any given time. That is, if for example the bar forms it will overshadow a previously identified $m = 2$ spiral. For this reason, the disc is separated into an inner, $R < 6$ kpc, and outer $R \geq 6$ kpc region. Generally, the bar will be the dominant feature in the inner region and will not appear in the outer one, leaving spirals to be identified.

4 RESULTS

4.1 Disc evolution and migration

The results are shown at different times up to ∼5 Gyr, where it is ensured that non-axisymmetric interactions have taken place. That is, spiral arms have grown, churned, and faded, leaving a cumulative radial migration effect upon the galaxy. Since our simulations are pure N-body, there is no need to integrate further as new spiral arms are not excited at later times. Three different simulations are presented in Fig. 2 and show the evolution of secular resonances. These three galaxies are chosen to show examples of disc dominance, halo dominance, and something intermediate. It therefore shows different number and strengths of spiral arms, as we expect. It is clearly visible that as the dark matter halo starts to dominate, the disc is unable to form larger, grand-design type spiral arms and instead form many weaker spiral arms. When the disc dominates there is also a significant radial 'puffing' up of the disc leading to a radially extended structure at later times.

The evolution is shown at three different points in time. The first two snapshots are taken from within the first fifth of the integration time ($t \approx 0.3$ Gyr and $t \approx 1$ Gyr, respectively) as there is very little significant secular evolution beyond that point. The last snapshot is at $t \approx 4$ Gyr, and does not change significantly after.

To allow for secular evolution and its effect on the migration, a few different combinations of 'initial' and 'final' times are investigated in ΔL_z–$L_{z,\rm i}$ space, that is the change in angular momentum compared to the initial angular momentum. This can be seen in Fig. 3 and here spirals arms manifest as diagonal lines near the corotation radius of a spiral or bar. Particles located exactly at corotation show no change to the angular momentum and those inside corotation would migrate outwards and vice versa. So particles inside have a positive change in angular momentum and stars outside have a negative one, giving rise to the diagonal ridges.

Fig. 3 shows that as the simulations produce different number and strength of spiral arms, the radial migration that takes place also differs. It is clear that a more massive halo produces many smaller spiral arms, as seen in Fig. 2, which produce the weak diagonal features. When the halo dominance grows there is much less total migration as evident in the spread in ΔL_z. This result is to be expected since a weaker arm produces a smaller torque and hence, smaller changes to the angular momentum.

As can be seen in the upper two rows of Fig. 2, a bar eventually forms in some of these simulations and appears to do so whenever the galaxy can readily form spirals. The prominent formation of a bar could potentially be prevented with a stronger bulge, creating an inner Lindblad resonance to serve as a barrier against formation. Once the bar forms it grows to be a rather large $m = 2$ resonance which has a tendency to overshadow smaller spiral features.

We can investigate the appearance of a bar and spirals more closely using the Fourier analysis outlined in Section 3.5. The power

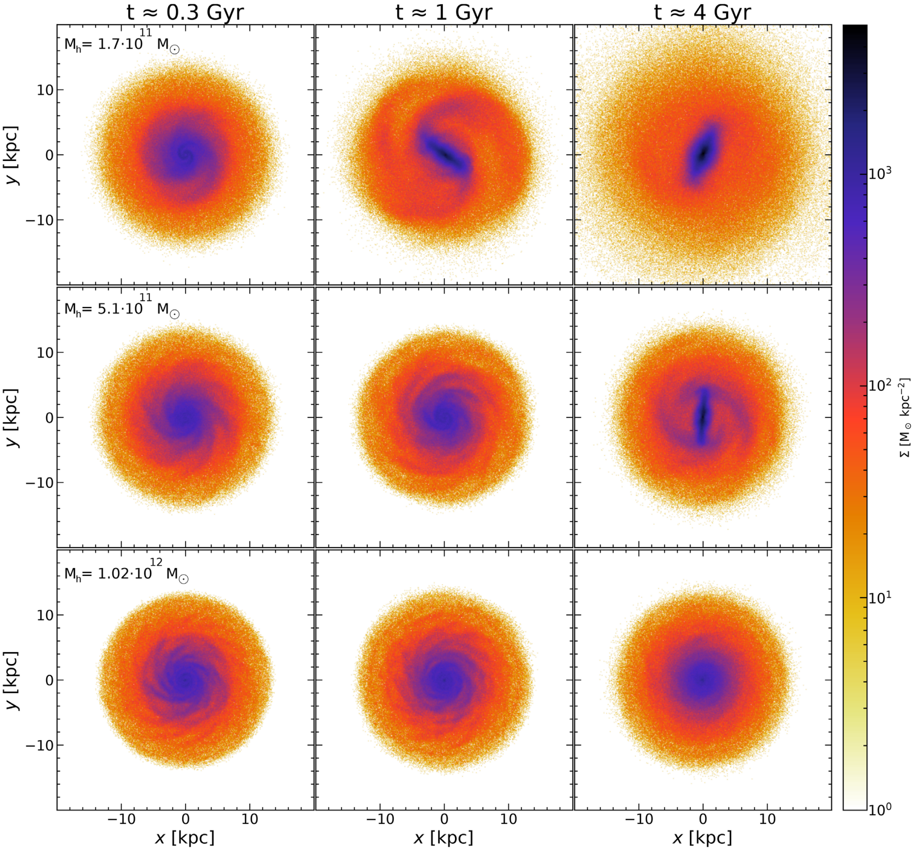

Figure 2. Face-on view of three of the different simulated galaxies, these are the disc corresponding to dark matter halo masses of 1.7×10^{11}, 5.1×10^{11}, and 1.02×10^{12} $M_\odot$ in descending order along the rows. The columns show snapshots taken at $t \approx 0.3$ Gyr, $t \approx 1$ Gyr, and $t \approx 4$ Gyr, respectively, as indicated at the top, and the colour shows the stellar density. In general we find that the number of spiral arms increases with the halo mass while their strength appears to decline.

spectrum and amplitudes of the dominant modes are shown in Fig. 4. The growth of a stable bar is seen very clearly in the amplitude of the $m = 2$ mode in the lightest two halo mass simulations. The evolution of the $m = 2$ mode is shown for each simulation, as this is usually the dominant mode when a bar forms. Also shown is the evolution of other prominent modes in each respective simulation. The lower mass simulation has a few occasions with $m = 3$ modes which are rather short-lived. The noisiness observed in this plot could well be due to the presence of material arms which are short-lived and therefore are difficult to capture in the power spectrum, but are very readily visible in plots such as Figs 2 and 3. It is still possible to observe a hint of a large $m = 6$ mode at the start of the heaviest halo mass simulation, which is in line with the predictions for the multitude of spiral arms when the disc dominance is low.

4.2 Migration and action

4.2.1 Vertical action

The appearance of different spiral structures depending on dominance of the disc has been established in our simulations. In Section 2, we made the argument that the amount of radial migration at various heights above the mid-plane of the disc could be linked to the spiral strength. To characterize the vertical distribution of our migrators, we use vertical action instead of position or velocity as the vertical action does not oscillate on orbital time-scales while

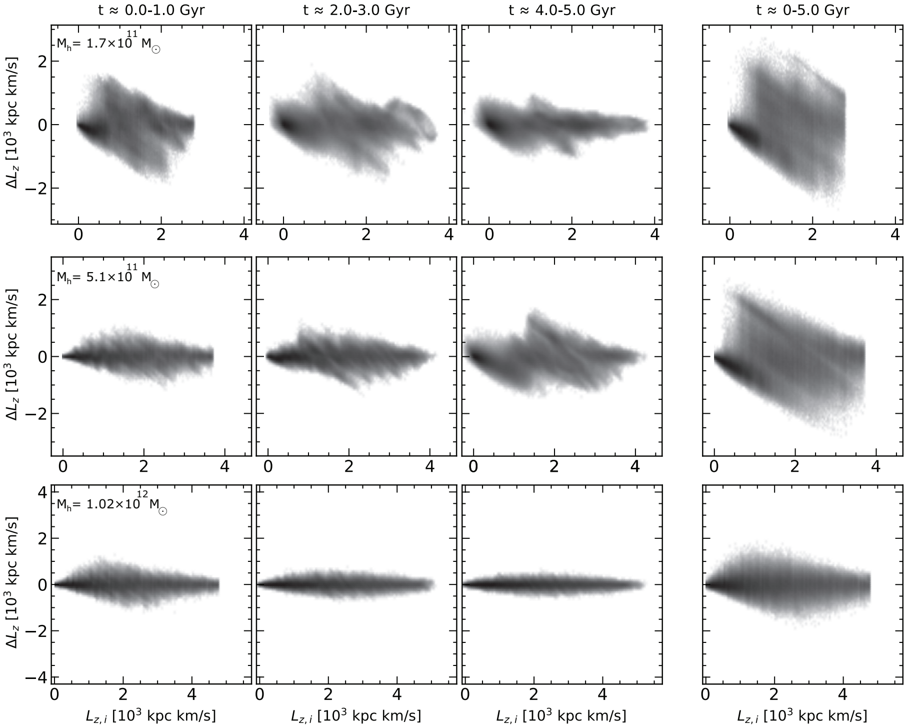

Figure 3. The change in angular momentum ΔL_z against initial angular momentum, $L_{z,\mathrm{i}}$ compared at various times in the simulation. The simulations are the same as in Fig. 2 and shown in the same order. The snapshot times compared are seen above the first row. The shading corresponds to number density. We can see that the weaker spirals seen in Fig. 2, here generate less radial migration as is to be expected.

position and velocity does. The data are binned in initial vertical action, J_z, and initial angular momentum, L_z, as a proxy for radius. For each bin we calculate the standard deviation of the change in angular momentum, $\sigma_{\Delta L_z}$, which quantifies the amount of radial migration or radial migration efficiency. The result of this is seen in Fig. 5. For the lightest halo that showed strong spirals and an eventual bar, there is strong migration at almost all J_z and in almost all of the disc in L_z, save for the innermost parts. The migration at high vertical action gets weaker as the halo grows in mass and once the halo becomes relatively dominant in the bottom plot radial migration appears to decrease as the vertical action is increased.

The different behaviours described here can be quantified more clearly by recognizing that the discussion of migration at various vertical actions is a discussion of a slope in $\sigma_{\Delta L_z}$ with J_z. To investigate any possible radial dependences, three slices in L_z with widths $(1/50)L_z^{\max}$ at 0.4, 0.6, and 0.8 of the maximum L_z are taken, while the innermost cut at 0.2 is omitted as it contains orbits which belong to a bar once it forms. The disc does not extend beyond ~15 kpc, so the maximum L_z corresponds to that of near circular orbits at this radius. To clarify, we take the particles within a $(1/50)L_z^{\max}$ width of the specified locations regardless of their J_z, creating three ‘slices’. The separation into these three different slices allows for the comparison of migration as a function of J_z at different distances from the centre of the galaxy. The particles in the slices are binned again in the J_z direction, with 300 particles in each bin. We perform a least-squares linear fit for $\sigma_{\Delta L_z}$ as a function of J_z where the gradient of the line we fit will reflect how the vertical action of a particle affects its radial migration.

However, comparing the slope of the lines in $\sigma_{\Delta L_z}$ and J_z as is would not prove very informative, because different parts of a galaxy in L_z reach different maximum J_z due to the difference in the gravitational potential, as clearly seen in Fig. 5. In order to correct for this we divide J_z in the slices by close to their largest value.[2] This correction normalizes J_z across the disc.

---

[2] The normalizing value is the median of J_z values in their second highest bin in the slice, which is chosen to avoid outliers. Our results are robust to the specific choice of normalization. Normalizing against a differentpercentile would not affect the result as it is the behaviour across the disc which is of interest.

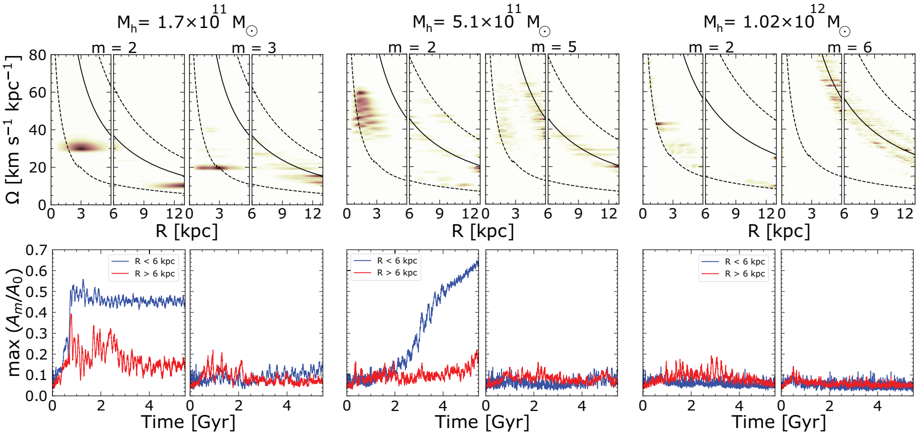

Figure 4. *Upper row:* For each simulation in Fig. 2, with mass indicated at the top, the power spectrum of the mode indicated above the plot. Shown are the angular velocities against radius. Solid lines indicate the corotation resonance with the disc and dashed lines mark the inner and outer Lindblad resonances. Multiple patterns can be seen across the various power spectra as horizontal lines since bars and spiral patterns have a fixed angular velocity. A bar can be seen in the two leftmost simulations for $m = 2$ at $\Omega \approx 33$ km s^{-1} kpc^{-1} and $\Omega \approx 50$ km s^{-1} kpc^{-1} for the leftmost and middle simulations, respectively. *Bottom row:* The corresponding amplitudes of the modes. Just like the power spectra above it is divided into an inner and outer part divided at 6 kpc. The growth and decay of many different modes is visible. The two leftmost simulations show the rise of a prominent bar in the $m = 2$ mode. They are even more apparent within 6 kpc, reinforcing that it matches the patterns in the upper row figures. Some patterns are seen outside 6 kpc for these simulations as well and the lightest simulation shows a rise in an $m = 3$ mode that dies after 2 Gyr. For the heaviest simulation, a very brief spike in $m = 6$ can be observed in the amplitude but is difficult to discern in the spectogram.

It is also problematic that the different simulations have different ranges of $\sigma_{\Delta L_z}$, since total migration decreases when the spiral arms become weaker (i.e. with increasing halo mass). For this correction $\sigma_{\Delta L_z}$ is divided by its mean around $J_z = 0$ in each slice, which normalizes the results across different dark matter halo masses.

We wish to know the vertical gradient of radial migration regardless of the total amount of radial migration or galactocentric radius, which this normalization will allow.

To give an example of this normalization Fig. 6 shows the slices at 0.6 $L_z^{\max}$. The slices and linear fits are seen for simulations with six different dark matter halo masses, ranging from lightest to heaviest. The gradient in radial migration as a function of vertical action is shown as red lines. As the halo mass is increased and the disc dominance is decreased, we see that the slope becomes steeper and migration less significant for high J_z particles, making the changes hinted at in Fig. 5 clear.

The three slices of the disc are compiled to show the slopes in Fig. 7 for the various dark matter halo masses and at the different angular momenta. The slope is calculated for each random initialization with the same halo mass set-up and the standard deviation of those values is used to give the error bars shown.

Fig. 7 shows a quantified version of the arguments made above regarding the vertical gradient of the radial migration. For the lower halo masses, we have strongly self-gravitating discs that result in normalized slopes closer to zero. These cases of low halo mass correspond to the situation seen in the top plot, and to some extent the middle, of Fig. 5. A separate regime appears as the halo mass increases and the disc is less dominant. Now the slopes are larger, showing a radial migration bias for low-$J_{z,\mathrm{i}}$ stars much like the 'provenance bias' of Vera-Ciro et al. (2014) discussed in Section 2. There is a smooth transition between the two different regimes discussed and the trend is too strong to be explained by the random scatter that we can see.

It can be clearly seen in Fig. 7 that by changing the relative gravitational influence of the halo and the disc in a galaxy simulation, and therefore the resulting spiral morphology, you can change the extent to which stars with lower vertical action are preferentially radially migrated.

4.2.2 *Radial action*

It is also useful to perform an investigation into the behaviour of radial migration as a function of the radial action in our simulations. Just as the vertical action is a good measure of how vertically heated an orbit is (see Section 2.1) the radial action is a radial equivalent and is related to the eccentricity of a stellar orbit. Daniel & Wyse (2018) found that radial migration was less efficient in populations with larger radial velocity dispersion. A similar result was also found by Solway et al. (2012) who looked at the angular momentum changes compared to initial eccentricity. They showed that angular momentum changes were larger for particles with smaller eccentricities.

These results can be understood within the theory as well. If the eccentricity of a particle is large its angular velocity will oscillate as it orbits and will only match that of a steadily rotating spiral for a brief period of time making it less likely to enter corotation with the spiral. The more circular the orbit of the particle the more readily it responds to the resonance. This argument is similar to the arguments

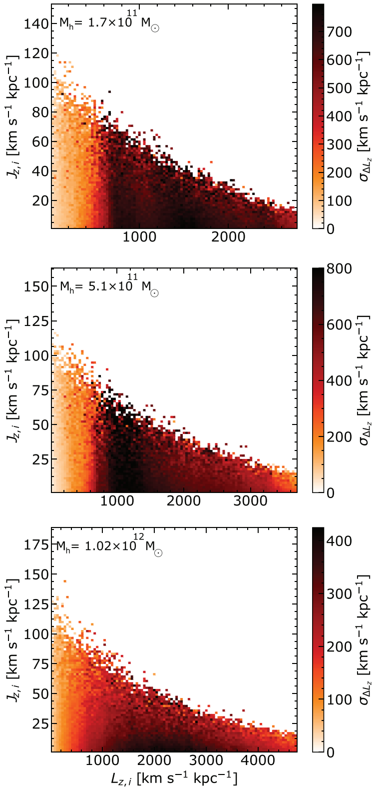

Figure 5. Initial vertical action and angular momentum of the same three galaxies shown in Fig. 2 and in the same order. The space is binned 100 × 100 to show the standard deviation of angular momentum changes between $t = 0$ Gyr and $t \approx 5$ Gyr. For the top plot with lightest halo the migration appears to stay the same across all J_z in contrast to the bottom plot with the heaviest halo which shows a clear decrease in radial migration as J_z increases.

made regarding the vertical bias of migrators with a key difference being that a vertical oscillation brings the particle away from the disc which a radial oscillation will not.

To perform this analysis, we use the same procedure as in the preceding section for vertical action. Three slices at separate $L_{z,\mathrm{i}}$ are cut in the space of $J_{r,\mathrm{i}}$ and $L_{z,\mathrm{i}}$. Within these slices the standard deviation of the angular momentum changes, $\sigma_{\Delta L_z}$, are taken within bins of 300 particles each. The linear slope is normalized in the same manner and calculated for each halo mass simulation and for all the different random initializations.

We present the result in Fig. 8. Here, the gradient of migration shows no strong trend with increasing halo mass. The value of the slope is almost constant at around −0.25, which means that radial migration is more efficient for less eccentric orbits, in agreement with the results and theory stated in the previous paragraphs. The innermost part of the galaxy contains orbits that belong to the bar and has strongly non-linear behaviour between the radial action and the migration efficiency. Fitting a line to that region of the disc yields a large scatter in slope values which give no real information on the migration process and as such is not shown here.

When comparing Fig. 8 with Fig. 7 it is clear that there is a difference in the response to disc dominance and stronger/weaker spirals between the two axes which could be caused by the former being confined to the disc while the other is not.

4.2.3 *Action conservation*

In the previous sections, the radial migration has been compared between snapshots taken at $t = 0$ and $t \approx 5$ Gyr, while the vertical action has been calculated for $t = 0$, assuming it has not changed by the time the particle migrates. To be certain of this we must investigate how well the vertical action is conserved over the duration. Conservation of vertical action was studied by Solway et al. (2012) who concluded that vertical action is conserved on average while it may change for individual particles. This work was expanded on by Vera-Ciro & D'Onghia (2016) who compared two *N*-body spiral galaxies. One was set up to form multi-armed spirals and the other, more Milky Way-like galaxy, to form a bar. They found that with the formation of a bar, the actions are not very well conserved.

For six of our different halo mass simulations, we compare the value of the vertical action at $t \approx 0$ Gyr and $t \approx 3$ Gyr (called here $J_{z,\mathrm{i}}$ and $J_{z,\mathrm{f}}$ respectively)[3] as a binned density map in Fig. 9. Beyond $t \approx 3$ Gyr the data are only blurred by noise. We include the median and 1σ range of $J_{z,\mathrm{f}}$ for 20 bins in $J_{z,\mathrm{i}}$ as blue solid and dashed lines, respectively. This can be compared to exact action conservation $J_{z,\mathrm{f}} = J_{z,\mathrm{i}}$ shown as a solid green line.

The lightest halo masses in Fig. 9 show that when the disc is dominant and a bar forms, as seen in Fig. 2, there is a large spread in vertical action around action conservation, in agreement with Vera-Ciro & D'Onghia (2016). However, the median lies close to the line $J_{z,\mathrm{i}} = J_{z,\mathrm{f}}$. The heavier haloes show a smaller spread about the line of conservation, and in agreement with Solway et al. (2012) their medians align almost exactly with $J_{z,\mathrm{i}} = J_{z,\mathrm{f}}$. While individual bins show a large spread the median is sufficiently close to $J_{z,\mathrm{i}} = J_{z,\mathrm{f}}$ that $J_{z,\mathrm{i}}$ is a good predictor of a typical J_z for all halo masses.

It is however clear that vertical action can, for individual particles, change significantly. We investigate to what extent radial migration can cause this by again comparing the same initial and final vertical actions in a binned histogram as above but coloured by radial migration efficiency, $\sigma_{\Delta L_z}$, instead of density. This is shown in Fig. 10 with the median and 1σ range from the density histogram overplotted.

From the discussion in Section 2, churning is not expected to change the radial action. Fig. 10 shows that the most significant migration is around the line of conservation of J_z in all simulations. For the lighter haloes there is still a spread to larger $J_{z,\mathrm{f}}$ where migration efficiency is also lower, so the most migrated particles do not change their action significantly. Thus, the change of vertical action is likely due to heating in the bar or a similar process and not due to the migration itself. The fact that most of the particles are located near the line of conservation, and that this is where most of the radial migration occurs, supports the idea that the behaviour in Fig. 7 is a gradient for radial migration by churning and is not significantly polluted by another process

---

[3] As in e.g. Trick, Coronado & Rix (2019), we use $\sqrt{J}$ to reveal structure at lower actions.

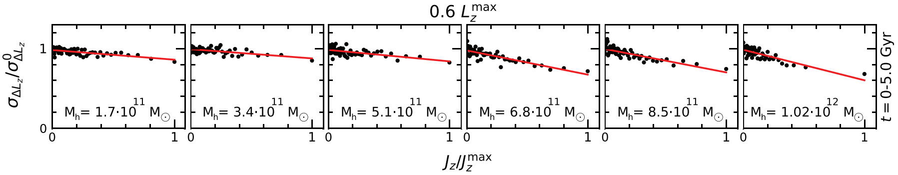

Figure 6. Standard deviation of the change in angular momentum, $\sigma_{\Delta L_z}$ normalized by the value at $J_z = 0$ against the vertical action normalized to the largest vertical action within the slice. Slices are vertical in Fig. 5 taken at 0.6 of $L_z^{\max}$ and shown for a representative range of different halo mass simulations, ranging from the lightest on the left to the heaviest on the right. These slopes are taken when comparing angular momentum at $t \approx 0$ Gyr and $t \approx 5$ Gyr. The red lines show the linear fits from which we get the slopes.

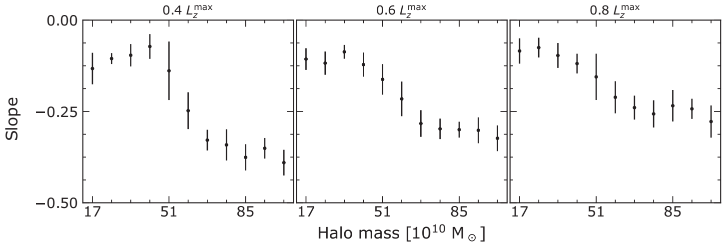

Figure 7. Compilation of all slopes calculated as described in Section 4.2.1 and seen as red lines in Fig. 6. Slopes are plotted against halo mass showing a tendency for flatter gradients for disc-dominated systems and a steeper ones for halo-dominated ones.

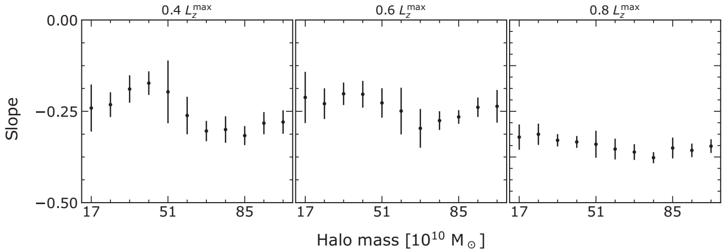

Figure 8. Similar to Fig. 7 using radial action instead of vertical action to investigate the gradient of migration. The radial action slope appears to be independent of halo mass, contrary to the vertical action counterpart.

4.3 Comparison to Vera-Ciro

As was shown in Section 4.2.1, the vertical gradient of radial migration changes depending on the disc dominance of the initial conditions. Despite this, literature results generally claim that there is less migration at larger vertical excursions as discussed in Section 2. Particularly, Vera-Ciro et al. (2014, 2016) has studied the radial migration in simulations with different spiral morphologies where they find a significant negative vertical gradient for radial migration regardless of spiral morphology, contrasting our results, and we wish to understand our results within this context. We have shown that high vertical action will prevent a star from being churned in cases where the disc is less dominant in the galaxy. The galaxies that are set up in these papers may simply be in a regime where this is the case. In order to investigate this thoroughly we have chosen to recreate and compare with the galaxy from Vera-Ciro et al. (2016) labelled `HD-MW` or ‘Milky Way-like’. The dominance of the disc is changed directly through the disc mass and we have used five set-ups with [0.245, 0.45, 1, 1.5, 2] times the original disc mass, 4×10^{10} M$_\odot$. 10 extra seeds are again generated for each simulation to test for stochastic robustness and the same procedure described in Section 4.2.1 is performed to generate Fig. 11. Now the slope flattens along the x-axis as they are plotted against disc mass instead of halo mass. It can be seen that while there is a tendency for larger vertical action to reduce radial migration at $M_\mathrm{d} = 4 \times 10^{10}$ M$_\odot$, it is not very prominent and becomes stronger/weaker if the mass of the disc is smaller/larger.

In fig. 4 of Vera-Ciro et al. (2016), the distribution of velocity dispersion is shown in terms of initial guiding centre radius, $R_{\mathrm{g,i}}$, and fractional change in guiding centre radius, $\delta R_\mathrm{g} = \ln\left(R_\mathrm{g}/R_{\mathrm{g,i}}\right)$ between an initial time and at $t \sim 2$ Gyr. The velocity dispersion is the initial

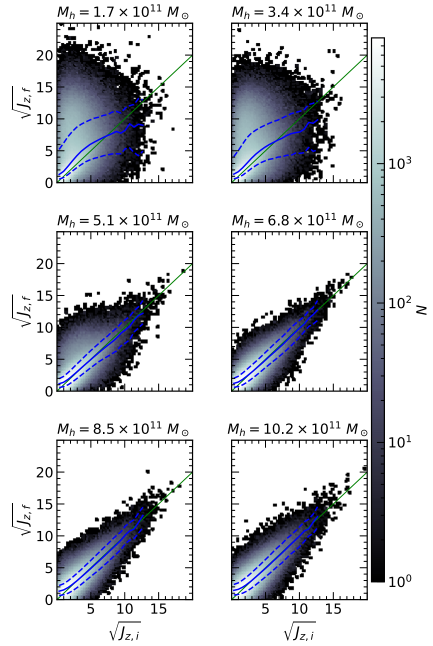

Figure 9. Number density distribution of $\sqrt{J_{z,\mathrm{i}}}$ and $\sqrt{J_{z,\mathrm{f}}}$ in units of (kpc km s^{-1})$^{1/2}$ calculated at $t = 0$ and $t \approx 3$ Gyr, respectively. Also shown is the median value of $\sqrt{J_{z,\mathrm{f}}}$ in 20 bins of $\sqrt{J_{z,\mathrm{i}}}$ as a solid blue line. Dashed blue lines show the 1σ range and exact action conservation $J_{z,\mathrm{f}} = J_{z,\mathrm{i}}$ is shown in green. The results are shown for the same simulations as in Fig. 6 and indicated above each individual plot.

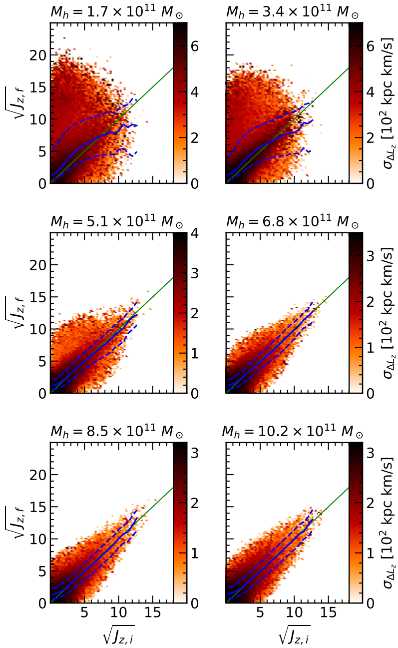

Figure 10. Same as Fig. 9 with the colour corresponding to the same radial migration efficiency as Fig. 5 instead of number density.

one in units of the average velocity dispersion at that radius. That is

$$\delta\sigma_{z,\mathrm{i}} = \ln \frac{\sigma_{z,\mathrm{i}}(R_{\mathrm{g,i}}, \delta R_{\mathrm{g}})}{|\sigma_{z,\mathrm{i}}(R_{g,\mathrm{i}})|}. \tag{12}$$

Using this they claim a lower velocity dispersion for particles of larger δR_{g}. For comparison the three simulations shown in Fig. 3 are investigated to show the distribution in vertical action, using a similar procedure such that

$$\delta J_z = \ln \frac{J_{z,\mathrm{i}}(L_{z,\mathrm{i}}, \Delta L_z)}{|J_{z,\mathrm{i}}(L_{z,\mathrm{i}})|}. \tag{13}$$

This equation normalizes the vertical action in a manner similar to how the normalization in J_z was carried out for the slope calculation. The result of this can be seen in Fig. 12. It is clear also here that disc dominance flattens the gradient in radial migration and vertical action, as seen in the previous results.

5 CONCLUSIONS

In this paper, we have studied radial migration efficiency as a function of vertical and radial action as well as how these functions depend on disc dominance. We have used a large suite of N-body simulations of isolated galaxies where we have varied the total amount of mass within the dark matter halo in order to change the dominance of the disc and thereby create spiral structures of different number and strength.

The main focus of this study has been to identify a relationship between disc dominance and the subsequent radial migration for different heights above the disc mid-plane, measured through the vertical action, J_z. This link has not been previously established and we have shown that if the disc of a galaxy is made more dominant, and therefore the spiral arms within it made stronger and fewer, radial migration can occur at larger vertical extents. This adds to our current understanding of radial migration in galaxies like the Milky Way and is instrumental in the implementation of radial migration in analytical studies of galactic dynamics.

Previous studies that have looked at the vertical gradient of radial migration have not reached the same conclusion (Solway et al. 2012; Vera-Ciro et al. 2014; Halle et al. 2015; Vera-Ciro et al. 2016). To understand this we have studied the results of Vera-Ciro et al. (2016) extensively within the context of our findings as they also investigate the role of different non-axisymmetric patterns on radial migration, partly in terms of vertical velocity dispersion, σ_z. They find that migrators are a subset of stars with small vertical velocity dispersions regardless of the observed spiral morphology achieved, in contrast to our findings. One of their simulations was reconstructed here and

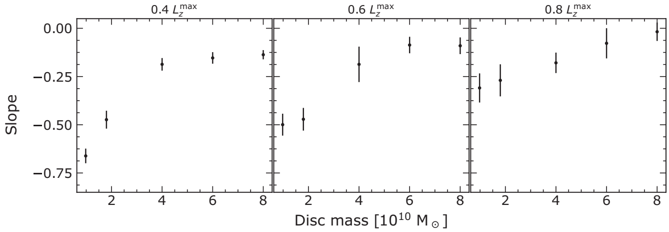

Figure 11. Similar to Fig. 7 but instead slopes are plotted against disc mass, meaning that the disc becomes more dominant along the *x*-axis. The simulations used to evaluate the slopes are recreations of the `HD-MW` simulation of Vera-Ciro et al. (2016). It is clear that the slope flattens with disc dominance.

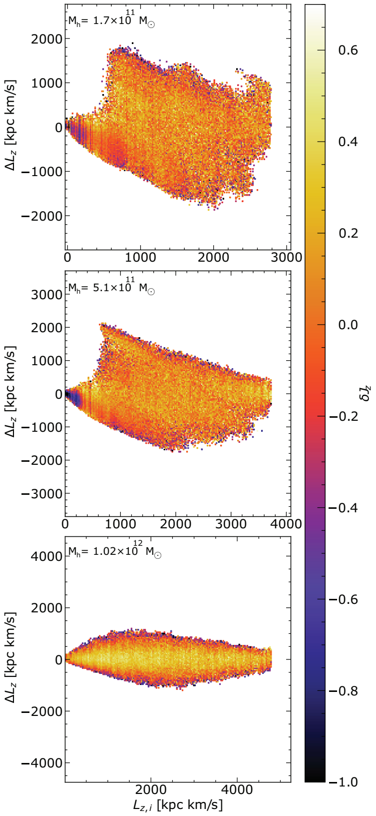

Figure 12. Same as the rightmost column of Fig. 3 but coloured by the log of the vertical action divided by the mean of the vertical action at that angular momentum. In the more disc dominated systems, we can see that the particles that migrate do not have very significantly different J_z than those that do not migrate as much. When the disc becomes less dominant, migration is more prominent among particles of low vertical action.

tested with different disc dominance to produce the results we have seen. We show that we are able to create different vertical gradients of radial migration depending on the disc dominance in this case as well. Within these findings, the results of Vera-Ciro et al. (2016) likely stems from a sampling of a specific part of the parameter space where there is less variation in the vertical gradient of migration.

In addition we studied the gradient of radial migration with radial action as a proxy for eccentricity. This relationship has previously been studied by Daniel & Wyse (2018) who showed that radial migration was less efficient in populations with larger radial velocity dispersion and before that by Solway et al. (2012) who compared ΔL_z with eccentricity to find similar results. Our simulations are in agreement with these two results regardless of the initial conditions. The strength of the spiral arms does not have a noticeable effect on which particles are radially migrated.

Our result for the radial action and vertical action contrast one another. This means that there is a difference in the response to corotation with increasing action due to the direction being along the disc or orthogonal to it. This discrepancy is interesting and invites further analysis.

The vertical action is less well conserved in our disc dominant simulations with a bar. The method by which the vertical gradient in Fig. 7 is determined relies on the initial vertical action, $J_{z,\mathrm{i}}$, reflecting the vertical action around the time of migration. However, as the action is well conserved on average for the majority of the simulations and only slightly deviates from average conservation in our most disc dominant simulations, our vertical gradient determinations should not be severely affected. One method to eliminate this issue would be to determine the vertical action as closely as possible to the time of migration, a feat which demands more detailed analysis.

These findings matter for stars with large vertical excursions, which are typically part of the oldest populations in the disc. Our results imply that, if the disc is sufficiently dominant, stars can be migrated despite being part of such a vertically extended population. Any interpretation of the distribution of stars as a function of age in the Milky Way would be affected by this, and it has significant implications for the formation and evolution of thick discs.

Previous work studying radial migration and its implications have made use of various combinations of analytical models and simulations both hydrodynamical and *N*-body, full or using static potentials. Here, we present the combined result of over a hundred full *N*-body simulations to reduce the stochasticity of our findings. Results like these which aid in describing the nature of radial migration are necessary to further the analytical modelling which relies on descriptions provided by studies of this kind.

Radial migration is still not fully understood and will certainly be the subject of future studies both numerical and analytical. Through the results we have presented here, the desired vertical gradient of radial migration can be tuned through the choice of relative gravitational strength of the disc to that of the dark matter halo.

ACKNOWLEDGEMENTS

We thank members of Lund Observatory as well as an anonymous referee for helpful comments and ideas. Computations for this study were performed on equipment funded by a grant from the Royal Physiographic Society in Lund. PJM is supported by a research project grant from the Swedish Research Council (Vetenskaprådet). DH and PJM gratefully acknowledge support from the Swedish National Space Agency (SNSA Dnr 74/14 and SNSA Dnr 64/17).

REFERENCES

Aumer M., Binney J., 2017, MNRAS, 470, 2113
Aumer M., Binney J., Schönrich R., 2016a, MNRAS, 459, 3326
Aumer M., Binney J., Schönrich R., 2016b, MNRAS, 462, 1697
Aumer M., Binney J., Schönrich R., 2017, MNRAS, 470, 3685
Bensby T., Feltzing S., Oey M. S., 2014, A&A, 562, A71
Bergemann M. et al., 2014, A&A, 565, A89
Binney J., 2012, MNRAS, 426, 1324
Binney J., Tremaine S., 2008, Galactic Dynamics: Second Edition, 2nd edn, Princeton University Press, Princeton, New Jersey, US
D'Onghia E., 2015, ApJ, 808, L8
Daniel K. J., Wyse R. F. G., 2018, MNRAS, 476, 1561
Dehnen W., 1999, AJ, 118, 1201
Dehnen W., 2000, ApJ, 536, L39
Dehnen W., 2002, J. Comput. Phys., 179, 27
Dehnen W., McLaughlin D. E., 2005, MNRAS, 363, 1057
Edvardsson B., Andersen J., Gustafsson B., Lambert D. L., Nissen P. E., Tomkin J., 1993, A&A, 500, 391
Frankel N., Rix H.-W., Ting Y.-S., Ness M., Hogg D. W., 2018, ApJ, 865, 96
Halle A., Di Matteo P., Haywood M., Combes F., 2015, A&A, 578, A58
Hernquist L., 1990, ApJ, 356, 359
Lynden-Bell D., Kalnajs A. J., 1972, MNRAS, 157, 1
McMillan P. J., 2017, MNRAS, 465, 76
McMillan P. J., Dehnen W., 2007, MNRAS, 378, 541
Minchev I., Famaey B., Quillen A. C., Dehnen W., Martig M., Siebert A., 2012, A&A, 548, A127
Minchev I., Martig M., Streich D., Scannapieco C., de Jong R. S., Steinmetz M., 2015, ApJ, 804, L9
Minchev I. et al., 2018, MNRAS, 481, 1645
Press W. H., Teukolsky S. A., Vetterling W. T., Flannery B. P., 1992, Numerical Recipes in C. The Art of Scientific Computing, 2nd edn, Cambridge University Press, Cambridge, UK
Roškar R., Debattista V. P., Quinn T. R., Stinson G. S., Wadsley J., 2008, ApJ, 684, L79
Roškar R., Debattista V. P., Quinn T. R., Wadsley J., 2012, MNRAS, 426, 2089
Schönrich R., Binney J., 2009, MNRAS, 396, 203
Schönrich R., McMillan P. J., 2017, MNRAS, 467, 1154
Sellwood J. A., Binney J. J., 2002, MNRAS, 336, 785
Solway M., Sellwood J. A., Schönrich R., 2012, MNRAS, 422, 1363
Teuben P., 1995, in Shaw R. A., Payne H. E., Hayes J. J. E., eds, ASP Conf. Ser. Vol. 77, Astronomical Data Analysis Software and Systems IV. Astron. Soc. Pac., San Francisco, p. 398
Toomre A., 1964, ApJ, 139, 1217
Toyouchi D., Chiba M., 2016, ApJ, 833, 239
Trick W. H., Coronado J., Rix H.-W., 2019, MNRAS, 484, 3291
Vera-Ciro C., D'Onghia E., 2016, ApJ, 824, 39
Vera-Ciro C., D'Onghia E., Navarro J., Abadi M., 2014, ApJ, 794, 173
Vera-Ciro C., D'Onghia E., Navarro J. F., 2016, ApJ, 833, 42

This paper has been typeset from a TEX/LATEX file prepared by the author.

Paper II

Paper II: The velocity distribution of white dwarfs in Gaia EDR3

Mikkola, D.; McMillan, P. J.; Hobbs, D.; Wimarsson, J (2022)
Monthly Notices of the Royal Astronomical Society, Volume 512, Issue 4, pp. 6201-6216

My contribution:

The original idea came from PM to apply the method of Dehnen (1998) to DR2 (Gaia Collaboration et al., 2018a). John Wimarsson (JW) wrote the initial, core parts of the code with support from DM and PM. DM took over responsibility for the code, finished writing it as well as developed all of the analysis tools. Further developments for the code were implemented with input from PM and DH, including the multigrid approach. DM and PM chose white dwarfs as targets and DM acquired the data from the Gaia archive. DM carried out the analysis with guidance from his supervisors DH and PM. DM reviewed existing literature on velocity distributions as well as white dwarfs and their bifurcation. DM wrote the paper, with rounds of review between DM, PM, and DH. DM submitted the report and went through editing rounds with an anonymous referee's useful comments which lead to further clarity and discussion in the paper. The paper was then accepted for publication.

Monthly Notices
of the
ROYAL ASTRONOMICAL SOCIETY

MNRAS **00,** 1 (2022)
Advance Access publication 2022 February 22

https://doi.org/10.1093/mnras/stac434

The velocity distribution of white dwarfs in *Gaia* EDR3

Daniel Mikkola,[1]⋆ Paul J. McMillan ,[1] David Hobbs[1] and John Wimarsson[1,2]

[1] *Lund Observatory, Department of Astronomy and Theoretical Physics, Lund University, Box 43, SE-22100 Lund, Sweden*
[2] *Space Research & Planetary Sciences, Physics Institute, University of Bern, Gesellschaftsstrasse 6, CH-3012 Bern, Switzerland*

Accepted 2022 February 14. Received 2022 March 8; in original form 2021 October 25

ABSTRACT

Using a penalized maximum likelihood, we estimate, for the first time, the velocity distribution of white dwarfs in the solar neighbourhood. Our sample consists of 129 675 white dwarfs within 500 pc in *Gaia* Early Data Release 3. The white dwarf velocity distributions reveal a similar structure to the rest of the solar neighbourhood stars, reflecting that white dwarfs are subject to the same dynamical processes. In the velocity distribution for three magnitude-binned subsamples, we, however, find a novel structure at $(U, V) = (7, -19)\ \mathrm{km\,s^{-1}}$ in fainter samples, potentially related to the Coma Berenices stream. We also see a double-peaked feature in $U - W$ at $U \approx -30\ \mathrm{km\,s^{-1}}$ and in $V - W$ at $V \approx -20\ \mathrm{km\,s^{-1}}$ for fainter samples. We determine the velocity distribution and velocity moments as a function of absolute magnitude for two samples based on the bifurcation identified in *Gaia* Data Release 2 in the colour–magnitude diagram. The brighter, redder sequence has a larger velocity dispersion than the fainter, bluer sequence across all magnitudes. It is hard to reconcile this kinematic difference with a bifurcation caused purely by atmospheric composition, while it fits neatly with a significant age difference between the two sequences. Our results provide novel insights into the kinematic properties of white dwarfs and demonstrate the power of analytical techniques that work for the large fraction of stars that do not have measured radial velocities in the current era of large-scale astrometric surveys.

Key words: methods: data analysis – methods: statistical – stars: kinematics and dynamics – Galaxy: kinematics and dynamics – solar neighbourhood – Galaxy: structure.

1 INTRODUCTION

The present-day structure and the history of the Galaxy are encoded not just in the positions of its stars but also in their kinematics. It is well established that the present velocity distribution in the solar neighbourhood has a great deal of structure in it (e.g. Gaia Collaboration 2018c) for which there are multiple possible causes. Suggested origins for overdensities include dissolving open clusters, resonances from large-scale density waves such as the Galactic bar and spiral arms, accreted populations from galaxy mergers, and phase mixing from nearby satellite galaxies (e.g. Antoja et al. 2012; Kushniruk, Schirmer & Bensby 2017). Understanding this substructure is a part of understanding the dynamical history of the Milky Way.

The phase-space distribution of stars within the Milky Way has been studied extensively over the last decades (see Gaia Collaboration 2018c and references therein) to reveal this complicated structure, especially since the *Hipparcos* mission (Perryman et al. 1997) and more so with its successor *Gaia*'s (Gaia Collaboration 2016) recent second and third data release (henceforth DR2 and EDR3, respectively; Gaia Collaboration 2018a, 2021a).

The astrometry of *Gaia* provides proper motions and positions for ∼1.5 billion sources with great precision, which is an enormous leap forward from its predecessor, which observed ∼120 000 sources. The *Gaia* data have only been available for a few years but the potential for kinematic study has already been demonstrated. For example, Bovy (2017) accurately measured the Oort constants A and B as well as for the first time the non-axisymmetric constants C and K. In Monari et al. (2018), it was shown that the moving group Coma Berenices is limited to negative Galactic latitudes and likely has not undergone phase mixing in the Galactic potential. The kinematic structure of the solar neighbourhood has been studied in unprecedented detail to reveal many new and old structures (e.g. Kushniruk et al. 2017; Gaia Collaboration 2018c) as well as arches (Antoja et al. 2018). Beyond velocity space, the solar neighbourhood has also been explored in orbit space (e.g. Trick, Coronado & Rix 2019; Trick et al. 2021; Trick 2022), showing ridges which can manifest themselves as streams and structures in velocity space. Understanding the kinematic substructure of the Galaxy will require exploration in both velocity and orbit space, which becomes far more accessible due to the wealth of data provided by missions such as *Gaia*.

Even though EDR3 provides accurate astrometry and photometry for a great number of sources, it does not contain full 3D phase-space information for all of them as some lack measured radial velocity. This means that for most individual stars only the position and proper motions are available as in the *Hipparcos* catalogue. In fact, the number of sources with radial velocities in *Gaia* EDR3, ∼7.2 million, is dwarfed by the number of sources with at least position and proper motions, ∼1.5 billion. This means that the radial

---

⋆ E-mail: mikkola@astro.lu.se

velocity sample contains only $\sim$0.5 per cent of sources with the full astrometric solution.

This limitation can be circumnavigated by studying properties of an entire sample rather than the individual stars. This was demonstrated in two seminal papers, Dehnen & Binney (1998) (hereafter DB98) and the follow-up paper Dehnen (1998) for *Hipparcos*. DB98 calculated the mean motion and velocity dispersions for populations taken from a sample of 11 865 single main-sequence stars, and Dehnen (1998) estimated the velocity distribution $f(\boldsymbol{v})$ for a similar sample of stars. Both of these papers use the approximation that the velocity distribution is consistent for the full sample and is spread across the full sky.

As previously mentioned, there are $\sim$1.5 billion sources in EDR3. This sample includes stars in *Gaia*'s *G*-band magnitude system as faint as $G \approx 21$, which means that it contains samples of stars that have been previously unavailable for kinematic studies. This includes the a large number of white dwarfs (WDs) which, following DR2, revealed that the colour–magnitude diagram (CMD) of WDs has more structure than previously thought and displays a clear bifurcation as well as a crystallization branch (Gaia Collaboration 2018b, Tremblay et al. 2019).

Since then, there have been a few different explanations put forward and we will briefly summarize a few here. Shortly after DR2 released, El-Badry, Rix & Weisz (2018) used a cross-match of the 100 pc *Gaia* WD sample with the Montreal White Dwarf Database (MWDD; Dufour et al. 2017) to show that part of the bifurcation could be explained by an initial–final mass ratio (IFMR) that produces a bimodal WD mass distribution with peaks at both $\sim$0.6 and $\sim$0.8 $\mathrm{M}_{\odot}$ if the age distribution in multimodal. The different-mass WDs would populate different cooling tracks and produce the bifurcation. This would not produce a bifurcation in mono-age clusters, however, as massive WDs would cool before young WDs appear on the CMD.

Around the same time, Kilic et al. (2018) used a similar sample and showed that atmospheric composition explains the bifurcation well for 0.6 $\mathrm{M}_{\odot}$ WDs. However, they also conclude that the WD mass distribution is indeed bimodal. They suggest that this bimodality can be explained at least partly through the merger of WD binaries. More recently, Kilic et al. (2020) revisited the 100 pc WD sample and conducted a spectroscopic follow-up survey, thereby being able to constrain the atmospheric composition reliably. They found that the mass distribution of WDs that have H lines as the primary feature of their spectrum (DA WDs) has a sharp peak at 0.59 $\mathrm{M}_{\odot}$ with a broad shoulder, best fitted with a secondary Gaussian at 0.76 $\mathrm{M}_{\odot}$, again demonstrating the existence of a bimodal mass distribution. They test a WD model including mergers and find that it cannot produce a good fit to the observed mass distribution. They also investigate the transverse velocities of WDs, since merger products should appear as massive WDs with larger velocities than those formed from single main-sequence stars. However, the lack of young, massive WDs with large velocities coupled with the model predictions leads them to conclude that mergers are unable to explain the bimodal mass distribution of WDs. Instead, it is shown in Tremblay et al. (2019), Bergeron et al. (2019), and Kilic et al. (2020) that the effects of crystallization are able to create the overabundance of massive WDs in the 0.7–0.9 $\mathrm{M}_{\odot}$ range. In this scenario, the massive WDs that should already have reached the bottom of the WD sequence are subjected to cooling delays (for a detailed explanation of these effects, see e. g. Bauer et al. 2020; Blouin, Daligault & Saumon 2021).

The bifurcation in the WD CMD is well described by atmospheric differences and the bimodal WD mass distribution can arise due to core crystallization and its related effects. We explore a new direction to probe the WD bifurcated sequences using their kinematics, which could provide additional insight into the bifurcation problem. While kinematics could be affected in complex ways by the processes that produce binary merger systems, the second, fainter, sequence of the CMD should have the same velocity dispersion as the brighter sequence if it is caused by mergers or atmospheric composition. Previously, Rowell & Kilic (2019) performed a kinematic study of WDs in DR2 using the method of DB98 to determine the mean velocity and velocity dispersion of the WDs. However, as they only split the WD CMD in M_G their results reflect a mixture of the two sequences and we expand upon this analysis by splitting the WDs across the visible bifurcation and computing the full velocity distributions in addition to velocity moments.

The paper is organized as follows: In Section 2, we briefly present the techniques of DB98 and Dehnen (1998) used to determine the moments and velocity distribution. The WD samples that we have used and how they are selected are presented in Section 3. Then, in Section 4 we present the moments for the bimodal sequences and in Section 5 the velocity distribution of nearby WDs is presented for the first time. The implication and significance of our results is discussed in Section 6 and our conclusion are in Section 7.

2 THEORY

2.1 Moments of phase space

In Galactic dynamics, we decompose the space velocity into velocity towards the Galactic Centre, *U*, in the direction of rotation, *V*, and, north of the Galactic plane, *W*. Galactic observations, however, use a combination of the line-of-sight velocity, v_r, and the combined on-sky velocity, $\boldsymbol{p}$. With the release of *Gaia*, we have access to a large sample of stars for which positions (ℓ, b), parallax (ϖ), and proper motions $(\mu_{\ell*}, \mu_b)$ have been measured. A subset of these will also have measurements of radial velocity v_r and with these properties combined one can determine a star's space velocity $\boldsymbol{v}_i$. Without the full 3D velocity vector, we can only know a star's tangential velocity $\boldsymbol{p}_i$. Despite this, it is still possible to determine the moments of phase space, the mean velocity components, and the velocity dispersions, and we do this by making use of a deprojection technique from DB98.

To correct for Galactic rotation, we use equation (1) of DB98 with values for Oort's constants taken from Bovy (2017) ($A = 15.3\,\mathrm{km\,s^{-1}\,kpc^{-1}}$ and $B = -11.9\,\mathrm{km\,s^{-1}\,kpc^{-1}}$). We express the tangential velocity in 3D Galactic coordinates as

$$\boldsymbol{p} = \frac{1}{\varpi}\begin{pmatrix} -\sin\ell\ \mu_{\ell*} - \cos\ell\ \sin b\ \mu_b \\ \cos\ell\ \mu_{\ell*} - \sin\ell\ \sin b\ \mu_b \\ \cos b\ \mu_b \end{pmatrix}, \tag{1}$$

and it is related to the space velocity through the projection

$$\boldsymbol{p} = \mathbf{A}\boldsymbol{v}. \tag{2}$$

The transformation matrix, $\mathbf{A}$, is defined by

$$\mathbf{A} \equiv \mathbf{I} - \hat{\boldsymbol{r}} \cdot \hat{\boldsymbol{r}}^T, \tag{3}$$

where $\mathbf{I}$ is a 3x3 identity matrix and $\hat{\boldsymbol{r}}$ is the unit vector to the star, given by

$$\hat{\boldsymbol{r}} = \begin{pmatrix} \cos b\ \cos\ell \\ \cos b\ \sin\ell \\ \sin b \end{pmatrix}. \tag{4}$$

The symmetric matrix $\mathbf{A}$ is a projection operator and is thus singular and non-invertible, which means that equation (2) cannot be inverted. This comes as no surprise; we cannot determine the space velocity of a star $\boldsymbol{v}$ with its tangential velocity alone.

2.1.1 *Mean velocities*

If the on-sky positions $\hat{\boldsymbol{r}}$ of a sample of stars are uncorrelated with their velocities $\boldsymbol{v}$, then so is the projection matrix. Then, by taking the average of equation (2)

$$\langle \boldsymbol{p} \rangle = \langle \mathbf{A}\boldsymbol{v} \rangle = \langle \mathbf{A} \rangle \langle \boldsymbol{v} \rangle, \tag{5}$$

the matrix $\langle \mathbf{A} \rangle$ *can* be inverted, which means that the average space velocity can be determined from the average tangential velocity

$$\langle \boldsymbol{v} \rangle = \langle \mathbf{A} \rangle^{-1} \langle \boldsymbol{p} \rangle. \tag{6}$$

The assumption of uncorrelated positions and velocities holds under the approximation that the velocity distribution is constant over the volume in question.

2.1.2 *Velocity dispersions*

We can now calculate the motion relative to the mean, known as the peculiar velocity

$$\boldsymbol{p}' \equiv \boldsymbol{p} - \mathbf{A}\langle \boldsymbol{v} \rangle, \qquad \boldsymbol{v}' \equiv \boldsymbol{v} - \langle \boldsymbol{v} \rangle, \tag{7}$$

which allows us to determine the following 3 x 3 matrix

$$\mathbf{B} = \langle \boldsymbol{p}' \boldsymbol{p}'^{T} \rangle = \frac{1}{N} \sum_{i=1}^{N} \boldsymbol{p}'_i \boldsymbol{p}'^{T}_i. \tag{8}$$

In a similar manner to how we could reconstruct $\langle \boldsymbol{v} \rangle$ from $\langle \boldsymbol{p} \rangle$, we can estimate the dispersion tensor $\mathbf{D}$ from the matrix $\mathbf{B}$.

Combining equation (7) with equation (2) and writing it in component form, using Einstein summation convention gives

$$p'_k = \mathbf{A}_{km} v'_m. \tag{9}$$

This allows us to specify the different components of $\mathbf{B}$ as

$$B_{kl} = \langle p'_k p'_l \rangle = \langle A_{km} v'_m A_{ln} v'_n \rangle = \langle A_{km} A_{ln} \rangle \langle v'_m v'_n \rangle, \tag{10}$$

where in the final step we again use the assumption of independence. We get the elements of the dispersion matrix as $D_{mn} = \langle v'_m v'_n \rangle$ and can simply write

$$B_{kl} = \langle A_{km} A_{ln} \rangle D_{mn}. \tag{11}$$

This can be inverted to find the elements of the dispersion tensor that correspond to the second-order moment $(D_{11}, D_{22}, D_{33}) = (\sigma_U^2, \sigma_V^2, \sigma_W^2)$.

This approach is very similar to that of DB98, with the only difference being that here the sample is not assumed to be perfectly isotropic. This method has seen use in, e.g., Rowell & Kilic (2019) for a similar sample of stars to ours.

2.2 Inferring velocity distributions

Just as we were able to determine the mean velocity and velocity dispersions from the tangential projection of the space velocities, we can infer the velocity distribution of a sample of stars without known radial velocities under the approximation that distribution is consistent for the whole sample and is spread across the sky. This method of finding $f(\boldsymbol{v})$ was demonstrated already by Dehnen (1998) for *Hipparcos* stars. Since we use the same method, we will outline only key details here. Consider now the probability distribution of tangential velocities in a given direction $\hat{\boldsymbol{r}}$ as $\rho(\boldsymbol{q}|\hat{\boldsymbol{r}})$ and express it in terms of the full velocity distribution with the integral

$$\rho(\boldsymbol{q}|\hat{\boldsymbol{r}}) = \int \mathrm{d}v_{\mathrm{r}}\, f(\boldsymbol{v}) = \int \mathrm{d}v_{\mathrm{r}}\, f(\boldsymbol{p} + v_{\mathrm{r}}\hat{\boldsymbol{r}}). \tag{12}$$

An estimate of the true distribution $f_0(\boldsymbol{v})$ is the result of maximizing the log-likelihood for a given model of it, $f(\boldsymbol{v})$

$$\mathcal{L}(f) = N^{-1} \sum_{k=1}^{N} \ln P(\boldsymbol{q}_k|\hat{\boldsymbol{r}}_k, f), \tag{13}$$

where

$$P(\boldsymbol{q}_k|\hat{\boldsymbol{r}}_k, f) = \int \mathrm{d}v_{\mathrm{r}}\, f(\boldsymbol{p}_k + v_{\mathrm{r}}\hat{\boldsymbol{r}}_k) \tag{14}$$

is the probability for a star k, in direction $\hat{\boldsymbol{r}}_k$ and with velocity drawn from $f(\boldsymbol{v})$, to be observed with tangential velocity $\boldsymbol{p}_k$. In principle, this log-likelihood could be maximized with a distribution function that has a series of delta functions, one for each star. We therefore introduce a penalty function to enforce smoothness. This function is given a weight α that acts as a smoothing parameter.

$$\mathcal{Q}_\alpha(f) = \mathcal{L}(f) - \frac{1}{2}\alpha \mathcal{S}(f), \tag{15}$$

where $\mathcal{S}(f)$ is the penalty function and a measure of the smoothness of $f(\boldsymbol{v})$. There are two constraints to the function that maximizes $\mathcal{Q}_\alpha(f)$: It must be non-negative,

$$f(\boldsymbol{v}) \geq 0, \tag{16}$$

and it must be unity,

$$\mathcal{N}(f) \equiv \int \mathrm{d}^3\boldsymbol{v}\, f(\boldsymbol{v}) = 1. \tag{17}$$

As is shown in Dehnen (1998), we can meet these conditions in rather elegant ways. The condition of equation (17) is met by maximizing

$$\tilde{\mathcal{Q}}_\alpha(f) \equiv \mathcal{Q}_\alpha(f) - \mathcal{N}(f), \tag{18}$$

instead of $\mathcal{Q}_\alpha(f)$, and the condition of equation (16) is met by defining

$$f(\boldsymbol{v}) \equiv e^{\phi(\boldsymbol{v})}, \tag{19}$$

with $\tilde{\mathcal{Q}}_\alpha$ now a function of $\phi(\boldsymbol{v})$.

The numerical approach to the problem is as follows: View $\phi(\boldsymbol{v})$ on a 3D grid that has $L_U \times L_V \times L_W$ cells and widths of $h_U \times h_V \times h_W$. With each cell denoted by $\boldsymbol{l}$ comprising three integers that label the cell, we then write

$$\phi(\boldsymbol{v}) = \sum_{\boldsymbol{l}} \phi_{\boldsymbol{l}} W_{\boldsymbol{l}}(\boldsymbol{v}), \tag{20}$$

where $W_{\boldsymbol{l}}(\boldsymbol{v})$ is the window function

$$W_{\boldsymbol{l}}(\boldsymbol{v}) = \begin{cases} \frac{1}{h_U h_V h_W}, & \text{if } \forall i\, |v_i - l_i h_i - v_i^0| \leq \frac{1}{2}h_i,\ v_i \in \{U, V, W\} \\ 0, & \text{otherwise,} \end{cases} \tag{21}$$

where $\boldsymbol{v}_i^0$ is the velocity at the centre of the first cell [$\boldsymbol{l} = (0, 0, 0)$], meaning all cells' positions are relative to it in $\boldsymbol{v}$-space. This criterion simply means that the window function is zero if the velocity components do not fit into the grid cell in question. Combining equations (20) and (14), we have

$$P(\boldsymbol{q}_k|\hat{\boldsymbol{r}}_k, f) = \sum_{\boldsymbol{l}} e^{\phi_{\boldsymbol{l}}} K(k|\boldsymbol{l}), \tag{22}$$

where $K(k|\boldsymbol{l})$ is simply the length of the segment of the line $\boldsymbol{v} = \boldsymbol{p}_k + v_r\hat{\boldsymbol{r}}_k$ that lies in cell $\boldsymbol{l}$, divided by $(h_U h_V h_W)$. The penalty function is approximated as

$$\mathscr{S}(f) \simeq \int \mathrm{d}^3\boldsymbol{v} \left(\sum_{\boldsymbol{n}} \phi_{\boldsymbol{n}}\, \Xi_{\boldsymbol{nl}}\right)^2, \tag{23}$$

where

$$\Xi_{\boldsymbol{nl}} = \sum_{i=x,y,z} \frac{\tilde{\sigma}_i^2}{h_i^2}(-2\delta_{\boldsymbol{n},\boldsymbol{l}} + \delta_{\boldsymbol{n},\boldsymbol{l}+\hat{\boldsymbol{e}}_i} + \delta_{\boldsymbol{n},\boldsymbol{l}-\hat{\boldsymbol{e}}_i}). \tag{24}$$

Here, $\hat{\boldsymbol{e}}_i$ denotes the unit vector in the ith direction. Putting it all together gives us the numerical approximation to the function we seek to maximize:

$$\begin{aligned}\tilde{\mathscr{Q}}_\alpha(\boldsymbol{\phi}) = N^{-1}\sum_k \ln\left[\sum_{\boldsymbol{l}} e^{\phi_{\boldsymbol{l}}}\, K(k|\boldsymbol{l})\right] - \sum_{\boldsymbol{l}} e^{\phi_{\boldsymbol{l}}} \\ -\frac{1}{2}\alpha h_x h_y h_z \sum_{\boldsymbol{l}}\left(\sum_{\boldsymbol{n}} \boldsymbol{\phi}_{\boldsymbol{n}}\, \Xi_{\boldsymbol{nl}}\right)^2.\end{aligned} \tag{25}$$

2.2.1 *Maximizing the likelihood*

In order to maximize the value of equation (25), we make use of the conjugate gradient method (e.g. Press et al. 2002). The value of the smoothing parameter α in equation (25) determines the balance between goodness of fit and smoothness. In order to determine an appropriate value, we use the *Gaia* Radial Velocity Spectrometer (RVS) sample. We create two subsamples by randomly selecting 130 000/30 000 sources (to match our `all_500` and `red_500`/`blue_500` sample sizes) and maximize the likelihood with a range of α values to determine the optimal value given a different number of sources. Since the actual velocity distribution can be determined for the RVS sample, we can determine an appropriate α by visual inspection. We find that the values $\alpha = 10^{-11}$ and $\alpha = 3 \times 10^{-11}$ appropriately reconstruct the velocity distribution and use these for our WD and red/blue samples, respectively.

We reduce the number of operations required considerably by using an approach with an increasing grid size. This method uses the initial guess of $\boldsymbol{\phi}$ on a crude Cartesian grid. The solution, $\hat{\boldsymbol{\phi}}$, which maximizes $\tilde{\mathscr{Q}}_\alpha$, is then interpolated on a finer grid and used as the initial guess for a new maximization on that finer grid. We allow for up to six different grids, each grid being twice as big in each dimension. This means the initial grid, $\boldsymbol{n}_{\mathrm{initial}}$, will be of shape $\boldsymbol{n}_{\mathrm{final}}/2^k$, where k is the number of grid steps and is chosen such that no dimension in $\boldsymbol{n}_{\mathrm{initial}}$ is less than 10. For our velocity distributions, we use a grid of $\boldsymbol{n} = [100, 100, 72]$ range. Our velocity distribution is found, following two stages of refinement, on a grid of $\boldsymbol{n} = [100, 100, 72]$ over the range $U \in [-150, 150]$ km s^{-1}, $V \in [-150, 50]$ km s^{-1}, and $W \in [-80, 60]$ km s^{-1}.

Our set-up is broadly consistent with the one used by Dehnen (1998), with a few differences. Our algorithm is built without the original rejection criterion that any star's $K(k|\boldsymbol{l})$ must pass through 96 cells. This means our distributions might take into account stars that lie outside the grid. Instead of discarding these stars, we simply omit the outermost layers of the grid when we present our results to reduce the impact of numerical edge effects. Our choice of grid size and ranges also provides us with a slightly better resolution of $\Delta\boldsymbol{v} \sim [3, 2, 2]$ km s^{-1}.

Since the algorithm itself does not take into account the measured uncertainties of the parameters, we statistically resample every source that we use. To do this, we draw alternative parameters for each source from a multivariate Gaussian in $\mu_{\alpha*}$, μ_δ, and ϖ, with the measured values as means and the uncertainty and correlation coefficients in the covariance matrix. We ignore the uncertainties on RA and Dec. as they are negligible. By comparing the inferred velocity distribution of these resamples with the original sample, we can estimate how significant the observed features are. We find no significant deviations from the initial sample. One example using a resampled distribution can be seen in Appendix C.

3 SAMPLE SELECTION

We use the data from *Gaia* EDR3 (Gaia Collaboration 2021a) and select a solar neighbourhood sample as this allows us to approximate the velocity distribution as constant across the sample, which is required for the analysis. To achieve this, we set a minimum parallax of 2 mas. We apply several quality filters to select a good sample. The renormalized unit weight error (RUWE) described in Lindegren (2018) is a goodness-of-fit statistic; we require that it is less than 1.15 based on an inspection of the distribution of values in an unfiltered sample and of the CMD. The corrected flux excess in *Gaia* magnitude bands BP and RP, C^*, is calculated following the procedure laid out in Riello et al. (2021) as part of our Astronomical Data Query Language (ADQL) query into the column `excess_flux` (the full query can be seen in Appendix A). We use their selection criterion and require that

$$|\mathrm{excess\_flux}| < 3|c_0 + c_1 G^m|, \tag{26}$$

where $c_0 = 0.005\,989\,8$, $c_1 = 8.817\,481 \times 10^{-12}$, and $m = 7.618\,399$.

We create the WD sample by setting $M_g > 9.6 + 3.7(G_{\mathrm{BP}} - G_{\mathrm{RP}})$. As an additional test, we compare our WD sample to that of Gentile Fusillo et al. (2021) and find that 99.5 per cent of our WDs are available within their catalogue. In their paper, they calculate the probability that each source is a WD, P_{WD}, and we find that of the cross-matched sample 98 per cent of stars have $P_{\mathrm{WD}} > 0.9$, indicating a high degree of confidence that our sources are WDs.

The WDs are split along the bimodal sequences along a line selected by eye into an upper and lower sequence (hereafter referred to as the red and blue sequences). We limit these cuts to $12 \lesssim M_G \lesssim 14$, where the bifurcation is clearest. All samples and the number of sources in them are listed in Table 1. To ensure that we are robust to the specific choice of line, we shift the line ±0.05 mag in colour, creating two different versions of the red and blue samples. We find that our results do not change when we shift the line. For WDs with $d < 100$ pc we show the red and blue sequences on top of the CMD in Fig. 1.

Table 1. The names of the various samples used and the number of sources in them.

Name	N_{WD}	Description
`all_500`	129 675	WDs with $d < 500$ pc
`all_200`	54 330	WDs with $d < 200$ pc
`all_100`	14 985	WDs with $d < 100$ pc
`red_500`	32 640	Red seq. WDs with $d < 500$ pc
`red_200`	19 883	Red seq.WDs with $d < 200$ pc
`red_100`	2909	Red seq. WDs with $d < 100$ pc
`blue_500`	27 809	Blue seq. WDs with $d < 500$ pc
`blue_200`	18 653	Blue seq. WDs with $d < 200$ pc
`blue_100`	2842	Blue seq. WDs with $d < 100$ pc
`A`	43 225	WDs with 7.4 mag $< M_G <$ 11.9 mag
`B`	43 225	WDs with 11.9 mag $< M_G <$ 13.3 mag
`C`	43 225	WDs with 13.3 mag $< M_G <$ 18.3 mag

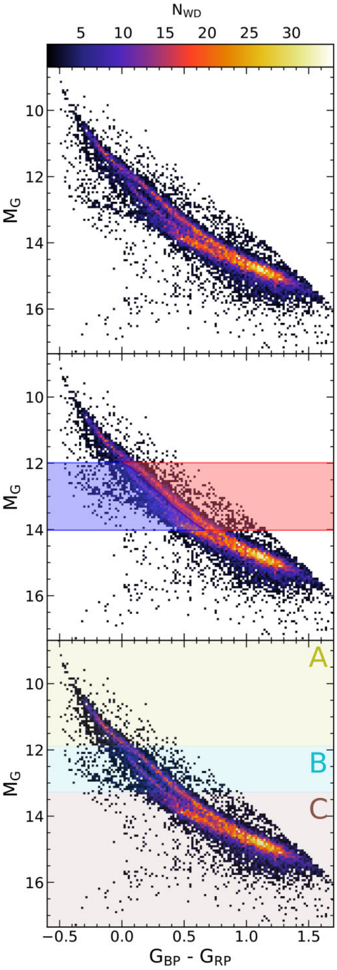

Figure 1. Top: CMD for the WDs within 100 pc. The colour shows the density of WDs on a 150 × 150 grid. Middle: the red and blue selections used to split across the bifurcation. The vertices of the two regions can be seen in Appendix B. Bottom: three different bins in absolute magnitude shown on top of the CMD.

Our selection includes WDs at distances up to ∼500 pc. In *Gaia*, the nominal brightness limit is $G = 20.7$ (Gaia Collaboration 2021a), which in an ideal case would allow *Gaia* to detect sources as faint as $M_G = 15.7$ within 100 pc and $M_G = 14.2$ within 200 pc. In addition to this, we place a parallax uncertainty criterion of $\varpi/\sigma_\varpi > 10$, which means that at 100 and 200 pc the uncertainties must be smaller than 1 and 0.5 mas, respectively. In *Gaia*, the typical parallax uncertainty at $G = 20.7$ for five-parameter solutions is 1.3 mas (Gaia Collaboration 2021a). The brightness and uncertainty limits mean that beyond 100 pc we will start to be affected by incompleteness, and therefore Malmquist bias. Conversely, our samples within 100 pc are free of this bias, especially the red and blue samples, which only go as faint as $M_G = 14$. We also use two WD samples limited in distance to 200 and 500 pc, which are limited by this bias. The effect of the bias will not be exactly the same for the two sequences as the blue sequence is slightly fainter than the red. However, the shift in magnitude between the sequences is sufficiently small that we can neglect it and assume they share the same bias. This means that any difference we see between the two sequences is not be due to the Malmquist bias as it affects the sequences in effectively the same way. A two-sample Kolmogorov–Smirnov (KS) test on the velocity dispersion of the samples between 0 and 100 pc and between 100 and 200 pc shows that these are drawn from the same population, so we can be confident that Malmquist bias has not had a significant effect on our sample out to 200 pc (see the following).

We also split the sample into three bins in absolute magnitude. These bins are chosen such that they have an equal number of WDs from the `all_500` sample. The bins are illustrated in Fig. 1, labelled `A`, `B`, and `C`, and represent a brighter, intermediate, and faint selection of WDs, respectively. As the WDs grow older, they will cool and become fainter, so by looking at different magnitudes we should be able to detect age-dependent variation in the velocity distribution.

4 VELOCITY DISPERSION

In Section 2.1, we showed how we can calculate the velocity dispersion of a sample of stars using only their positions and tangential velocities. We calculate 3D velocity dispersions for a moving window in absolute magnitude separately for the WD samples limited to 100 and 200 pc. We estimate the uncertainty within the windowed sample by calculating the moments for 500 bootstrapped samples. The standard deviation of all of the resulting statistics is used to provide a 1σ uncertainty. The complete 100 pc sample's velocity dispersions are seen in Fig. 2a. Generally, we would expect the velocity dispersion to increase with fainter magnitude due to dynamical heating over time. This is true overall, though the component σ_V is approximately constant for the red and black sequences over the range of magnitudes considered.

The red sequence has a larger velocity dispersion than the blue at low magnitudes in all directions to the extent that their 1σ regions do not overlap. Beyond this, the separation is not as great and harder to make out. In both U and V, the median places the red sequence above the blue. For a comparison, we look also at the velocity dispersion for all the WDs within 200 pc in panel (b), in which the separation is very clear at all magnitudes and for all three velocity components. The 1σ regions of the red and blue barely overlap with the joint sample. To determine whether or not the two distance-limited samples probe the same underlying distribution, we calculate the statistic

$$Q = \frac{\sigma_{\mathrm{A}} - \sigma_{\mathrm{B}}}{\sqrt{\Delta\sigma_{\mathrm{A}}^2 + \Delta\sigma_{\mathrm{B}}^2}}, \tag{27}$$

where $\sigma_{\mathrm{A,B}}$ is the velocity dispersion for samples A or B and $\Delta\sigma_{\mathrm{A,B}}$ their uncertainties estimated through bootstrapping. We calculate Q for both sequences with A being the 100 pc limited samples and B selected to be the stars between 100 and 200 pc to avoid overlapping sources. We calculate Q for a number of binned points in M_G and if the two distance-limited samples are drawn from similar underlying distributions the distribution of Q should be Gaussian, with $\mu = 0$ and $\sigma = 1$. The cumulative distribution of Q can be seen in Fig. 3

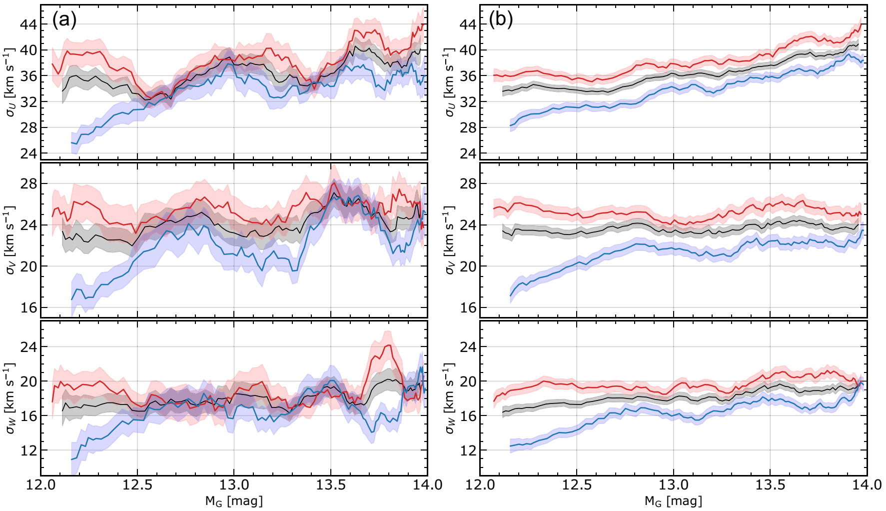

Figure 2. (a) Dispersions in U, V, and W calculated for samples `all_100`, `red_100`, and `blue_100` using a moving window in absolute magnitude and shown with black, red, and blue colours, respectively. The shaded region shows the 1σ uncertainty. The red and blue lines appear to be separate for brighter WDs in all three directions but become mixed towards the fainter end of the sequence. (b) Same as (a) but for the samples `all_200`, `red_200`, and `blue_200`. For these WDs, the split between the red and the blue sequences is much more pronounced and now clearly so at all absolute magnitudes. The red sequence appears to have a larger velocity dispersion in all directions and at almost all absolute magnitudes.

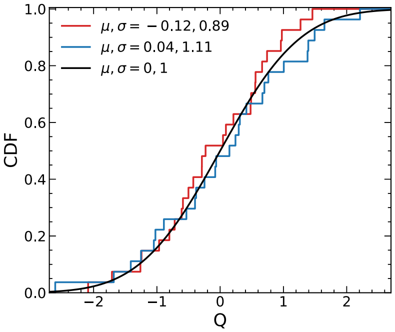

Figure 3. Cumulative distribution of the Q statistic described in the text for the red and blue sequences when comparing samples limited to within 100 pc or between 100 and 200 pc. The black line shows the Gaussian CDF with $\mu = 0$ and $\sigma = 1$.

for the red and blue sequences and shows good alignment with the analytical Gaussian Cumulative Distribution Function (CDF). In addition to this, we perform a KS test between the different samples and the Gaussian CDF under the null hypothesis that they arise from the same distribution. The KS testing yields a P-value of 0.936, 0.834, and 0.936 when testing the red/blue, red/Gaussian, and blue/Gaussian Q distributions, respectively, clearly demonstrating that they arise from the same Gaussian distribution and therefore the difference between our two samples is simply due to statistical noise. In summary, there is a statistically significant separation in the velocity dispersion between the red and blue sequences.

If the bifurcation is caused by a bimodal WD mass distribution, this could be explained by the progenitors of the WDs in the two different sequences. The lower mass WDs will come from less massive main-sequence stars, which would mean that these progenitors will have been dynamically heated for a longer duration of time and the lower mass WDs would be born with larger dispersions.

The separation between red and blue sequences is larger at brighter magnitudes, which correspond to younger WDs. This can be expected if the blue sequence comes from massive WDs that are younger than their red-sequence, less massive, counterparts. Most of the dynamical heating occurs during the first few Gyr of a stars life (e.g. Nordström et al. 2004; Binney & Tremaine 2008) and so would already have occurred for the red-sequence WDs but still be occurring for the blue-sequence ones. Over time as WDs on both sequences cool to fainter magnitudes, their heating tracks would align to become more parallel, which is visible in our figures.

Undeniably, the bifurcation in the CMD is well described by a difference in the atmospheric composition of WDs (Bédard et al. 2021). It is however difficult to reconcile with the observed difference in the kinematics that we display here, which requires significantly different dynamical heating histories between the two sequences. If there is a significant age difference between the two populations, however, this would result from the expected heating from the Galactic disc. We can estimate the age difference of stars in the two sequences using the age–velocity dispersion relationship from

Aumer & Binney (2009) and applying it to the total velocity dispersion of the two samples, `red_500` and `blue_500`. This suggests a typical age of ∼7.7 Gyr and ∼4.9 Gyr respectively for the red and blue sequences. We are unaware of any mechanism that could explain these kinematics purely by a difference in atmospheric composition.

As mentioned in Section 3, we also selected WDs out to $\varpi = 2$ mas or 500 pc. Beyond 200 pc, the separation between red and blue sequences remains the same and did not provide any further insights.

5 VELOCITY DISTRIBUTION OF WHITE DWARFS

We apply the maximum penalized likelihood estimate to all of the samples to produce a full 3D velocity distribution for which we show the projections in the planes U–V, U–W, and V–W. To identify where the peaks of the distribution are, we apply the peak_local_max function available as part of the SCIKIT-IMAGE[1] PYTHON package (van der Walt et al. 2014). The results in the U–V plane are presented first in Fig. 4. In the first row, we compare the velocity distribution of all our WDs with those of WDs identified as belonging to the red and blue sequences as laid out in Section 3. It is immediately clear that the WD velocity distribution is overall very similar to the rest of the solar neighbourhood (e.g. Gaia Collaboration 2018c), which is not too surprising considering that the WDs are older stars of the same population.

We can identify a few familiar moving groups such as the Hyades, Pleiades, and Hercules across all three samples very clearly. To a lesser extent, we can also identify higher velocity moving groups beyond $U > 25\,\mathrm{km\,s^{-1}}$ such as Wolf 630 and Dehnen98.The moving groups in the blue sequence are more narrowly distributed around their group mean overall than those of the red sequence, where the groups are spread out more across the central regions in the space due to the overall larger velocity dispersion shown in Section 4.

We show the three samples of different absolute magnitudes in the second row of Fig. 4, going from brightest (`A`) to faintest (`B`). For the individual distributions, we see the same type of structure as we did for the whole sample. It appears as though there is more structure in these subsamples than in the former three. However, as the samples contain less stars than the `all_100` sample but use the same smoothing parameter α they have a noisier distribution. The fainter sample, `C`, has older stars and thus a larger velocity dispersion, as expected, which 'smears' out the distribution, which reveals an arch-like structure in `C`, with three horizontal arches at V of 0, −20, and $-40\,\mathrm{km\,s^{-1}}$, which are illustrated in the plot. This type of structure has been shown to exist in the solar neighbourhood (Gaia Collaboration 2018c) and can be attributed to dynamical resonances with the spiral arms and Galactic bar (Trick et al. 2019).

The third row takes the three samples `A`, `B`, and `C`, and subtracts the mean of all three to emphasize the parts of the distribution that are shared between the samples or are independently significant. Our expectation is that the bright, young sample with low velocity dispersion (`A`) should be overabundant near the centre of the distribution and the faint sample should show the opposite. Stars with very large $|V|$ belong to populations with their guiding centres at significantly larger/smaller Galactocentric radii and would be visiting the solar neighbourhood when their orbits are sufficiently dynamically heated. Thus, they would be older and part of a fainter sample. This effect can be seen in the third row, where samples `A` and `B` dominate the centre of the distribution while `C` is represented more in the wings with, for example, the Hercules moving groups being overabundant. Asymmetric drift also causes the mode of the distribution to shift towards more negative V.

The region around $(U,\ V) \approx (7,\ -19)\,\mathrm{km\,s^{-1}}$ is underdense in `A` and `B` but surprisingly is overabundant in `C`, with an identified peak in that region as well. A review of recent articles that investigate the velocity distribution in $U-V$ for the solar neighbourhood reveals that Antoja et al. (2012) and Gaia Collaboration (2018c) do not identify a known moving group in this region, while Kushniruk et al. (2017) does and attributes it to the Coma Berenices stream.

The distributions in $U-W$ and $V-W$ in Figs 5 and 6 are not as rich in structure as the $U-V$ plane, but we can, however, identify Coma Berenices and Pleiades by comparing the two planes. Our choice of smoothing parameter α is chosen to fit best with the sample `all_500` and hence will be underestimated for the smaller samples (`red_500` and `blue_500`) and as such the features seen in them may disappear with an α that is appropriate for smaller samples. A feature identified by Dehnen (1998) is a double-peaked feature along W in the $U-W$ plane at $U \approx -30\,\mathrm{km\,s^{-1}}$ and in the $V-W$ plane at $V \approx -20\,\mathrm{km\,s^{-1}}$. This double-peaked feature is very vaguely present in $U-W$ for sample `C`. In the $V-W$ plane, however, we can identify the feature clearly in both `red_500` and `blue_500`, and perhaps vaguely in `B` and `C`. We mark the proposed double-peak feature with circles around the involved features. This seems to imply that the double-peaked feature, of which the Pleiades appears a part, is limited to fainter, possibly older stars.

In Table 2, we summarize the features we can see and mark whether we can see them clearly, somewhat, or not at all. We also list their locations in all three velocity dimensions (see for comparison table 2 from Dehnen 1998). For most of the moving groups, we are able to associate a previously known one following Kushniruk et al. (2017), but no known group accurately describes feature 5 in the table, meaning that it may be a new feature. Compared with previous results, the features presented here are located mostly at lower velocities ($|v| < 50\,\mathrm{km\,s^{-1}}$). It may be that the WDs in groups at larger velocities are not numerous enough to appear in the distributions or that their dispersion is too great.

5.1 The stellar warp

In his analysis of *Hipparcos* data, Dehnen (1998) found evidence for the stellar warp by investigating $\langle W\rangle$ as a function of V. For $V > 10\,\mathrm{km\,s^{-1}}$, the velocity distribution was skewed towards positive $\langle W\rangle$. We perform the same analysis here of our largest WD sample `all_500` and the results can be seen in Fig. 7. To do this, we require a larger grid of $\boldsymbol{n} = [200, 152, 152]$ covering $U \in [-200, 200]\,\mathrm{km\,s^{-1}}$, $V \in [-150, 150]\,\mathrm{km\,s^{-1}}$, and $W \in [-150, 150]\,\mathrm{km\,s^{-1}}$ to ensure that none of the edge effects discussed in Section 2.2.1 affect the results. We find that our results also show increasing $\langle W\rangle$ with increasing V.

We compare our results to Schönrich & Dehnen (2018), who use the Tycho-Gaia Astrometric Solution (TGAS) to determine the average vertical velocity as a function of azimuthal velocity and angular momentum for stars in the two cones towards the Galactic Centre and anti-Centre with angular radius of 30° (their fig. 6). Since our samples are in the solar neighbourhood, the velocity in V is a proxy for angular momentum since $L_z = -R(V_\odot + V)$. Just as in our sample, the average vertical velocity increases with angular momentum and shows a dip just beyond the local standard of rest (LSR). At large angular momentum, corresponding to $V > 15\,\mathrm{km\,s^{-1}}$ in the solar neighbourhood, there is a significant increase in $\langle W\rangle$ for all of their samples as well as ours. Towards $V = 50\,\mathrm{km\,s^{-1}}$ $\langle W\rangle$

---

[1] https://scikit-image.org/

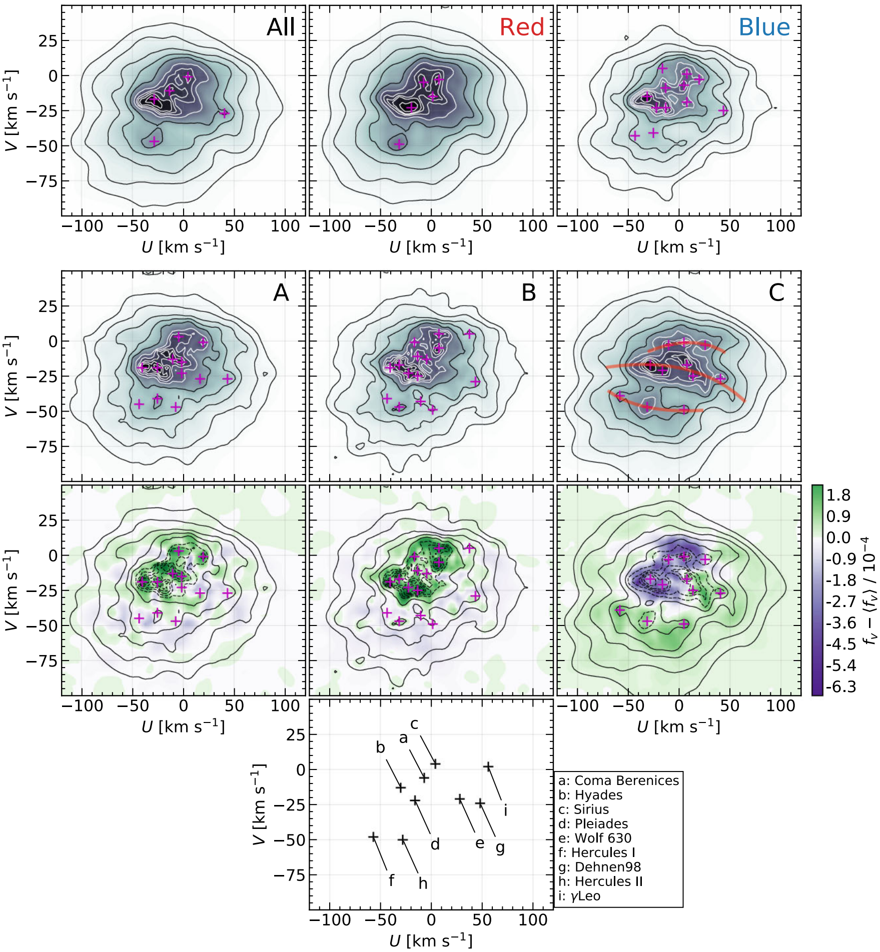

Figure 4. The velocity distribution of WDs in U and V. The top row shows the distribution for the whole WD sequence and the red and blue sequences corresponding to samples `all_500`, `red_500`, and `blue_500` in Table 1. Contour lines are constructed so as to contain 95, 90, 80, 68, 50, 33, 21, 12, 6, and 2 per cent of all sources in the sample and magenta crosses show identified peaks with a peak-finding algorithm described in Section 5. The second row contains samples `A, B, and C`, as indicated, which are magnitude bins in the full sample. Three horizontal arches are illustrated in sample `C` and explained in Section 5. The third row takes the distributions for the three samples `A, B, and C` and subtracts the mean of all three samples. The contour lines are the same as the individual distributions. The fourth row shows the first nine groups identified in Antoja et al. (2012) as black crosses for comparison.

decreases again, which is consistent with a similar decrease at higher angular momentum seen by Schönrich & Dehnen (2018).

More recently, the Gaia Collaboration (2021b) also looked at the vertical velocity profile of stars outside the solar radius as a function of angular momentum. We see this in their fig. 11, which shows this profile for several different stellar types, of which the young main-sequence stars are the ones to show a decrease in vertical velocity at $L_z^* \sim 2400\,\mathrm{kpc\,km\,s^{-1}}$ corresponding to around $V = 60\,\mathrm{km\,s^{-1}}$. However, our sample and the *Gaia* TGAS sample are in the solar neighbourhood, where stars with such large angular momentum must have large radial excursions to be included in the sample, and therefore are very likely to be old. This is in contrast to the stars in

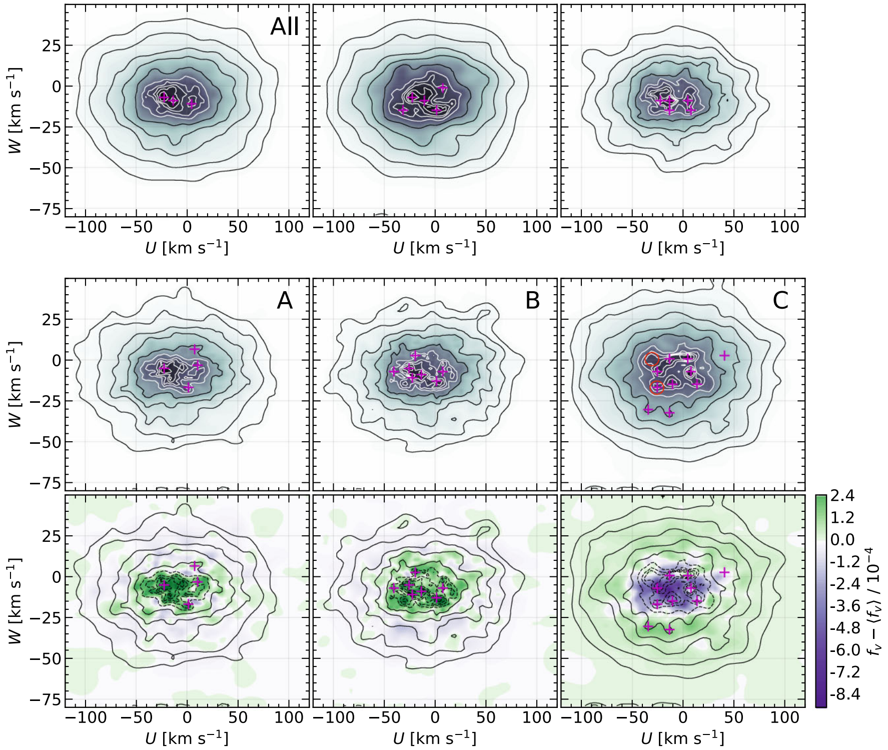

Figure 5. Same as Fig. 4 but in U and W. The circles in panel C mark the peaks that are suggested to be part of a double-peaked feature discussed in Section 5.

the Gaia Collaboration (2021b), which are young and located beyond 10 kpc from the Galactic Centre. While the decrease in the vertical velocity profile we see could therefore be related to these decreases seen in other data sets, we note that the decrease is still within 1σ uncertainty, and therefore, the most we can say is that the results are mutually consistent.

For $V < 20\,\mathrm{km\,s^{-1}}$, where the Poisson noise is not as great, the average velocity, $\langle W \rangle$, has a relatively small tilt. We perform a weighted linear fit for $V \in [-80, 50]\,\mathrm{km\,s^{-1}}$ and find a slope of $\sim$0.03 (shown in Fig. 7), which is somewhat larger than the $\sim$0.02 found by Schönrich & Dehnen (2018). If we instead restrict our fit to the relatively well-constrained region $V \in [-80, 20]\,\mathrm{km\,s^{-1}}$, we find a slope of $\sim$0.025, in agreement with the previous results.

6 DISCUSSION

6.1 The bifurcated WD CMD

In Section 1, we reviewed the literature on the nature of the bifurcation of the CMD in the *Gaia* data. We know that there exists a bimodality in the mass distribution of spectral class DA WDs (Kilic et al. 2018, 2020; Jiménez-Esteban et al. 2018) at around $\sim 0.6\,\mathrm{M}_\odot$ and $\sim 0.8\,\mathrm{M}_\odot$.

Cooling tracks for these masses of DA WDs would produce a bifurcation that appears very similar to the one visible in *Gaia* (El-Badry et al. 2018). However, massive WDs will form sooner and begin cooling at an earlier time than the less massive ones, which means that for these cooling tracks to be simultaneously visible in the CMD the massive WDs must be (1) formed through the merger of lower mass WD binaries, (2) formed at a later time than the less massive WDs, or (3) cooling slower due to crystallization. Scenario (1) was suggested by Kilic et al. (2018) but subsequently dismissed by Kilic et al. (2020) due to merger models being unable to produce a mass distribution that fit the observations as well as, and, perhaps more importantly, not being able to find a significant amount of young and massive DA WDs with high velocities. This leaves scenarios (2) and (3). In the first of these scenarios, a multimodal age distribution could produce massive WDs at a later time for a bimodal mass distribution that would have a smaller velocity dispersion as they have not had as much time to be heated. In the latter scenario, crystallization (Tremblay et al. 2019) will result in a slowdown of the cooling of massive WDs, which means the massive sequence can

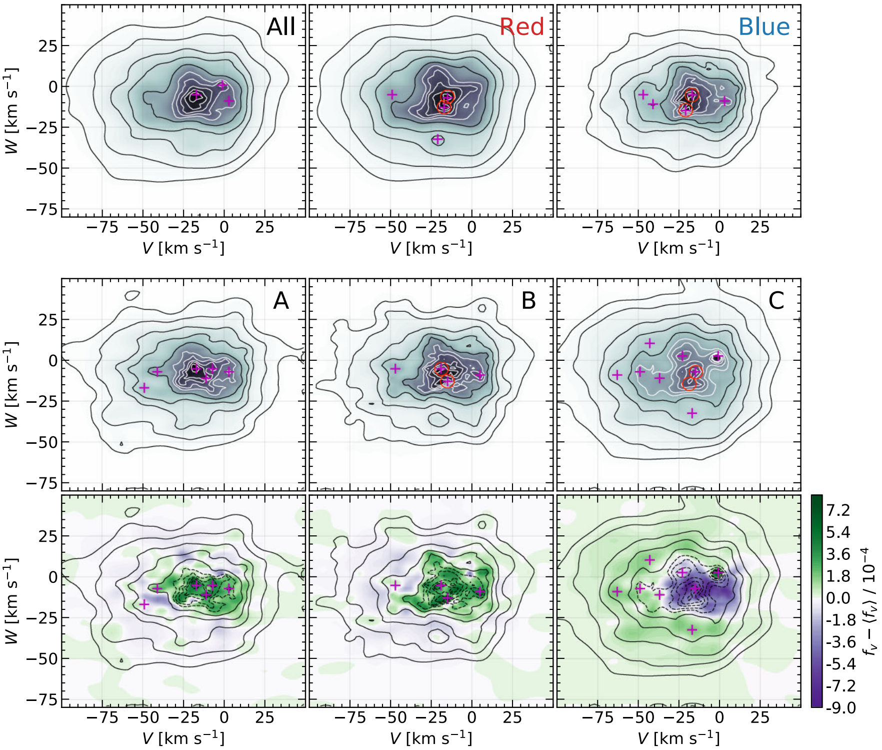

Figure 6. Same as Fig. 5 but in V and W.

Table 2. Identified features in the velocity distributions at approximate coordinates. We omit the velocity in W when it cannot be determined accurately. Filled circles and hollow circles are for clear and weak features, respectively. Group 5 has an asterisk indicating unclear membership in the moving group, which is further discussed in Section 6.2.

Feature	U	V	W	`all_500`	`red_500`	`blue_500`	`A`	`B`	`C`	Moving group
1	4	−1	...	●	●	●		○	●	Sirius
2	−13	−11	−10	●	○	●	●	●		Coma Berenices
3	−28	−17	...	●	○	●	●	●	●	Hyades
4	−28	−47	...	●	●	●	●	●	●	Hercules
5	7	−19	...	○		●			●	Coma Berenices*
6	1	−48	...	○		○	○	○	○	Hercules
7	1	−15	...		●		●		○	Coma Berenices
8	16	−26	...				○		●	Wolf 630
9	−19	−23	−8	○	●	●	●	●	●	Pleiades
10	40	−27	...	●	○	●	●	●	●	Dehnen 98
11	19	−1	...			●	●		○	Sirius
12	−7	−5	...		●				○	Coma Berenices

consist of a mixture of young and older massive WDs. Both of these scenarios would cause the massive WDs to have a lower velocity dispersion. In Fig. 2, it is clear that this behaviour is observed. The velocity distributions for the red and blue sequences in Figs 4, 5, and 6 exhibit this as well, with the red sequence showing a larger velocity dispersion.

Atmospheric composition can elegantly explain the visible bifurcation in the *Gaia* data with an upper DA branch and a lower branch

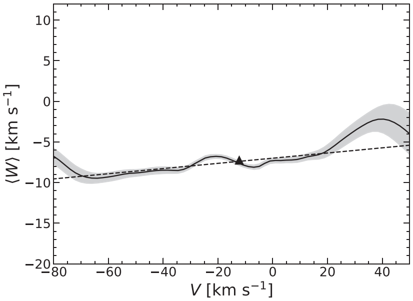

Figure 7. Mean of the vertical motion, $\langle W \rangle$, in the central regions of $f(V, W)$ for sample `all_500`. The location of the LSR is marked by a triangle and is taken from Schönrich, Binney & Dehnen (2010). The error bars show the 1σ Poisson noise. The dashed black line shows a weighted linear fit.

of He-dominated WDs with trace amounts of H or other metals. The bimodal WD mass distribution fits well with this explanation when described by the process of crystallization or by the inclusion of young massive WDs. However, atmospheric composition alone does not provide the difference in kinematics between the two sequences that we identify. This difference arises naturally, however, with a bimodal WD mass distribution from a multimodal age distribution.

The cooling tracks of $\sim$0.6 M$_\odot$ and $\sim$0.8 M$_\odot$ DA WDs would also lie in the region where the bifurcation exists (e.g. Bergeron et al. 2019). We cross-match our `red_100` and `blue_100` with the MWDD to determine what fractions of stars are DA or non-DA and find that around 85 per cent of the red sample cross-match and 39 per cent of the blue sample cross-match are DAs. The red cross-match shows that the this sequence is likely to be comprised of older, less massive DAs. The DAs in the blue cross-match have higher mass with a mean of $\sim$0.8 M$_\odot$ as expected in keeping with previous results (e. g, Kilic et al. 2020).

The bifurcation seen in *Gaia* clearly has contributions from both atmospheric differences and different WD mass cooling tracks. It remains unclear whether the origin of the massive WDs is recent bursts of star formation or a pile-up of WDs with a mixture of ages due to delayed cooling from crystallization, or a mixture of both. Fantin et al. (2019) investigate the star formation history of the Galactic disc using WDs and suggest that star formation increases 3.3 ± 1.8 Gyr ago and is roughly constant for $\sim$5 Gyr prior to that. A detailed study of the age distribution of the WD population using accurately determined ages, masses, and spectral types would provide valuable insight into these questions and analytical modelling of WD formation and evolution following bursts of star formation would be a good avenue to test the formation avenues of these WDs.

6.2 The velocity structure of WDs

For the first time, we present the velocity distribution of WDs in the solar neighbourhood in addition to their velocity moments for such a large sample. We find that the WD velocity distribution in (U, V) shares many features with the velocity distribution of main-sequence stars when comparing our results with recent maps of the kinematic structure of the solar neighbourhood like those of the Gaia Collaboration (2018c), Kushniruk et al. (2017), or Antoja et al. (2012). When we separate our sample along this bifurcation, we can see very similar velocity distributions, with the notable differences being the red sample having a larger velocity dispersion.

The CMD is also split into three equally sized samples based on their absolute magnitude. The mean velocity distribution of all three subsamples is subtracted from each individual subsample, which reveals an unexpected overdensity for the faintest sample, `C`, in the region $(U, V) \approx (7, -19)$ km s^{-1}. The location does not match conclusively to any of the known moving groups and is only identified in Kushniruk et al. (2017), who attribute it to be a part of the Coma Berenices moving group along with two other identified groups. If this feature is limited to fainter, older stars, it could suggest its origin is dynamical. In Monari et al. (2018), it is shown that the Coma Berenices moving group is not vertically phase mixed and is localized to negative b only, and this is suggested to be due to a recent passing by a dwarf galaxy such as Sagittarius, which fits well with passages suggested in the literature (for a summary, see the lower panel of fig. 2 of Ruiz-Lara et al. 2020).

The double-peaked feature identified in W is limited to fainter stars, which should be part of an older sample. The feature is symmetrical around the average vertical velocity, which suggests that this feature might be in the brighter sample as a single feature around the mode containing younger, less dynamically heated stars.

Beyond smaller scale structure, we find that the velocity distribution is very similar to that of main-sequence stars, which can be expected since WDs are subject to the same dynamical processes as other stars. The distributions also show very clear arches like those seen in dynamical studies of main-sequence stars (e.g. Trick et al. 2019). To further narrow down the origin of the observed features requires comparison with model predictions or investigating the ages and abundances of their associated stars. For example, It would be possible to investigate the age evolution of dynamical features in the distributions by studying their appearance for several absolute magnitude bins and associating the absolute magnitude with ages using WD cooling tracks.

7 CONCLUSIONS

We present the velocity distributions of WDs in the solar neighbourhood, which, to our knowledge, has not been done previously. The velocity distributions are estimated through a penalized maximum likelihood. The data we use come from *Gaia* EDR3 and are filtered to select a clean and unbiased sample of WDs. We split the WD CMD across the established bifurcation and into several absolute magnitude bins and find that the velocity distribution is similar to that of main-sequence stars from previous studies and displays many well-known moving groups. We also identify a novel structure located at $(U, V) \approx (7, -19)$ km s^{-1}, which appears only in bins that are fainter or possibly older, and discuss possible explanations for the feature. We also identify a double-peaked feature in W, previously established in the *Hipparcos* data by Dehnen (1998), involving mostly fainter stars.

We also explore the mean velocities and velocity dispersions as a function of absolute magnitude and compare them between the two established sequences in the *Gaia* WD CMD. We find that the brighter sequence has larger velocity dispersion than the faint one across all magnitudes: The sequences are two separate kinematic populations. This cannot be explained if the origin of the second sequence is due to WD binary mergers or solely atmospheric composition. Our results are consistent with the observed WD bimodal mass distribution with a multimodal age distribution.

The results of our study shed light on the bifurcation in the *Gaia* WD CMD and explore the possibility of accessing the majority of sources in *Gaia* that lack radial velocities. We plan to use EDR3 to investigate the velocity distribution of the solar neighbourhood using as many stars as we can include to probe the kinematic structure of the Milky Way for new insights.

ACKNOWLEDGEMENTS

This work made use of data from the European Space Agency (ESA) mission *Gaia* (https://www.cosmos.esa.int/gaia), processed by the *Gaia* Data Processing and Analysis Consortium (DPAC, https://www.cosmos.esa.int/web/gaia/dpac/consortium). Funding for the DPAC has been provided by national institutions, in particular the institutions participating in the *Gaia* Multilateral Agreement. This research made use of ASTROPY,[2] a community-developed core PYTHON package for astronomy (Astropy Collaboration 2013, 2018).

We thank members of the Lund Observatory for helpful comments and ideas. We give special thanks to Ross Church for constructive discussions and comments. Computations for this study were performed on equipment funded by a grant from the Royal Physiographic Society in Lund. PM was supported by project grants from the Swedish Research Council (vetenskaprådet reg: 2017-03721 and 2021-04153). DH and PM gratefully acknowledge support from the Swedish National Space Agency (SNSA Dnr 74/14 and SNSA Dnr 64/17).

DATA AVAILABILITY

All the data analysed in this paper are publicly available from the *Gaia* EDR3 archive (http://gea.esac.esa.int/archive/). The 3D probability distributions used in Figs 4, 5, and 6 are available upon request from the corresponding author.

REFERENCES

Antoja T. et al., 2012, MNRAS, 426, L1
Antoja T. et al., 2018, Nature, 561, 360
Astropy Collaboration, 2013, A&A, 558, A33
Astropy Collaboration, 2018, AJ, 156, 123
Aumer M., Binney J. J., 2009, MNRAS, 397, 1286
Bauer E. B., Schwab J., Bildsten L., Cheng S., 2020, ApJ, 902, 93
Bédard A., Brassard P., Bergeron P., Blouin S., 2021, preprint (arXiv:2112.09989)
Bergeron P., Dufour P., Fontaine G., Coutu S., Blouin S., Genest-Beaulieu C., Bédard A., Rolland B., 2019, ApJ, 876, 67
Binney J., Tremaine S., 2008, Galactic Dynamics, 2nd edn. Princeton Univ. Press, Princeton
Blouin S., Daligault J., Saumon D., 2021, ApJ, 911, L5
Bovy J., 2017, MNRAS, 468, L63
Dehnen W., 1998, AJ, 115, 2384
Dehnen W., Binney J. J., 1998, MNRAS, 298, 387 (DB98)
Dufour P., Blouin S., Coutu S., Fortin-Archambault M., Thibeault C., Bergeron P., Fontaine G., 2017, in Tremblay P. E., Gaensicke B., Marsh T., eds, ASP Conf. Ser. Vol. 509, 20th European White Dwarf Workshop. Astron. Soc. Pac., San Francisco, p. 3
El-Badry K., Rix H.-W., Weisz D. R., 2018, ApJ, 860, L17
Fantin N. J. et al., 2019, ApJ, 887, 148
Gaia Collaboration, 2016, A&A, 595, A1
Gaia Collaboration, 2018a, A&A, 616, A1
Gaia Collaboration, 2018b, A&A, 616, A10
Gaia Collaboration, 2018c, A&A, 616, A11
Gaia Collaboration, 2021a, A&A, 649, A1
Gaia Collaboration, 2021b, A&A, 649, A8
Gentile Fusillo N. P. et al., 2021, MNRAS, 508, 3877
Jiménez-Esteban F. M., Torres S., Rebassa-Mansergas A., Skorobogatov G., Solano E., Cantero C., Rodrigo C., 2018, MNRAS, 480, 4505
Kilic M., Hambly N. C., Bergeron P., Genest-Beaulieu C., Rowell N., 2018, MNRAS, 479, L113
Kilic M., Bergeron P., Kosakowski A., Brown W. R., Agüeros M. A., Blouin S., 2020, ApJ, 898, 84
Kushniruk I., Schirmer T., Bensby T., 2017, A&A, 608, A73
Lindegren L., 2018, Re-normalising the astrometric chi-square in Gaia DR2, GAIA-C3-TN-LU-LL-124. http://www.rssd.esa.int/doc_fetch.php?id = 3757412
Monari G. et al., 2018, RNAAS, 2, 32
Nordström B. et al., 2004, A&A, 418, 989
Perryman M. A. C. et al., 1997, A&A, 500, 501
Press W. H., Teukolsky S. A., Vetterling W. T., Flannery B. P., 2002, Numerical recipes in C+ + : the art of scientific computing,Cambridge University Press, Cambridge, UK
Riello M. et al., 2021, A&A, 649, A3
Rowell N., Kilic M., 2019, MNRAS, 484, 3544
Ruiz-Lara T., Gallart C., Bernard E. J., Cassisi S., 2020, Nat. Astron., 4, 965
Schönrich R., Dehnen W., 2018, MNRAS, 478, 3809
Schönrich R., Binney J., Dehnen W., 2010, MNRAS, 403, 1829
Tremblay P.-E. et al., 2019, Nature, 565, 202
Trick W. H., 2022, MNRAS, 509, 844
Trick W. H., Coronado J., Rix H.-W., 2019, MNRAS, 484, 3291
Trick W. H., Fragkoudi F., Hunt J. A. S., Mackereth J. T., White S. D. M., 2021, MNRAS, 500, 2645
van der Walt S. et al., 2014, PeerJ, 2, e453

---

[2] http://www.astropy.org

APPENDIX A: *GAIA* ARCHIVE QUERY

The following query has been used on the *Gaia* archive[3] and is detailed in Section 3:

```
select bp_rp, phot_g_mean_mag, phot_bp_rp_excess_factor, ra, dec, parallax, pmra, pmdec,
if_then_else(
bp_rp > −20,
to_real(case_condition(
 phot_bp_rp_excess_factor - (1.162004  +  0.011464∗ bp_rp
                +  0.049255∗power(bp_rp,2)
               - 0.005879∗power(bp_rp,3)),
 bp_rp < 0.5,
 phot_bp_rp_excess_factor - (1.154360  +  0.033772∗ bp_rp
                +  0.032277∗power(bp_rp,2)),
 bp_rp > =  4.0,
 phot_bp_rp_excess_factor - (1.057572  +  0.140537∗bp_rp)
)),
phot_bp_rp_excess_factor
) as excess_flux
from gaiaedr3.gaia_source
where parallax > 2
and parallax_over_error > 10
and ruwe < 1.15
```

APPENDIX B: RED AND BLUE WD SEQUENCE SELECTION

Table B1 lists the vertices for the intersect between red and blue regions of the WD CMD outlined in Section 3.

Table B1. Vertices for the regions in M_G and $G_{\mathrm{BP}} - G_{\mathrm{RP}}$ that make up our red and blue WD sequences.

$G_{\mathrm{BP}} - G_{\mathrm{RP}}$ (mag)	M_G (mag)
0.668	14.021
0.561	13.746
0.407	13.291
0.323	12.982
0.231	12.673
0.150	12.364
0.071	12.124
0.001	11.987

---

[3] https://gea.esac.esa.int/archive/

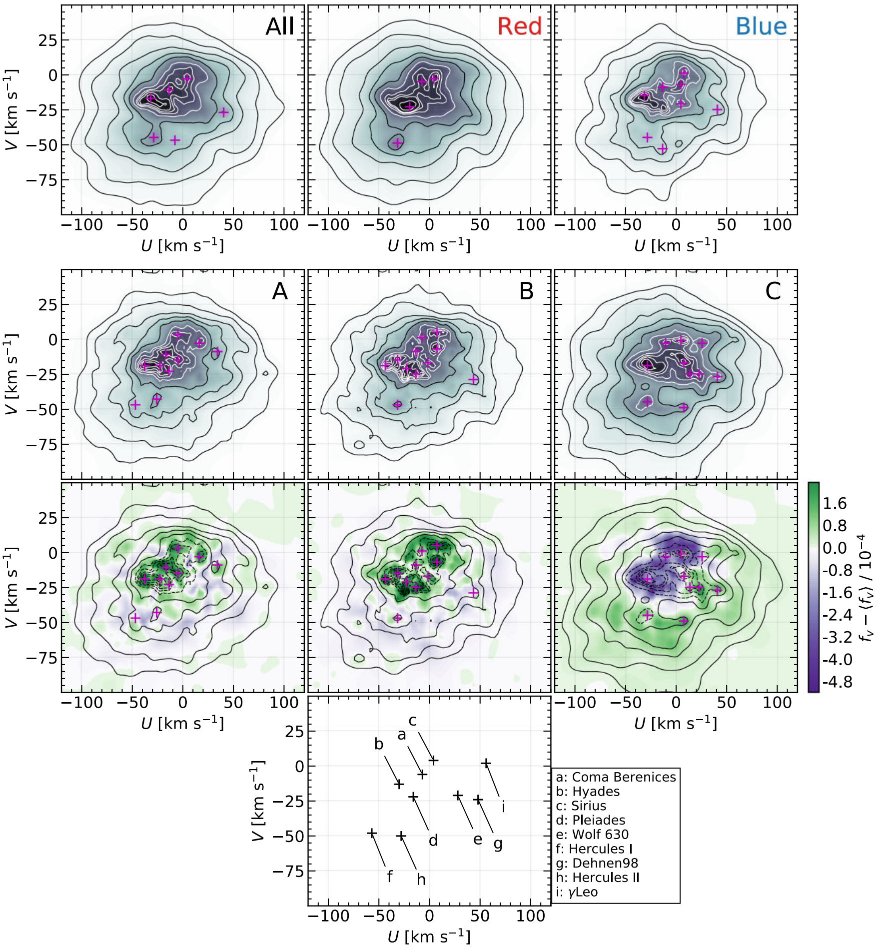

Figure C1. Same as Fig. 4 using a statistical resample of the proper motions and parallaxes.

APPENDIX C: RESAMPLED VELOCITY DISTRIBUTIONS

At the end of Section 2.2, we explained how we used a statistical resample of our proper motions and parallaxes with their measured uncertainties to estimate the effect that the uncertainties might have. As they are not significant, we omit them from the main paper and show a single example of one of these resamples in Figs C1–C3.

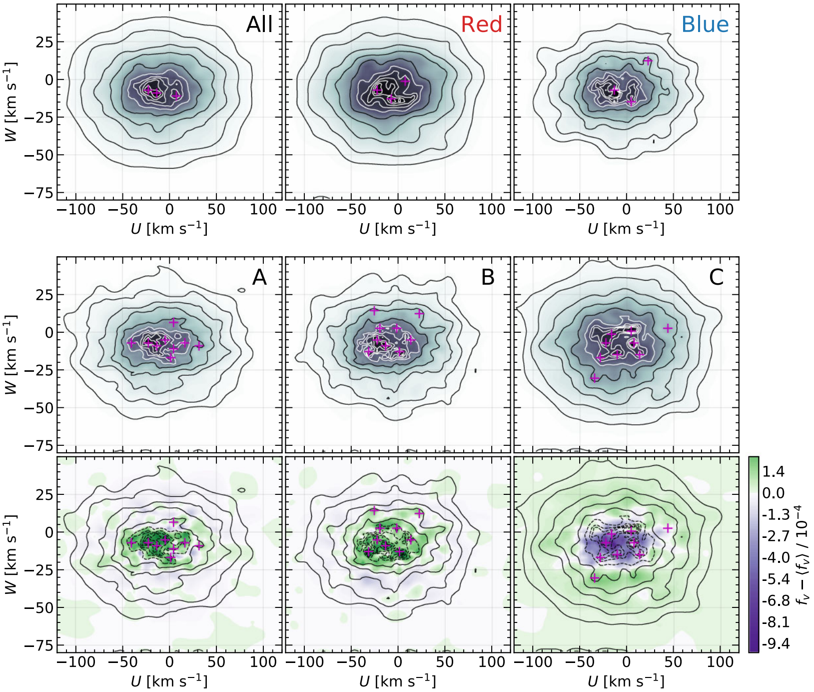

Figure C2. Same as Fig. 5 using a statistical resample of the proper motions and parallaxes.

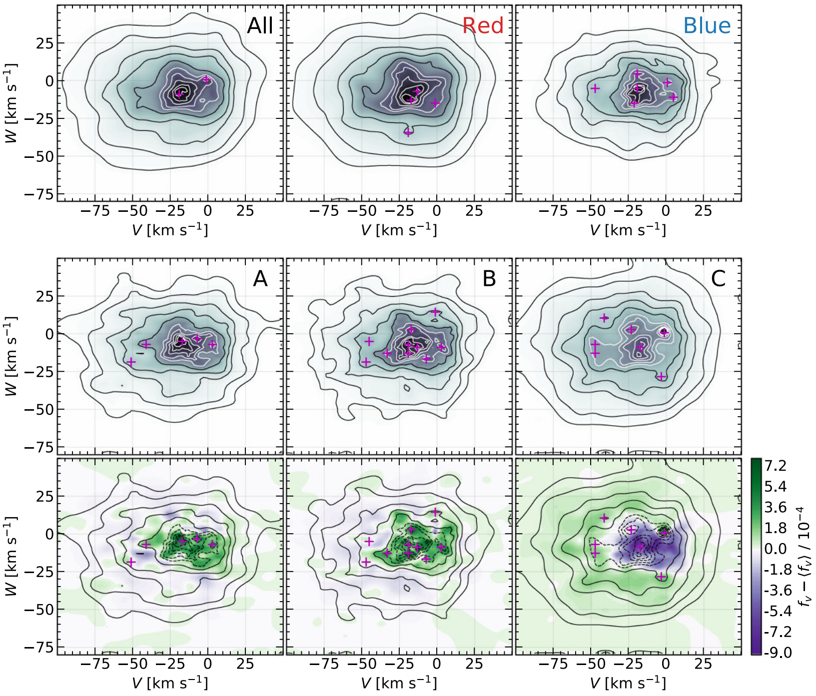

Figure C3. Same as Fig. 6 using a statistical resample of the proper motions and parallaxes.

This paper has been typeset from a TEX/LATEX file prepared by the author.

Paper III

Paper III: New stellar halo substructures from Gaia DR3 proper motions

Mikkola, D.; McMillan, P. J.; Hobbs, D. (submitted to MNRAS)

My contribution:

After the second paper, DM and PM had the original idea to expand the method and apply it to other data sets. DM and PM chose two new data sets which were a large Solar neighbourhood sample and a stellar halo sample. PM provided literature sources for velocity distributions of the stellar halo. DM acquired the data and filtered it for quality. DM implemented conversion into spherical velocity coordinates in the code and ran the algorithm to produce probability distributions. The analysis in velocities was carried out by DM, with support from PM and DH and minor contributions from PM. DM wrote the paper which was reviewed by PM and DH to bring it to a submittable state.

MNRAS **000**, 1–11 (2022) Preprint 5 October 2022 Compiled using MNRAS LaTeX style file v3.0

New stellar halo substructures from Gaia DR3 proper motions

Daniel Mikkola⋆[1], Paul J. McMillan†[1], David Hobbs[1]
[1]*Lund Observatory, Lund University, Department of Astronomy and Theoretical Physics, Box 43, SE-22100, Lund, Sweden*

Accepted XXX. Received YYY; in original form ZZZ

ABSTRACT

Local stellar motions are expected, and have been shown, to include signatures of the Galaxy's past dynamical evolution. These are typically divided into the disc, which shows the dynamical effects of spiral arms and the bar, and the stellar halo, with structures thought to be debris from past mergers. We use *Gaia* Data Release 3 to select large samples of these populations without limiting them to sources with radial velocities. We apply a penalised maximum likelihood method to these samples to determine the full 3D velocity distribution in Cartesian (U, V, W) or spherical (v_r, v_ϕ, v_θ) coordinates. We find that the disc population is dominated by four moving groups and also detect a new moving group at $(U, V) = (-10, -15)$ km s^{-1}. For the stellar halo, we isolate the accreted component with cuts in transverse velocity and the colour-magnitude diagram. In this component we find several known structures believed to be caused by past mergers, particularly one around $(v_r, v_\phi, v_\theta) = (-150, -300, -100)$ km s^{-1} appears more prominent than previously claimed. Furthermore we also identify two new structures near $(v_r, v_\phi, v_\theta) = (\pm225, 25, 325)$ km s^{-1} and $(0, 150, -125)$ km s^{-1} which we refer to as *MMH-1* and *MMH-2* respectively. These results give new insights into local stellar motions and shows the potential of using samples that are not limited to stars with measured line-of-sight velocities, which is key to providing large samples of stars, necessary for future studies.

Key words: methods: statistical - methods: data analysis - Galaxy: structure - Galaxy: Solar neighbourhood - stars: kinematics and dynamics - Galaxy: kinematics and dynamics.

1 INTRODUCTION

As our Galaxy evolves, the kinematics of the stars that reside in it are imprinted by the various external and internal processes that affect it. The volume near the Sun is no different and contains footprints of possible dynamical resonances and interactions with nearby dwarf galaxies. For this reason, untangling the causes of the kinematic structure can give us vital information about the history of the Milky Way and its interactions with its nearest neighbours.

The approach to studying nearby kinematic space has bifurcated into the study of the Galactic disc (e. g. Dehnen 1998; Kushniruk et al. 2017; Antoja et al. 2018; Lucchini et al. 2022; McMillan et al. 2022) and the study of the Galactic stellar halo (e. g. Koppelman et al. 2019a,b; Koppelman & Helmi 2021a; Lövdal et al. 2022; Ruiz-Lara et al. 2022; Dodd et al. 2022). This seems only natural with the two stellar components recording different dynamical processes. The Galactic disc in the Solar neighbourhood shows evidence of dynamical resonances from the spiral arms and the bar (Antoja et al. 2010; Trick et al. 2021). The stellar halo, however, records evidence of mergers between the Milky Way and its neighbours (e.g., Helmi 2020) which in the Λ cold dark matter (ΛCDM) model is how galaxies build up their halos. Finding the causes behind the structures that we can see in the velocity distributions of the local Galaxy will be an important step towards fully understanding its complex history.

As noted by Helmi (2020), large samples with accurate kinematics are required if we are to detect each individual structure. This requirement is now starting to met by the advent of *Gaia* (Gaia Collaboration et al. 2016) and it's subsequent data releases: DR2 (Gaia Collaboration et al. 2018a), EDR3 (Gaia Collaboration et al. 2021a), and DR3 (Gaia Collaboration et al. 2022). Thanks to this, we now have over 1.4 billion sources measured with 5D phase-space coordinates: positions and proper motions. As of DR3, ∼33 million sources also have radial velocities, about 2% of all sources, increased from 0.5% in EDR3. Unfortunately as we start to look at more local samples, apply quality cuts, and pick out specific populations, the number of useful sources can rapidly decline. As an example consider the local ($\varpi > 1/3$ mas) stellar halo (defined as $v_\mathrm{T} > 200\,\mathrm{km s^{-1}}$) with good parallaxes ($\varpi/\sigma_\varpi > 10$). This sample will contain 503 572 sources with 5 parameters, which is reduced to only 84 784 with measured radial velocities. By working without radial velocities we are able access significantly larger datasets and important discoveries can still be reached as demonstrated by previous works using only proper motions (e.g., Dehnen & Binney 1998; Dehnen 1998; Antoja et al. 2017; Koppelman & Helmi 2021b; Gaia Collaboration et al. 2021b; McMillan et al. 2022).

⋆ E-mail: mikkola@astro.lu.se
† E-mail: paul@astro.lu.se

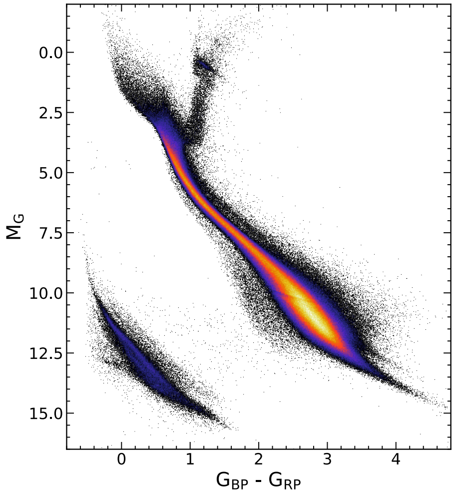

Figure 1. Colour-Magnitude diagram of our Solar neighbourhood sample. The colour shows the number density of sources. We exclude bins with N < 5 stars in them.

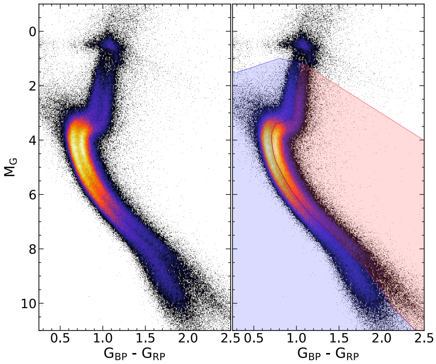

Figure 2. *Left*: Colour-Magnitude diagram of our sample of stars with $V_T > 200$kms^{-1} corrected for extinction effects. The two sequences from Gaia Collaboration et al. (2018b) are clearly visible. *right*: The same plot but showing the regions used to isolate the left and right sequences in red and blue respectively. The color shows the number density of sources and again we exclude bins with N < 5 stars in them.

Table 1. The names of the various samples used and the number of sources in them

Name	*N*	Description
`SNBH`	1 171 846	Stars in the Solar neighbourhood defined as $\varpi > 5$ mas
`SNBH_NORTH`	578 368	Same as `SNBH` but with $b > 0$
`SNBH_SOUTH`	593 478	Same as `SNBH` but with $b < 0$
`SNBH_RVS`	510 478	Same as `SNBH` but with measured radial velocities
`HALO_LEFT`	239 115	Left halo sequence, see Section 2.
`HALO_RIGHT`	194 507	Right halo sequence, see Section 2
`HALO_RVS`	69 820	Our halo sample but with measured radial velocities

In our previous paper Mikkola et al. (2022) (hereafter referred to as Paper I), we implemented the penalized maximum-likelihood method of Dehnen (1998) to infer the 3D velocity distribution of white dwarfs in *Gaia* EDR3. We apply the same method here to the Solar neighbourhood to view the velocity distribution in unprecedented velocity resolution. Additionally we also investigate the stellar halo which has been shown to host many structures which are likely due to the merger history of the Galaxy (see e. g. Dodd et al. 2022 and references therein) with Naidu et al. (2020) even suggesting the halo could be almost entirely comprised of substructure.

The paper is organised as follows: In Section 2 we describe the data selection and the quality cuts that have been made to provide a local disc-dominated sample and a stellar halo sample. We outline some of the differences and new additions we have made to the method from Paper I in Section 3. Then in Section 4 we present the velocity distribution for the Solar neighbourhood disc population. The stellar halo is results are shown in Section 5 where we discuss each of the features we see and compare to literature, as well as present new features that we identify and discuss our findings. We finally summarise with our conclusions in Sections 6.

2 SAMPLE SELECTION

The largest sample of stars with transverse velocities is available from Gaia DR3 through the Gaia Archive[1]. For all of the samples we perform a series of quality cuts, most of which are visible in our ADQL queries (which we provide in appendix A). We select stars with $\varpi/\sigma_\varpi > 10$ as a strong cut on parallax uncertainties lets us approximate distance as $d = 1/\varpi$. We also filter `ruwe` < 1.15 to ensure good quality astrometric solutions (Lindegren 2018) after inspection of the `ruwe` distribution. Additionally, Lindegren et al. (2018) explains that for five-parameter solutions to be accepted at least six separate observations are used (called `visibility_periods_used` in the archive). As in Gaia Collaboration et al. (2018b) we use a stronger filter of at least 8 which removes outliers at the fainter end. In addition, we use their criteria for `astrometric_chi2_al` and `astrometric_n_good_obs_al` to remove artefacts due to excess astrometric noise. Finally we use their quality filters for relative flux error on photometry:

`phot_g_mean_flux_over_error` > 50,

`phot_rp_mean_flux_over_error` > 20, and

`phot_bp_mean_flux_over_error` > 20.

Beyond this, we also calculate the flux excess in BP and RP, C^*, following the procedure of Riello et al. (2021) directly in our query as in Gaia Collaboration et al. (2021a). We then select stars such that $C^* < 3|\sigma_{C^*}|$.

Our Solar neighbourhood sample contains stars which have $\varpi > 5$ mas ($d \lesssim 200$ pc). This sample is further split into north and south Galactic hemisphere samples with $b > 0$ and $b < 0$

---

[1] https://gea.esac.esa.int/archive/

respectively. The final result of our filters on this sample can be seen in the colour-magnitude diagram (CMD) in Fig. 1. We also create a Solar neighbourhood sample from the Gaia RVS for comparison.

To generate a sample of halo stars we select stars with a transverse velocity, $v_{\mathrm{T}} > 200$ kms^{-1} as in Gaia Collaboration et al. (2018b) where it was shown this reveals two dual well-defined sequences, the standard sequence of the Solar neighbourhood and a new sequence to the left consistent with a more metal-poor population. This cut on velocity will remove some low velocity halo stars, but more importantly removes the majority of disc stars. This means our sample contains slightly fewer stars but is purer, allowing us to identify the sequences more easily. The smaller sample also makes computations less demanding. We further require $\varpi > 1/3$ mas ($d \lesssim 3$ kpc) to ensure we avoid orbits belonging to the bulge.

Our Solar neighbourhood sample should be mostly unaffected by extinction and it will not have any bearing its analysis either. For the halo sample however, we need to isolate the two sequences in the CMD and therefore it is important we treat it correctly. To correct our colours and magnitudes, we use the extinction map of Capitanio et al. (2017)[2] to determine the reddening for our stars . We pair this with extinction coefficients for the Gaia bands $G, G_{\mathrm{BP}}, G_{\mathrm{RP}}$ from Sanders & Das (2018) to reduce the effects of extinction. Using the corrected values, we show the CMD in Fig. 2 which clearly shows the two separate sequences. Splitting the sample into a left and right sequence sample can be done reliably by eye and the selection is shown with blue and red shaded regions respectively.

We list the names of our sample as well as the number of sources contained within them in Table 1.

3 VELOCITY DISTRIBUTION WITHOUT RVS

We have used the same maximum penalized-likelihood algorithm from Dehnen (1998) that was used for Paper I. We summarise the key elements of this approach here, and a more detailed explanation can be found in our earlier paper. The method makes use of the projection of transverse velocities on the sky. The probability distribution of these transverse velocities in a specific direction, $\hat{\boldsymbol{r}}$, we write as $\rho(\boldsymbol{q}|\hat{\boldsymbol{r}})$ where $\boldsymbol{q}$ is the 2D transverse velocity. This relates to the 3D velocity distribution, $f(\boldsymbol{v})$, as:

$$\rho(\boldsymbol{q}|\hat{\boldsymbol{r}}) = \int \mathrm{d}v_r\, f(\boldsymbol{v}) = \int \mathrm{d}v_r\, f(\boldsymbol{p} + v_r\hat{\boldsymbol{r}}). \tag{1}$$

Here, $\boldsymbol{p}$ is the tangential motion of a star projected into 3D. Tangential motion is not sufficient to determine a true distribution and instead we must estimate it with a log-likelihood of a model for it. Numerically, we use the discrete velocity distribution

$$f(\boldsymbol{v}) = e^{\phi(\boldsymbol{v})}, \tag{2}$$

where $\phi(\boldsymbol{v})$ is the logarithm of the probability density, which we discretize on a 3D grid of $L_U \times L_V \times L_W$ cells with widths $h_U \times h_V \times h_W$[3]. The resulting function which we use in our maximum penalized-likelihood estimation is:

$$\tilde{\mathscr{Q}}_\alpha(\boldsymbol{\phi}) = N^{-1}\sum_k \ln\left[\sum_{\boldsymbol{l}} e^{\phi_{\boldsymbol{l}}} K(k|\boldsymbol{l})\right] - \sum_{\boldsymbol{l}} e^{\phi_{\boldsymbol{l}}} - \frac{1}{2}\alpha h_x h_y h_z \sum_{\boldsymbol{l}} \left(\sum_{\boldsymbol{n}} \phi_{\boldsymbol{n}} \Xi_{\boldsymbol{nl}}\right)^2. \tag{3}$$

The first term is the sum of the probability distribution function with N being the sample size. For each star, k, the length in velocity space of the line formed by its tangential velocity and all possible radial velocities through a cell, $\boldsymbol{l}$, is $K(k|\boldsymbol{l})$. The second term is a normalising term and the third is the penalizing term where $(\sum_{\boldsymbol{n}} \phi_{\boldsymbol{n}} \Xi_{\boldsymbol{nl}})$ is a numerical approximation for the second derivative of $\phi(\boldsymbol{v})$ for a given cell. This term therefore penalizes unsmooth solutions and is scaled by the smoothing parameter, α.

We use a similar method for determining the optimal value of α as in Paper I. That is, we compare many estimations of an equally sized RVS sample using different α. For all stars in the Solar neighbourhood the RVS sample is only half as large as the sample without v_r so we have to upscale our sample. We create a copy of the RVS sample, `SNBH_RVS` where the Galactic positions are sampled randomly from the original. The velocities are taken from the RVS, with each proper motion and radial velocity resampled from a multivariate Gaussian with the measured values as mean, and with uncertainties and correlation coefficients in the covariance matrix. With a randomly selected Galactic position this then transforms to Galactic velocities, U, V, W, and this copy is then projected back into on-sky motions with the radial velocities discarded.

For the Solar neighbourhood sample, the upscaling only needs to be done once as the RVS is half the size of the full dataset. We then compare the estimated $\tilde{f}^{\alpha}_{\boldsymbol{v}}$ with the real RVS $f_{\boldsymbol{v}}$ and select the α that gives the smallest integrated square error (ISE)

$$D(\tilde{f}^{\alpha}_{\boldsymbol{v}}, f_{\boldsymbol{v}}) = \int d^3\, \boldsymbol{v}(\tilde{f}^{\alpha}_{\boldsymbol{v}} - f_{\boldsymbol{v}})^2. \tag{4}$$

This gives for the full Solar neighbourhood sample an optimal smoothing of $\alpha = 10^{-11}$ for a $\boldsymbol{n} = [304, 304, 192]$ grid over the ranges $U \in [-150, 150]$ kms^{-1}, $V \in [-200, 100]$ kms^{-1}, $W \in [-100, 100]$ kms^{-1}, corresponding to a resolution of ~1 kms^{-1}. The same setup is used for the north and south Galactic hemisphere samples to ensure the differences are not by construction. This will however result in a slightly under-smoothed distribution for the smaller samples.

For the stellar halo, the `HALO_RVS` sample is about 3 times smaller than the two samples `HALO_LEFT` and `HALO_RIGHT` and we upscale it to three times its original size. We also no longer use heliocentric Cartesian velocity coordinates, U, V, W but instead use Galactocentric spherical velocities, v_r, v_ϕ, v_θ defined such that for a star in the galactic plane at the position of the Sun, v_ϕ and v_θ are in the same direction as V and W, respectively, to make comparisons easier. To make to transformation, we have assumed the Sun's position to be $(R, z) = (8122, 20.8)$ pc and its velocity $(U, V, W) = (12.9, 245.6, 7.78)$ km s^{-1} with respect to the Galactic centre. On a grid of $\boldsymbol{n} = [240, 240, 240]$ with v_r, v_ϕ, and v_θ all in the range $[-600, 600]$ kms^{-1} corresponding to a resolution of 5 kms^{-1}, the value of α that minimises the ISE is 4.64×10^{-13} and is used for both halo samples.

One difference between our approach when handling the Solar neighbourhood sample and when handling the halo sample is how the velocity dispersion, $\boldsymbol{\sigma}$, and average velocity, $\langle \boldsymbol{v} \rangle$, are determined. For the former sample we can determine $\boldsymbol{\sigma}$ and $\langle \boldsymbol{v} \rangle$ of the sample

---

[2] `https://stilism.obspm.fr/`

[3] U, V and W are the usual heliocentric velocity components in the direction towards the Galactic centre, towards Galactic rotation, and towards the north Galactic pole, respectively

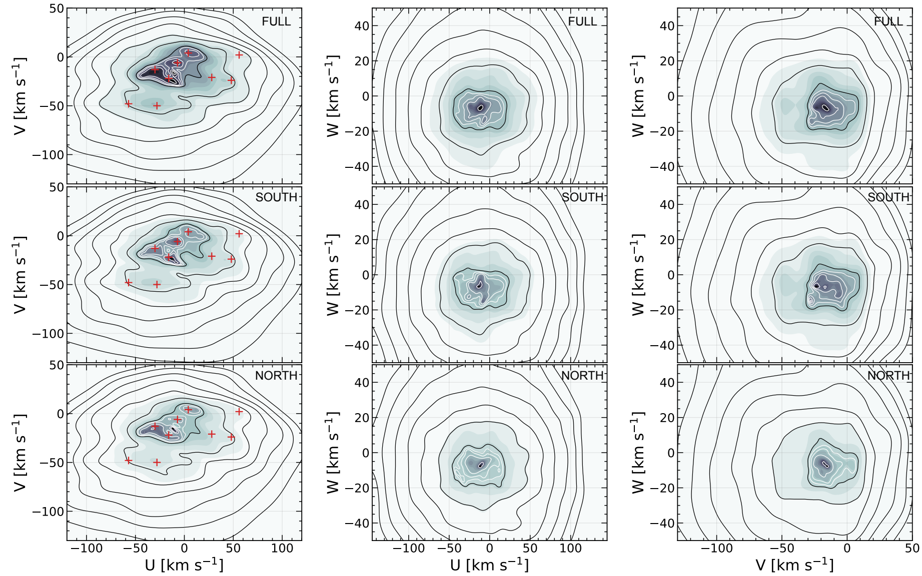

Figure 3. Galactic velocity distributions. The colormap shows the probability distribution, $f(\boldsymbol{v})$. The contour lines contain 99, 98, 96, 92, 84, 68, 35, 27, 18, 10, and 1 percent of all the stars, from outside going inward. The white contours start at 27%. *First row:* The velocity distribution of the `SNBH_FULL` sample. In the first column, the location of the first 9 groups of Antoja et al. (2012) are shown as red crosses. *Second row:* Same as the first row, but for the `SNBH_SOUTH` sample. *Third row:* Velocity distribution of `SNBH_NORTH`.

directly, following the procedure of Dehnen & Binney (1998) (as in Mikkola et al. (2022)), but for the latter case we use spherical coordinates and it becomes unnecessarily complex. Instead, we determine $\langle \boldsymbol{v} \rangle$ and $\boldsymbol{\sigma}$ for the subset of the sample that has measured radial velocities. However, since $\boldsymbol{\sigma}$ and $\langle \boldsymbol{v} \rangle$ are only used for the initial guess of $\phi(\boldsymbol{v})$ and as scaling factors for determining α, we are free to find σ however we wish without significant consequences for the analysis.

4 THE SOLAR NIGHBOURHOOD

The velocity distribution estimated for the Solar neighbourhood sample is seen in Fig. 3. The first row shows distribution for the complete sample and the second and third rows show the south and north Galactic hemisphere samples respectively. We find that the distribution is mostly dominated by the common features: *Sirius*, *Coma Berenices*, *Hyades*, *Pleiades*, *Hercules*. We can also identify *Dehnen98* and *Wolf 630* to an extent. The first four of the major groups occupy a region that contains roughly 35% of all the stars in the sample, shown by the white contour lines. We can see the incomplete vertical face-mixing of *Coma Berenices* (Quillen et al. 2018; Monari et al. 2018; Bernet et al. 2022) as it is a much stronger feature in the southern Galactic hemisphere. A curious feature that appears more strongly in the northern hemisphere is the rather strong overdensity between *Pleiades* and the expected position of *Coma Berenices* at roughly $(U, V) = -10, -15$ kms^{-1}. This feature is clearly separate from *Pleiades* and we find no match for it in the list of moving groups in Antoja et al. (2017), Kushniruk et al. (2017), or Lucchini et al. (2022). The close proximity to *Pleiades* suggests that this feature is now visible thanks to the improved velocity resolution. Overall we find limited detailed substructure in the direct velocity distribution which shows the dominance of the major moving groups in this space.

4.1 Conditional $f(\boldsymbol{v})$ of the Solar neighbourhood

To unravel low-level structure that the representations of the velocity distribution of Fig. 3 may have missed, in Fig. 4 we renormalize the plots so that, rather than showing the full 2D probability density of U and V, we show the *conditional* probabilities of V or U for each U or V, respectively. That is, the colour represents the probability of the star having a specific V given that it has certain U velocity (or vice versa).

In addition to the structure we have seen above, we can see in $P(V|U)$ around $(U, V) = -100, -50$ km s^{-1} a structure that matches well with estimates of *ϵInd* (e.g., Antoja et al. 2012; Bobylev & Bajkova 2016; Kushniruk et al. 2017). Above it, closer to $V = -10$ km s^{-1} is another feature that matches to a group identified by Bobylev & Bajkova (2016) and Kushniruk et al. (2017). There are also features with positive U sitting at $V \approx -30$ km s^{-1} with $U = 50$ km s^{-1} and $U = 100$ km s^{-1}, the first of which is the *Dehnen98* group from Antoja et al. (2012), which itself is from Dehnen 1998. The second group is likely *Antoja12* (see Kushniruk et al. 2017 and references therein). This demonstrates the strength of plotting conditional probabilities for the inferred velocity distributions to gain insight into low-level structures.

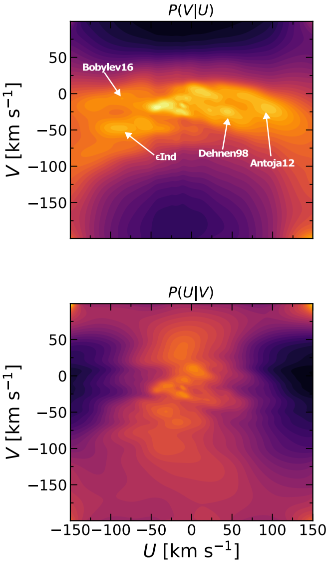

Figure 4. The conditional probability on $f(U, V)$ on either U or V for the top and bottom plot respectively. The density is scaled such that $P(v)^{0.25}$ to reveal low probability structure. Some features discussed in the text are highlighted.

5 THE LOCAL STELLAR HALO

We present the velocity distribution of the stellar halo in the planes (v_r, v_ϕ), (v_r, v_θ), and (v_ϕ, v_θ) in Fig. 5 estimated through our penalized maximum-likelihood method. The figure very clearly shows the separation into a blue accreted population and a red in-situ halo or hot thick disc. The blue accreted population occupies phase space almost symmetrically around $v_\phi = 0$ and does not continue smoothly from the disc population, with multiple substructures.The red, in-situ halo or hot thick disc on the other hand has very little substructure and is mostly a continuation of the disc phase space distribution.

Since our main interest is in the substructure of the accreted halo, throughout the rest of this paper we only look at the `HALO_LEFT` sample.

For this sample we can see that there are a plethora of features. We overlay the distribution with known features from literature, revealing which of these we do or do not see from this perspective of the population. The extent of these shapes has been adapted from Koppelman et al. (2019a) and Naidu et al. (2020). We will now go over and discuss the features we can see in our distributions.

5.1 Gaia-Sausage-Enceladus

The strongest feature across all velocity space is the *GSE* and this feature is not continuous but rather appears to be a composition of multiple different features which we have labelled in the top-left of Fig. 5 as G1-5 in (v_r, v_ϕ). Since our cut of $v_\mathrm{T} > 200$ km s^{-1} is rather generous, we expect there to be some contamination between the samples. Thus, G2 and G4 are likely contaminants from the two features seen in the `HALO_RIGHT` sample in the third row of Fig. 5. G1 and G5 appear in the space of what is typically associated with the GSE (e. g. Koppelman et al. 2019a; Feuillet et al. 2021; Dodd et al. 2022) while the central group, G3, appears likely to be the *L-RL3* group in Dodd et al. (2022) who identifies it with Cluster 3 in Lövdal et al. (2022). The GSE appears slightly asymmetric on either side of $v_\phi = 0$ here because of our cut on tangential velocity removing some of its lower v_ϕ members and including some contaminants from the disc.

5.2 Sequoia & Antaeus

Some noticeable features are the 'horns' sticking out at the bottom in (v_r, v_ϕ) at $v_\phi = -250$ km s^{-1} and around $v_r = \pm 200$ km s^{-1} and to the left in (v_ϕ, v_θ) around $v_\theta = \pm 150$ km s^{-1}. These features are in the location associated with *Sequoia* (Myeong et al. 2019). In Naidu et al. (2020) this region is mixed with groups *Arjuna* and *I'itoi* which are distinguished from one another by their metallicities. Since we do not have metallicity measurements here we will refer to the dynamical space occupied by these features simply as *Sequoia*. In the same space we can also see the *Antaeus* group from Oria et al. (2022) which shares many of the same attributes as *Sequoia*. It is not clear to what extent these features are separate but Oria et al. (2022) claims that the low J_z and position in the disc plane of Antaeus are unique.

5.3 Helmi streams

Two of the most prominent substructures that appears in all the distributions are the *Helmi streams* (Helmi et al. 1999). They are also among the first identified substructures. An updated view of the streams lets us narrow them down in velocity space (Koppelman et al. 2019a,b; Koppelman & Helmi 2021a). This feature is particularly strong and is bimodal in v_θ, with the lower v_θ group being far more represented as expected (e.g., Koppelman et al. 2019b). At slightly larger v_ϕ we would expect to find *Aleph*, reported first in Naidu et al. (2020), but in our sample it appears to be absent.

5.4 Thamnos

The structure *Thamnos* was identified by Koppelman et al. (2019b) using the *Gaia* DR2 RVS sample supplemented with line-of-sight velocities and abundances from RAVE (Kunder et al. 2017), APOGEE (Abolfathi et al. 2018), and LAMOST (Cui et al. 2012). Their sample was limited to 3 kpc like halo samples. In our distributions there is no distinct separate feature corresponding to *Thamnos*, but in both (v_r, v_ϕ) and (v_ϕ, v_θ) the distribution's densest parts extends to slightly lower v_ϕ than for the *GSE* structure, which may be due to the presence of Thamnos. It is suggested by Naidu et al. (2020) that *Thamnos* may be more discernible at larger distances where the *GSE* and disc-like stars contribute less to the distribution.

5.5 Other structures

In addition to the structures mentioned above we find several others in these projections. One of these can be associated with a known velocity structure, *ED-2* from Dodd et al. (2022) and is marked with a cerise shaded region. This feature is close to Sequoia at $(v_r, v_\phi) = (-150, -300)$ km s^{-1} and presents in $(v_\phi, v_\theta) = (-300, -100)$ km s^{-1}. To verify if they are the same

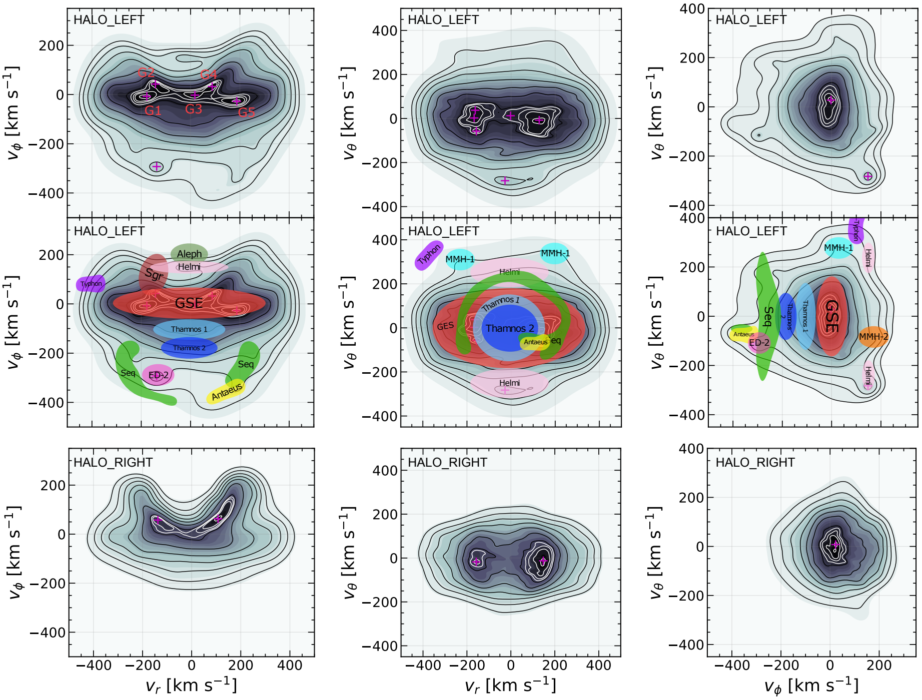

Figure 5. Velocity distributions in spherical coordinates. The colormap shows the square root of the probability distribution, $\sqrt{f(v)}$, to enhance fainter structure. The contour lines are the same as in Fig. 3. *First row:* The velocity distribution of the `HALO_LEFT` sample. Five distinct features thought belonging to the region occupied by GSE are labelled. *Second row:* Same as the first row, but overlaid with rough expected positions of reported substructures from literature in similar style to Naidu et al. (2020) and Mardini et al. (2022) but in velocity space. *Third row:* Velocity distribution of `HALO_RIGHT`, with very little substructure. Because we are interested in the substructure found in `HALO_LEFT` we focus exclusively on this sample in subsequent figures.

structure, we investigate the full 3D velocity structure to find that the features overlap and are one and the same.

In Dodd et al. (2022), they assign 33 members to the cluster in their sample of 72 274 stars (or ~0.05%). We can look at the fraction of the probability density that occupies the region. We define the region around the group with $v_r \in [-175, -100]$ km s^{-1}, $v_\phi \in [-325, -275]$ km s^{-1}, and $v_\theta \in [-100, -150]$ km s^{-1} and find that ~0.074% of the sample lies there, corresponding to ~180 stars in the sample. This suggests that the very dense feature is slightly more prominent than previous believed.

At slightly larger v_r than the even the large v_θ Helmi stream, around $(v_r, v_\theta) = (-250, 300)$ km s^{-1} and $(v_r, v_\theta) = (200, 350)$ km s^{-1}, we find a new feature split across two different values of v_θ. At such a large v_θ we also find a new structure in (v_ϕ, v_θ) at $(25, 300)$ km s^{-1}. We refer to these groups as a single feature which we call *MMH-1*. In the full 3D probability distribution the positions of *MMH-1* overlap and we consider them the same feature.

Lastly, at $(v_\phi, v_\theta) = (150, -100)$ km s^{-1}, another feature can be seen. At such values of v_ϕ and v_θ it is difficult to discern any stronger feature in the spaces of (v_r, v_ϕ) and $(v_r v_\theta)$ as the region is crowded particularly in (v_r, v_ϕ) where it would lie close to the cutoff caused by our tangential velocity limit. We refer to this feature as *MMH-2*.

5.6 Conditional $f(v)$ of the local halo

In much the same way as we did in Fig. 5, we again use conditional probabilities to illustrate our halo velocity maps with respect to one of the two velocity dimensions to investigate faint structure that otherwise may not be visible. We show these conditional probability maps in Fig. 6 which reveal more of the surrounding velocity structure with certain features become strikingly visible. For example the two-pronged structure around *Sequioa*, *Antaeus*, and *ED-2* is much more readily apparent in $P(v_r|v_\phi)$ and $P(v_\theta|v_\phi)$ than before. The separation of the *GSE* from the hot thick disc is apparent in both $P(v_r|v_\phi)$ and $P(v_\phi|v_r)$, and it is located primarily around two features around $v_\phi \pm [150, 300]$ km s^{-1}. The region occupied by *Thamnos* is now also readily apparent where it was not before.

Our two novel groups, *MMH-1* and *MMH-2*, appear in these figures as well. The first, *MMH-1*, which has a large v_θ of around 300 km s^{-1} appears in the conditional probabilities $P(v_r|v_\theta)$

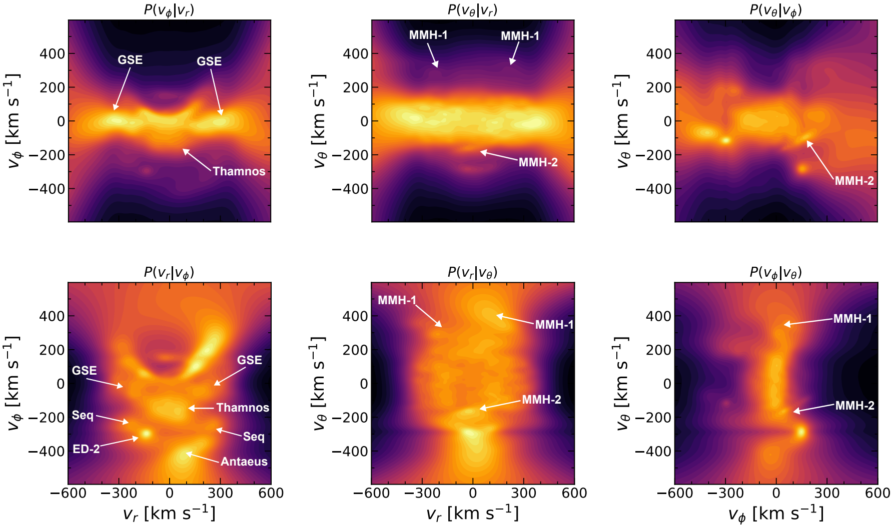

Figure 6. The conditional probability of the three different spaces in each column and velocity space as Fig. 5 for the `HALO_LEFT` sample. Top row is conditional probability on the x-axis coordinate and bottom row on the y-axis coordinate. We show specifically $P(v)^{0.25}$ to reveal low probability structure even further.

and $P(v_\phi|v_\theta)$ corresponding to the bottom row, middle and last columns. It also stretches up towards much larger extents in v_θ, but it is unclear if this structure is physical given how far out in the edges of the distribution it lies. Similarly there is a symmetric feature at large negative v_θ near -400 km s^{-1} which, if real, could relate to *MMH-1*. The group *MMH-2* appears strongly in (v_ϕ, v_θ) for both $P(v_\phi|v_\theta)$ and $P(v_\theta|v_\phi)$.

A feature we have not discussed previously which is present in $P(v_\theta|v_r)$ and $P(v_r|v_\theta)$ is the sloped feature around $(v_r, v_\theta) = (0, -150)$ km s^{-1}. This feature is also visible in Fig. 5 and does not appear in the other papers we have reviewed and is very difficult to find in the other spaces, suggesting it lies at rather low v_ϕ as this would place it close to the densest parts of the distribution, thus obscuring it from detection. We have confirmed this by limiting the (v_r, v_θ)-space to separate bins of v_ϕ, which reveals that the feature only appears between $v_\phi \in [0, 100]$ km s^{-1}. This means the feature is most likely the representation of *MMH-2* in this space.

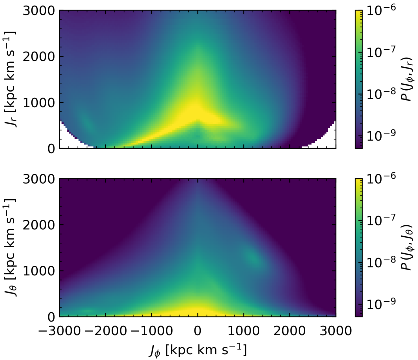

Figure 7. Action distribution associated with our `HALO_LEFT` sample. The probability density is in units of kpc^{-2} km^{-2} s^{2}. While there are strong selection effects that shape these distributions, we are still able to see some of the substructure in this projection of the data, most strikingly the Helmi stream in the lower panel near $(J_\phi, J_\theta) = (1500, 1200)$ kpc km s^{-1}.

5.7 Action space distribution

A very common method of searching for accreted substructure in the Milky Way halo is to work in terms of integrals of motion (e.g., Helmi et al. 1999). In particular, the orbital actions have become commonly used since a convenient approximation within galaxy potentials became available (Binney 2012). When stars in a sample are distributed over a large volume in the Milky Way it is essential to use techniques like these to identified substructure accreted long ago because, while we can expect stars accreted together to have very similar integrals of motion, they will have very different velocities if they are in very different parts of the Galaxy.

We have very deliberately limited our sample to a relatively local volume within the stellar halo so that stars on similar orbits have similar velocities. Nonetheless, to make consistent comparison with other studies possible, it is still valuable to determine the distribution of the stars in terms of their orbital actions. We use the AGAMA software package (Vasiliev 2019) to determine the actions in the Milky Way gravitational potential from McMillan (2017) rescaled such that the Sun's position and velocity are consistent with the values given in Section. 3. Fig. 7 shows this action distribution in terms of J_r or J_θ against J_ϕ,[4] where we have approximated that

---

[4] J_ϕ is the conserved component of angular momentum, while J_r characterises the radial oscillation and J_θ that of oscillation in the θ direction.

stars are at the position of the Sun. Changing this assumed position within our survey volume does not make any important qualitative difference.

The distributions in Fig. 7 are clearly shaped by the selection effects that apply to them. At high $|J_\phi|$ there is a lower limit for J_r below which there is no orbits that pass the Sun's position. At lower $|J_\phi|$, there is a minimum J_r that reaches the Sun's position for $J_\theta = 0$, and this is where we find the bright maximum in the (J_ϕ, J_r) distribution that runs from approximately $(-1500, 0)$ to $(0, 600)$ kpc km s^{-1}, which is a selection effect. For $J_\theta > 0$ there are orbits that reach the solar position at these J_ϕ with lower J_r, so the density does not fall to zero below this point. There is an upper envelope for J_θ at a given J_ϕ, above which the density becomes very low. This is a consequence of the requirement that the orbit reaches the Sun's position and is bound to the Galaxy.

Nonetheless, there are features of the velocity distribution that stand out in these plots too. The GSE stands out as a strikingly high density of stars over a large range in J_r around $J_\phi = 0$. ED-2 is clearly seen in both panels at $(J_r, J_\phi, J_\theta) = (600, -2450, 90)$ kpc km s^{-1}; the Helmi Stream is clearly visible in the (J_ϕ, J_θ) plane around $(1300, 1200)$ kpc km s^{-1} and expected at a J_r of 80 kpc km s^{-1}; the Sequoia group produces an overdensity that can be seen around $(J_\phi, J_r) = (-2000, 1000)$ kpc km s^{-1}. Otherwise, for our sample the substructure is substantially clearer in the velocity distribution than in these action distributions.

We note, in the interests of finding members of our newly discovered substructure in future study of samples beyond the Solar neighbourhood, that in our assumed potential these have actions (J_r, J_ϕ, J_θ) around $(1450, 200, 2300)$ and $(70, 1200, 200)$ kpc km s^{-1} for MMH-1 and MMH-2 respectively.

Finally, we can use angle-action modelling to justify an assumption underlying our approach: that it is reasonable to approximate the velocity distribution of the stellar halo as independent of position in our sample volume. To provide a realistic example, we use the Torus Code (Binney & McMillan 2016) we sample the points from the phase-mixed orbit corresponding to the approximate actions of the Helmi and ED-2 streams. For the Helmi stream we focus only on component at $v_\theta < 0$ (by symmetry the equivalent at $v_\theta > 0$ will have the same spread in velocity), while for ED-2 we also limit it to $v_r < 0$ to match the major component we observe. For the points on the orbital torus sampled within our survey volume, we have a dispersion in v_ϕ of 12 km s^{-1} and in v_θ of 17 km s^{-1} for the Helmi Stream, and of $(50, 40, 30)$ km s^{-1} in (v_r, v_ϕ, v_θ) for ED-2. This spread is comparable to that seen in for these groups in Fig. 5, which is quite small on the scale of the velocity distribution that we are studying, and clearly does not prevent us from finding substructure. We note also that this is likely to be an overestimate of the associated dispersion, because the real sample has a smaller spread in position, being preferentially near the Sun, and this smaller spread in position, for a given orbital torus, corresponds to a smaller spread in velocity.

6 CONCLUSIONS

We use DR3 astrometry data without radial velocities, giving us access to a significantly larger catalogue of stars. With the penalized maximum likelihood algorithm implemented in Paper I we can then infer full 3D velocity distributions to investigate the Solar neighbourhood for substructure. We analyse the Solar neighbourhood in two separate stellar components: the Galactic disk and the stellar halo. The disk is also split into a north and southern hemisphere based on Galactic latitude as in Monari et al. (2018) and we find that the overall velocity distribution is dominated by the four major moving groups; *Sirius*, *Coma Berenices*, *Hyades*, and *Pleiades*, with 35% of stars lying in and around them. However, we find some degree of asymmetry with Galactic latitude with *Coma Berenices* being most prominent in the southern hemisphere in agreement with previous results (Quillen et al. 2018; Monari et al. 2018; Bernet et al. 2022). We also identify a new structure at $(U, V) = -10, -15$ km s^{-1} which does not align with any known moving groups.

For the local stellar halo, we use the same approach as Gaia Collaboration et al. (2018b) to reveal a double main sequence for stars with $v_{\mathrm{T}} > -200$ km s^{-1} which we split into in an *'in-situ'* and *'accreted'* population to the right and left in the CMD respectively. These samples are then used to infer the velocity distributions in spherical Galactocentric coodrinates, v_r, v_ϕ, and v_θ. We see that we can reliably make out several of the more well-known features of the stellar halo in the *'accreted'* sample: *GSE*, *Sequoia*, *Helmi streams*, and *Thamnos* are all visible in our sample. We also find three addition structures, the first of which is identified already as *ED-2* in Dodd et al. (2022). We then have a new structure, *MMH-1*, appear at large v_θ, split into two locations at $(v_r, v_\theta) = (-250, 300)$ km s^{-1} and $(v_r, v_\theta) = (200, 350)$ km s^{-1}. It also appears at $(v_\phi, v_\theta) = (25, 300)$ km s^{-1}. By inspection of the full 3D velocity space we confirm this as one feature with velocities $(v_r, v_\phi, v_\theta) = (\pm 225, 25, 325)$ km s^{-1}. Lastly we also have the new feature *MMH-2* at $(v_\phi, v_\theta) = (150, -100)$ km s^{-1} which we trace into v_r, which gives it velocities $(v_r, v_\phi, v_\theta) = (0, 150, -125)$ km s^{-1}. These velocity distributions gives us the appearance of the stellar halo at 'face value', which provides a clear idea of what structure can be expected there and to what extent.

In addition to this we investigated the conditional velocity distributions upon which provides further support for the existence of these structures and their extent. This is where we also find a match for *MMH-2* in v_r, which was not as readily apparent in the standard distributions.

Furthermore we transform our velocity distributions into action space distributions and identify the location of several of the previous substructures there as well. This further demonstrates the possibilities of our approach and lets us connect between velocity space and orbital space.

This work demonstrates what can be achieved without needing to rely on the full 6D phase-space information. During the era of *Gaia*, there will be more sources with astrometry alone than with added radial velocities due to the inherent differences in the methods by which the measurements are obtained. Currently around 2% of the data has radial velocities and with spectroscopic follow-up this is likely to increase, but not match the amount of pure astrometric sources. In the next era with a successor mission in the infrared (Hobbs 2022, submitted)[5] the amount of radial velocities could increase significantly. This will mean that enough sources will be available that more discoveries can be made directly with 6D data, but the proper motions will remain more numerous and so methods such as these will be pivotal.

---

[5] Proceedings of the XXXI IAU General Assembly, to be published in Cambridge University Press

ACKNOWLEDGEMENTS

This work has made use of data from the European Space Agency (ESA) mission *Gaia* (`https://www.cosmos.esa.int/gaia`), processed by the *Gaia* Data Processing and Analysis Consortium (DPAC, `https://www.cosmos.esa.int/web/gaia/dpac/consortium`). Funding for the DPAC has been provided by national institutions, in particular the institutions participating in the *Gaia* Multilateral Agreement. This work made use of Astropy:[6] a community-developed core Python package and an ecosystem of tools and resources for astronomy (Astropy Collaboration et al. 2013, 2018, 2022).

We thank members of Lund Observatory for helpful comments and ideas. Computations for this study were performed on equipment funded by a grant from the Royal Physiographic Society in Lund. PM is supported by research project grants from the Swedish Research Council (Vetenskaprådet Reg: 20170-03721 and 2021-04153). DH and PM gratefully acknowledge support from the Swedish National Space Agency (SNSA Dnr 74/14 and SNSA Dnr 64/17).

DATA AVAILABILITY

All data analysed in this paper are publicly available from the Gaia archive (`http://gea.esac.esa.int/archive/`). The 3D probability distributions used in Figures 3 and 5 are available upon request to the corresponding author.

REFERENCES

Abolfathi B., et al., 2018, ApJS, 235, 42
Antoja T., Figueras F., Torra J., Valenzuela O., Pichardo B., 2010, in , Vol. 4, Lecture Notes and Essays in Astrophysics. pp 13–31
Antoja T., et al., 2012, MNRAS, 426, L1
Antoja T., de Bruijne J., Figueras F., Mor R., Prusti T., Roca-Fàbrega S., 2017, A&A, 602, L13
Antoja T., et al., 2018, Nature, 561, 360
Astropy Collaboration et al., 2013, A&A, 558, A33
Astropy Collaboration et al., 2018, AJ, 156, 123
Astropy Collaboration et al., 2022, ApJ, 935, 167
Bernet M., Ramos P., Antoja T., Famaey B., Monari G., Al Kazwini H., Romero-Gómez M., 2022, arXiv e-prints, p. arXiv:2206.01216
Binney J., 2012, MNRAS, 426, 1324
Binney J., McMillan P. J., 2016, MNRAS, 456, 1982
Bobylev V. V., Bajkova A. T., 2016, Astronomy Letters, 42, 90
Capitanio L., Lallement R., Vergely J. L., Elyajouri M., Monreal-Ibero A., 2017, A&A, 606, A65
Cui X.-Q., et al., 2012, Research in Astronomy and Astrophysics, 12, 1197
Dehnen W., 1998, AJ, 115, 2384
Dehnen W., Binney J. J., 1998, MNRAS, 298, 387
Dodd E., Callingham T. M., Helmi A., Matsuno T., Ruiz-Lara T., Balbinot E., Lovdal S., 2022, arXiv e-prints, p. arXiv:2206.11248
Feuillet D. K., Sahlholdt C. L., Feltzing S., Casagrande L., 2021, MNRAS, 508, 1489
Gaia Collaboration et al., 2016, A&A, 595, A1
Gaia Collaboration et al., 2018a, A&A, 616, A1
Gaia Collaboration et al., 2018b, A&A, 616, A10
Gaia Collaboration et al., 2021a, A&A, 649, A1
Gaia Collaboration et al., 2021b, A&A, 649, A8
Gaia Collaboration Vallenari A., Brown A. G. A., Prusti T., 2022, A&A
Helmi A., 2020, ARA&A, 58, 205
Helmi A., White S. D. M., de Zeeuw P. T., Zhao H., 1999, Nature, 402, 53
Koppelman H. H., Helmi A., 2021a, A&A, 645, A69
Koppelman H. H., Helmi A., 2021b, A&A, 649, A136
Koppelman H. H., Helmi A., Massari D., Roelenga S., Bastian U., 2019a, A&A, 625, A5
Koppelman H. H., Helmi A., Massari D., Price-Whelan A. M., Starkenburg T. K., 2019b, A&A, 631, L9
Kunder A., et al., 2017, AJ, 153, 75
Kushniruk I., Schirmer T., Bensby T., 2017, A&A, 608, A73
Lindegren L., 2018, Re-normalising the astrometric chi-square in Gaia DR2, GAIA-C3-TN-LU-LL-124, `http://www.rssd.esa.int/doc_fetch.php?id=3757412`
Lindegren L., et al., 2018, A&A, 616, A2
Lövdal S., Ruiz-Lara T., Koppelman H. H., Matsuno T., Dodd E., Helmi A., 2022, arXiv e-prints, p. arXiv:2201.02404
Lucchini S., Pellett E., D'Onghia E., Aguerri J. A. L., 2022, arXiv e-prints, p. arXiv:2206.10633
Mardini M. K., Frebel A., Chiti A., Meiron Y., Brauer K. V., Ou X., 2022, ApJ, 936, 78
McMillan P. J., 2017, MNRAS, 465, 76
McMillan P. J., et al., 2022, MNRAS, 516, 4988
Mikkola D., McMillan P. J., Hobbs D., Wimarsson J., 2022, MNRAS, 512, 6201
Monari G., et al., 2018, Research Notes of the American Astronomical Society, 2, 32
Myeong G. C., Vasiliev E., Iorio G., Evans N. W., Belokurov V., 2019, MNRAS, 488, 1235
Naidu R. P., Conroy C., Bonaca A., Johnson B. D., Ting Y.-S., Caldwell N., Zaritsky D., Cargile P. A., 2020, ApJ, 901, 48
Oria P.-A., Tenachi W., Ibata R., Famaey B., Yuan Z., Arentsen A., Martin N., Viswanathan A., 2022, ApJ, 936, L3
Quillen A. C., et al., 2018, MNRAS, 478, 228
Riello M., et al., 2021, A&A, 649, A3
Ruiz-Lara T., Matsuno T., Lövdal S. S., Helmi A., Dodd E., Koppelman H. H., 2022, A&A, 665, A58
Sanders J. L., Das P., 2018, MNRAS, 481, 4093
Trick W. H., Fragkoudi F., Hunt J. A. S., Mackereth J. T., White S. D. M., 2021, MNRAS, 500, 2645
Vasiliev E., 2019, MNRAS, 482, 1525

---

[6] http://www.astropy.org

APPENDIX A: GAIA ARCHIVE QUERY

The following query has been used on the Gaia archive[7] to obtain our `SNBH` samples and is detailed in Section 2:

```
select source_id, bp_rp, phot_g_mean_mag, phot_bp_rp_excess_factor, ruwe, ra, dec,
parallax, pmra, pmdec, parallax_error, pmra_error, pmdec_error, parallax_pmra_corr,
parallax_pmdec_corr, pmra_pmdec_corr, visibility_periods_used, astrometric_chi2_al,
astrometric_n_good_obs_al, radial_velocity,
radial_velocity_error,
if_then_else(
bp_rp > -20,
  to_real(case_condition(
    phot_bp_rp_excess_factor - (1.162004 + 0.011464* bp_rp + 0.049255*power(bp_rp,2)
                                  - 0.005879*power(bp_rp,3)),
    bp_rp < 0.5,
    phot_bp_rp_excess_factor - (1.154360 + 0.033772* bp_rp + 0.032277*power(bp_rp,2)),
    bp_rp >= 4.0,
    phot_bp_rp_excess_factor - (1.057572 + 0.140537*bp_rp)
  )),
  phot_bp_rp_excess_factor
) as excess_flux
from gaiadr3.gaia_source
where parallax_over_error > 10
and parallax > 5
and ruwe < 1.15
and phot_g_mean_flux_over_error > 50
and phot_rp_mean_flux_over_error > 20
and phot_bp_mean_flux_over_error > 20
and visibility_periods_used > 8
and astrometric_chi2_al/(astrometric_n_good_obs_al-5)
    < 1.44*greatest(1,exp(-0.4*(phot_g_mean_mag-19.5)))
```

To create our `HALO` samples, we have used a similar query with a different parallax cut:

```
select source_id, bp_rp, phot_g_mean_mag, phot_bp_rp_excess_factor, ruwe, ra, dec,
parallax, pmra, pmdec, parallax_error, pmra_error, pmdec_error, parallax_pmra_corr,
parallax_pmdec_corr, pmra_pmdec_corr, visibility_periods_used, astrometric_chi2_al,
astrometric_n_good_obs_al, radial_velocity,
radial_velocity_error,
if_then_else(
  bp_rp > -20,
  to_real(case_condition(
    phot_bp_rp_excess_factor - (1.162004 + 0.011464* bp_rp + 0.049255*power(bp_rp,2)
                                  - 0.005879*power(bp_rp,3)),
    bp_rp < 0.5,
    phot_bp_rp_excess_factor - (1.154360 + 0.033772* bp_rp + 0.032277*power(bp_rp,2)),
    bp_rp >= 4.0,
    phot_bp_rp_excess_factor - (1.057572 + 0.140537*bp_rp)
  )),
  phot_bp_rp_excess_factor
) as excess_flux
from gaiadr3.gaia_source
where parallax_over_error > 10
and parallax > power(3, -1)
and ruwe < 1.15
and phot_g_mean_flux_over_error > 50
and phot_rp_mean_flux_over_error > 20
and phot_bp_mean_flux_over_error > 20
and visibility_periods_used > 8
and astrometric_chi2_al/(astrometric_n_good_obs_al-5)
    < 1.44*greatest(1,exp(-0.4*(phot_g_mean_mag-19.5)))
and 4.74*sqrt(power(pmra, 2) + power(pmdec, 2))/parallax > 200
```

---

[7] https://gea.esac.esa.int/archive/

Table B1. Vertices for the regions in M_G and $G_{\rm BP} - G_{\rm RP}$ that make up our red and blue halo sequences.

$G_{\rm BP} - G_{\rm RP}$ mag	M_G mag
2.4	11
2.110	10.087
2.012	9.522
1.789	8.630
1.637	8.178
1.452	7.565
1.262	7.021
1.142	6.652
1.034	6.239
0.936	5.826
0.843	5.326
0.756	4.782
0.729	4.478
0.708	4.000
0.713	3.695
0.756	3.413
0.849	3.326
0.925	3.260
0.963	3.239
0.990	2.412
1.066	1.173

APPENDIX B: RED AND BLUE CMD SEQUENCE SELECTION

Table B lists the vertices for the intersect between red and blue regions of the CMD outlined in Section 2. In addition to this, the blue section starts from the point $(G_{\rm BP} - G_{\rm RP}, M_G) = (-0.125, 11)$ mag and passes through the points (0.8, 1) mag and (-0.125, 1.95) mag after the intersecting vertices. The red section starts from (3.125, 11) mag and after the intersecting vertices ends at (3.125, 5.25) mag.

This paper has been typeset from a TEX/LATEX file prepared by the author.

Printed by Media-Tryck, Lund 2022 NORDIC SWAN ECOLABEL 3041 0903

LUND
UNIVERSITY

Faculty of Science
Department of Astronomy
and Theoretical Physics

ISBN 978-91-8039-411-6

9 789180 394116